UNIVERSIDADE ESTADUAL DE CAMPINAS
Instituto de Física Gleb Wataghin

GUSTAVO DE OLIVEIRA LUIZ

DYNAMICS OF COUPLED MICRO-OSCILLATORS

DINÂMICA DE MICRO-OSCILADORES ACOPLADOS

CAMPINAS

2017

GUSTAVO DE OLIVEIRA LUIZ

DYNAMICS OF COUPLED MICRO-OSCILLATORS

DINÂMICA DE MICRO-OSCILADORES ACOPLADOS

Thesis presented to the
Institute of Physics Gleb Wataghin
of the University of Campinas
in partial fulfillment of the requirements
for the degree of Doctor in sciences

Tese apresentada ao
Instituto de Física Gleb Wataghin
da Universidade Estadual de Campinas
como parte dos requisitos exigidos para a
obtenção do título de Doutor em ciências

Supervisor/Orientador: Gustavo Silva Wiederhecker

ESTE EXEMPLAR CORRESPONDE À VERSÃO FINAL
DA TESE DEFENDIDA PELO ALUNO
GUSTAVO DE OLIVEIRA LUIZ, E ORIENTADA PELO
PROF. DR. GUSTAVO SILVA WIEDERHECKER.

CAMPINAS
2017

Agência(s) de fomento e nº(s) de processo(s): CNPq, 153044/2013-6
ORCID: http://orcid.org/0000-0003-3592-5639

Ficha catalográfica
Universidade Estadual de Campinas
Biblioteca do Instituto de Física Gleb Wataghin
Lucimeire de Oliveira Silva da Rocha - CRB 8/9174

L968d

Luiz, Gustavo de Oliveira, 1988-
Dynamics of coupled micro-oscillators / Gustavo de Oliveira Luiz. – Campinas, SP : [s.n.], 2017.

Orientador: Gustavo Silva Wiederhecker.
Tese (doutorado) – Universidade Estadual de Campinas, Instituto de Física Gleb Wataghin.

1. Teoria de modos acoplados. 2. Optomecânica de cavidade. 3. Dissipação de energia. 4. Oscilações não-lineares. 5. Silício. I. Wiederhecker, Gustavo Silva,1981-. II. Universidade Estadual de Campinas. Instituto de Física Gleb Wataghin. III. Título.

Informações para Biblioteca Digital

Título em outro idioma: Dinâmica de micro-osciladores acoplados
Palavras-chave em inglês:
Coupled mode theory
Cavity optomechanics
Energy dissipation
Nonlinear oscillations
Silicon
Área de concentração: Física
Titulação: Doutor em Ciências
Banca examinadora:
Gustavo Silva Wiederhecker [Orientador]
Paulo Clóvis Dainese Júnior
Fernando Iikawa
Edson Denis Leonel
Hugo Leonardo Rocha de Lira
Data de defesa: 05-09-2017
Programa de Pós-Graduação: Física

MEMBROS DA COMISSÃO JULGADORA DA TESE DE DOUTORADO DE **GUSTAVO DE OLIVEIRA LUIZ – RA 071086** APRESENTADA E APROVADA AO INSTITUTO DE FÍSICA "GLEB WATAGHIN", DA UNIVERSIDADE ESTADUAL DE CAMPINAS, EM 05/09/2017.

COMISSÃO JULGADORA:

- Prof. Dr. Gustavo Silva Wiederhecker - (Orientador) DFA/IFGW/UNICAMP
- Prof. Dr. Paulo Clovis Dainese Junior - DEQ/IFGW/UNICAMP
- Prof. Dr. Fernando Iikawa - DFMC/IFGW/UNICAMP
- Prof. Dr. Edson Denis Leonel - UNESP (Campus de Rio Claro)
- Prof. Dr. Hugo Leonardo Rocha de LIRA - Instituto de Estudos Avançados do Centro Técnico Aeroespacial

A Ata de Defesa, assinada pelos membros da Comissão Examinadora, consta no processo de vida acadêmica do aluno.

CAMPINAS
2017

Agradecimentos

Agradeço primeiramente à minha esposa, Bia, que me apoiou em todos esses anos, compartilhando comigo todos os bons momentos e suportando, mais que qualquer outra pessoa, o mau humor quando as coisas não iam tão bem. Além de sempre compreender as razões que me levaram a chegar em casa, diversas vezes, de madrugada, após um dia inteiro de medidas no laboratório.

Agradeço aos meus pais, Jô e Paulo, que sempre me apoiaram, apesar das longas ausências de casa causadas por fins de semana e feriados trabalhando. Também agradeço à minha irmã Camila pela ajuda nos momentos em que precisei.

Aos meus amigos Felipe, Rodrigo, Guilherme, Debora e Yovanny que, durante todos os anos, contribuíram neste trabalho ajudando desde os processos de preparação de amostras até montagens experimentais e discussões sobre os resultados, além da caracterização de alguns do equipamentos usados. E, juntamente com esses, ainda há aqueles que sempre estiveram lá para dar opiniões e trocar ideias, seja sobre nossos trabalhos ou não: Laís, Marvyn, Mário, André e Jorge.

Ao meu orientador, Gustavo Wiederhecker, pelo apoio constante, sempre presente nos momentos de dúvida e dificuldade, ficando às vezes até tarde no laboratório para me ajudar a realizar algumas medidas. Igualmente importante foi o professor Thiago Alegre, tanto discutindo os problemas que surgiam no caminho, quanto auxiliando no preparo e realização das medidas. Ambos também foram importantes fornecendo conselhos valiosos sobre o trabalho e sobre a carreira.

A diversos professores e seus alunos, que nos emprestaram e ajudaram a operar equipamentos por vezes essenciais para a realização deste projeto.

Aos funcionários Totó e Antonio Celso, que garantiram o bom funcionamento dos laboratórios de fabricação, tanto cuidando da infraestrutura quanto garantindo que todos os materiais necessários estivessem disponíveis. Também agradeço aos funcionários da secretaria do departamento e da coordenadoria de pós-graduação.

E finalmente, mas não menos importante, agradeço às agências de fomento e outras instituições, sem as quais nada disso seria possível, CAPES, CNPq, FAPESP, UNICAMP, Instituto de Física Gleb Wataghin (IFGW), The Optical Society (OSA) e o INCT Fotônica (FOTONICOM).

Resumo

Nas últimas décadas a optomecânica de microcavidades chamou a atenção de cientistas e engenheiros, que encontraram na interação entre luz e ondas acústicas aplicações que variam de sensores de massa com resolução atômica, até a preparação de estados quânticos de osciladores harmônicos mesoscópicos, passando por simuladores quânticos, filtros ópticos controláveis opticamente, criação de estados topológicos para luz e fônons, apenas citando alguns exemplos. Apesar das diversas demonstrações de vários dispositivos, sendo discos e cristais fotônicos os formatos mais comuns, há ainda um grande esforço no sentido de aperfeiçoá-los reduzindo perdas ópticas e mecânicas e suprimindo outros fenômenos de óptica não-linear, como absorção de dois fótons, que podem impedir seu funcionamento apropriado. Como ressonadores ópticos e mecânicos tipicamente compartilham a mesma estrutura nestes dispositivos, seus projetos são acoplados, dificultando o aprimoramento independente de cada um.

Nesta tese usamos dispositivos optomecânicos de campo próximo, cuja interação entre modos mecânicos e ópticos se dá através do campo evanescente do último, para desacoplar o projeto mecânico do óptico, o que nos permitiu estudar a otimização do ressonador mecânico sem qualquer efeito sobre a cavidade óptica. Com um ressonador mecânico de silício composto por dois osciladores acoplados, pudemos demonstrar que o correto equilíbrio das massas de cada oscilador é um método simples e eficiente para suprimir as perdas devido à radiação de energia mecânica para o substrato na escala de frequência de 50 MHz. Este processo permitiu que fatores de qualidade limitados por perdas relacionadas ao material e à superfície, da ordem de 10 mil à temperatura ambiente e de 50 mil a aproximadamente 25 K, fossem obtidos. Também observamos nestes dispositivos o fenômeno de auto-pulsação, que apresenta uma dinâmica própria tão interessante quanto a optomecânica, apesar de impedir a operação apropriada dos osciladores optomecânicos. Estudamos este fenômeno separadamente e demonstramos que estes pulsos, ocorrendo em duas cavidades ópticas acopladas por seus campos evanescentes, podem sincronizar com o campo óptico sendo o único intermediador.

Ambas as demonstrações têm implicações importantes, abrindo caminho para o desenvolvimento de novas plataformas de interesse tanto científico quanto tecnológico, como estruturas para o estudo de estados topológicos para a luz e para ondas acústicas e geradores de sinal de radio-frequência de alto desempenho. Além disso, os dispositivos foram todos produzidos em uma fábrica comercial, o que também demonstra que sua fabricação está pronta para ser escalada para produção em massa.

Abstract

Cavity optomechanics in the micro-scale has attracted the attention of scientists and engineers on the last few decades, who encountered applications to the interaction of light and acoustic waves ranging from atomic resolution mass sensors to the preparation of quantum states of mesoscopic harmonic oscillators, passing by quantum simulators, optically controllable optical filters, formation of topological states for both photons and phonons, just to mention a few examples. Although various devices have been demonstrated, with disks and photonics crystals being the most common designs, there is still a large effort to improve them by reducing optical and mechanical losses and suppressing other non-linear phenomena, such as two-photon absorption, that may affect their proper operation. Because optical and mechanical resonators typically share the same structure in these devices, their designs are coupled, which complicates the independent improvement of each one.

In this thesis we used near-field optomechanical devices, whose mechanical modes interact with the optical through the latter's evanescent field, to decouple the mechanical design from the optical, what allowed us to focus all attention on the mechanical resonator. With a silicon mechanical resonator composed of two coupled oscillators, we could demonstrate that the correct balance of the masses of the oscillators is an efficient and simple way to suppress losses due to energy radiation to the substrate at the 50 MHz frequency range. This strategy led to material and surface limited quality factors close to 10k at room temperature and 50k at approximately 25 K. We also observed the phenomenon of self-pulsing in these devices, which presents dynamics as interesting as the optomechanical interactions do, in spite of being a problem for the proper operation of the optomechanical devices. We studied this phenomenon separately and demonstrated that these pulses, when occurring in two evanescently coupled optical cavities, may synchronize with the optical field being the sole intermediary.

These two demonstrations have important implications, paving the way for new platforms of scientific and technological interest, such as structures for the study of topological states for both light and acoustic weaves as well as high efficiency radio-frequency signal generators. Moreover, these devices were all fabricated in a commercial foundry, which also demonstrates that the fabrication of such technology is ready to be scaled up to mass production.

List of Figures

List of Acronyms

Acronym	Description	Acronym	Description
FP	Fabry-Pérot cavity	PBS	Polarizing beam-splitter
WGM	Whispering-gallery mode	SNR	Signal to noise ratio
NFO	Near-field optomechanics	PSD	Power spectral-density
TPA	Two-photon absorption	PM	Phase modulation
FC	Free charge-carriers	AM	Amplitude modulation
SOI	Silicon-on-insulator	ENBW	Effective noise bandwidth
CMOS	Complimentary metal-oxide-semiconductor	RBW	Resolution bandwidth
SEM	Scanning electron microscope (microscopy)	FEM	Finite element method
BOE	Buffered oxide-etch	PML	Perfectly matched layer
IPA	Isopropyl alcohol	MEMS	Micro-electro-mechanical systems
CPD	Critical-point dryer	TED	Thermo-elastic damping
SMF	Single mode (optical) fiber	AKE	Akhiezer effect (damping)
FSR	Free-spectral-range	TE	Transverse electric (optical mode)
DAQ	Data acquisition system	TM	Transverse magnetic (optical mode)
VOA	Variable optical attenuator	RT	Room temperature
PC	Polarization controller	LT	Low temperature
MZI	Mach-Zehnder interferometer	LNT	Liquid nitrogen temperature
AC	Acetylene (wavelength reference) cell	LH	Liquid helium
RF	Radio frequency	LN	Liquid nitrogen
ESA	Electrical spectrum analyzer	WDM	Wavelength division multiplexer
LO	Local oscillator	OSC	Oscilloscope

List of Symbol

Symbol	Description
$\mathrm{i} = \sqrt{-1}$	Imaginary unit
c	Speed of light
h	Planck's constant
$\hbar = h/2\pi$	Reduced Planck's constant
k_b	Boltzmann's constant
ε_0	Vacuum electrical permitivity
t	Time variable
v_g	Optical mode group velocity
n	Index of refraction of a material
n_eff	Effective Index of refraction of a confined optical mode
n_g	Group index of refraction of a confined optical mode
γ	Grüneisen parameter
G_{OM}	Optomechanical coupling rate
$\mathrm{x}_{\mathrm{zpf}}$	Quantum zero point fluctuation displacement
x	mechanical displacement amplitude
Ω_m	Mechanical resonant angular frequency
$f_m = \Omega_m/(2\pi)$	Mechanical frequency
γ_m	Mechanical damping rate
β_{ij}	Coupling rate between two mechanical oscillators
$\mathbf{U}_n$	Normalized mechanical displacement
$\mathbf{E}$	Electric field vector
$\mathbf{D}$	Electric displacement vector
Γ_{OM}	Optomechanical overlap integral
P_{in}	Input laser power of an optical cavity
P_d	Power coupled into the optical cavity
$U = \mid a \mid^2$	Intra-cavity stored energy
$P_{out}(\Delta)$	Detuning dependent optical cavity transmission
$\Delta = \omega_l - \omega_0$	Input laser frequency detuning with respect to the optical resonance of the cavity
λ_0	Optical resonant wavelength
$\omega_0 = 2\pi\ c/\lambda_0$	Optical resonant angular frequency
ω_l	Input laser angular frequency

δ_0	Frequency mismatch between the resonances of two cavities
C_i	i^{th} cavity in an array of coupled cavities
κ	Total linear decay rate of the optical cavity, also called cold cavity decay rate (includes linear absorption, scattering and coupling to the waveguide)
$\tau_{opt} = 1/\kappa$	Optical life-time
κ_e	Coupling rate between optical cavity and waveguide
κ_i	Intrinsic decay rate of the optical cavity (may include linear and non-linear loss sources)
κ_{lin}	Optical decay rate due to linear absorption
κ_{nla}	Optical decay rate due to non-linear absorption
$\kappa_{rad,scat}$	Optical decay rate due to radiation and/or scattering
γ_{FC}	Free-carriers decay rate
$\tau_{FC} = 1/\gamma_{FC}$	Free-carrier life-time
N	Density of free-carriers (FC)
γ_{th}	Thermal decay rate
$\tau_{th} = 1/\gamma_{th}$	Thermal life-time
$\theta = T - T_0$	Temperature variation with respect to equilibrium
T	Temperature variable
T_0	Equilibrium temperature
$\mathrm{g}_0 = G_{\mathrm{OM}}\mathrm{x}_{\mathrm{zpf}}$	Vacuum optomechanical coupling rate
g_θ	Coupling coefficient of optical resonance to temperature variation
g_N	Coupling coefficient of optical resonance to the density of carriers
g_{cp}	Coupling coefficient of counter-propagating optical resonances
g_{12}	Coupling coefficient of optical modes of two cavities
α_{TPA}	Two-photon absorption loss parameter (see text for more information)
α_N	Free-carrier optical loss parameter (see text for more information)
β_{FC}	Free-carrier generation parameter
β_{th}	Thermal source parameter
σ_{Si}	Silicon free-carrier absorption cross-section
β_{si}	Silicon two-photon absorption parameter
Γ_{TPA}	Overlap factor for two-photon absorption
V_{TPA}	Volume effectively available for two-photon absorption
Γ_{FC}	Overlap factor for free-carrier absorption
V_{FC}	Volume effectively available for free-carrier absorption
Γ_{disk}	Fractional energy overlap with θ whithin the optical cavity
V_{disk}	Physical volume of the optical cavity
V_{eff}	Effective optical mode volume
ρ	Material density
c_p	Material heat capacity

$\overline{\Delta\omega}$	Mean optical frequency shift caused by the mean temperature and FC density variation
$\overline{\theta}$	Mean temperature variation
$\overline{N}$	Mean FC density variation
$\Delta\omega$	Frequency shift of the optical resonance due to non-linear effects
$\Delta\lambda$	wavelength shift of the optical resonance

Contents

Chapter 1

Introduction

1.1. Optomechanics: an introduction

In the past half a century or so, the interaction of electromagnetic fields confined in an optical cavity with acoustic vibrations have attracted the attention in various scientific communities [1–3]. Nowadays, the so called cavity optomechanics is found in a very broad range of mass and length scales, from kilograms and kilometers in gravitational waves detectors [4] down to fentograms and nanometers in micro-fabricated devices [5]. These systems have been used to demonstrate sensors with high sensitivity [4, 6, 7], the preparation of mesoscopic harmonic oscillators into their quantum ground state [8, 9], sources of coherent laser-like phonons [10], all-optical tunable optical filters [11], self-sustained oscillators and their synchronization [12, 13], among many other examples of applications.

The operation of all cavity optomechanical systems rely on a feedback loop (fig. 1.1a) in which the light stored inside the cavity exerts a pressure on the mechanical structure and, because the structure is mechanically compliant at some level, the structure moves, inducing a change on the optical frequency of resonance and changing the amount of stored optical energy. The typical toy-model for this interaction is a Fabry-Pérot optical cavity (FP) with one of its mirrors coupled to a spring (fig. 1.1b).

The first to report a complete analysis of this feedback process was Vladimir Braginskiĭ [1] in the context of optical interferometers. What Braginskiĭ showed is that the dynamical variations due to this feedback, often called dynamical backaction, can cause changes to both mechanical stiffness and damping rate. The former is called optical spring effect, as the varying force caused by the optical field alters the stiffness of the mechanical oscillator. The change in damping rate or optomechanical damping rate, as Braginskiĭ argues, appears because the optical field inside the cavity has a finite response-time, which creates a delay on the feedback loop, causing the optical force to have a component in phase with the mechanical velocity.

Both the spring effect and the optomechanical damping rate signal depend on the detuning of the pump laser with respect to the cavity's resonance frequency. If the laser is detuned to lower frequencies (red-detuned) the mechanical frequency of oscillation (Ω_m) decreases, while the effective damping rate, given by the intrinsic plus optomechanical damping rates ($\gamma_{eff} = \gamma_m + \gamma_{OM}$) increases. This is the effect used to reduce the temperature of a mechanical mode, ultimately leading to quantum ground state cooling [8]. On the other hand, if the input laser is detuned to higher frequencies (blue-detuned) than the optical resonance the spring

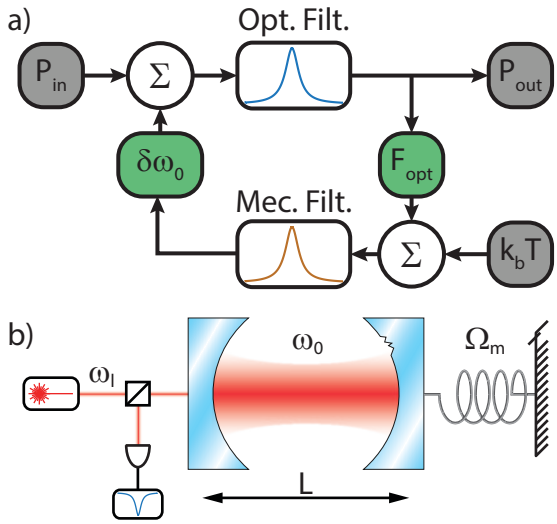

Figure 1.1: **Optomechanics schematics.** a) Feedback diagram of an optomechanical cavity system. P_{in} and P_{out} are the optical input and output power, respectively; F_{opt} is the force the optical field exerts on the cavity's structure; k_bT is the thermal energy that initially excites the mechanical structure, with k_b being the Boltzmann constant and T the temperature of the environment; $\delta\omega_0$ is the optical frequency shift caused by the motion of the mechanical structure. b) Optomechanical toy-model, composed by a Fabry-Pérot optical cavity with a movable mirror placed on a spring. ω_0 is the optical resonant angular frequency, determined by the cavity's length L. ω_l is the input laser angular frequency. Ω_m is the natural angular frequency of oscillation of the mass-spring system formed by the mirror and a spring.

effect increases the mechanical frequency of oscillation, while the optomechanical damping rate is actually negative and reduces the effective damping rate of the mechanical oscillator. This reduction of γ_{eff} in practice causes an amplification of the mechanical oscillations, ultimately leading to self-sustained oscillations. This is the regime of operation used to demonstrate phonon-lasing [10] and optically mediated synchronization of mechanical oscillators [12].

More recently, interest in the dynamics arising from the coupling of optomechanical oscillators in arrays of devices have emerged [14, 15]. And the first demonstration of the possibility of such a system [12] only encourages other groups to follow this path, e.g., proposing realistic structures that may lead to topological effects and pseudomagnetic fields for sound waves (or phonons) [16, 17].

1.2. Challenges in optomechanics

Although the toy-model typically used to explain optomechanics is a FP cavity with a moving mirror (fig. 1.1b), this is not an easy design to implement in the micro- and nano-scale required for integrated photonics. The most common designs encountered in literature for micro- and nano-scale optomechanical devices are disks, supporting optical whispering-gallery modes (WGM) [18], and photonic crystals [19], which guide and confine light by creating photonic band-gaps through periodic patterning. Figure 1.2 present a few examples studied in

our group, in this case all three made of silicon. Namely a bullseye optomechanical cavity (1.2a) studied by Felipe Santos [20], a PhD student of our group; a photonic-crystal optomechanical cavity (1.2b), studied by Rodrigo Benevides [21], another PhD student of the group; a double paddle near-field optomechanical device, which is object of study in this thesis.

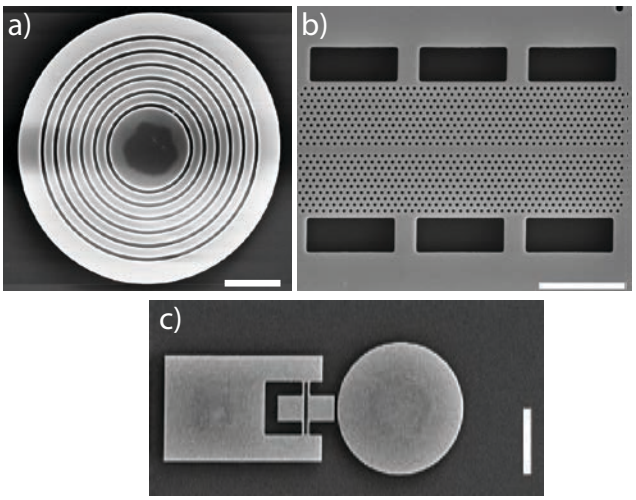

Figure 1.2: **Examples of optomechanical cavity designs.** a) Bullseye optomechanical cavity [20]. b) Photonic-crystal optomechanical cavity [21]. c) Double paddle near-field optomechanical device (studied in this thesis). All scale bars are 5 μm long.

In these devices, the coupling between optical and mechanical modes, characterized by the optomechanical coupling rate ($G_{\mathrm{OM}} = \partial\omega_0/\partial x$, where x is a parametric variable for the mechanical displacement), happens because of two effects: motion of the optical cavity boundaries [22], similarly to the FP case, and strain-induced changes of the material's index of refraction, what is called photo-elastic effect [23]. Hence, in order to increase the optomechanical interaction, or the optomechanical coupling rate, the devices are usually designed to maximize the overlap between optical and mechanical modes. Although, this overlap doesn't always guarantee higher optomechanical coupling rates [24], as the effects of moving boundary and strain may cancel each other out. And here the challenges of designing optomechanical devices emerge. Because optical and mechanical oscillations can be in very different wavelength scales, it is very difficult to produce a single structure capable of efficiently confining both kinds of oscillations maintaining good overlap between them, i.e., maintaining a considerable optomechanical coupling rate. Although this has been demonstrated for mechanical modes above the 1 GHz frequency scale [25–27], this is only possible because the acoustic wavelength at these frequencies is about the same order of magnitude of the optical field wavelength (taking the material index of refraction into account).

One approach that allows for independent optical and mechanical design, at the MHz frequency scale for the latter, is the so called near-field optomechanics (NFO) [28]. In this kind of device, the mechanical and optical resonators are totally independent structures, with the mechanical modes interacting with the optical field of a cavity through the latter's evanescent field. This allows for independent troubleshooting of optical and mechanical devices, leading

to independent improvements, at the expense of reduced optomechanical coupling rates as the overlap between optical and mechanical modes is reduced.

Mechanical losses

Efficient confinement of optical and mechanical modes involves producing devices with lower intrinsic losses, or damping rates. Losses in resonators are typically benchmarked by the quality factor (Q-factor or Q), which is defined as the ratio between the stored energy and the dissipated power per oscillation period. It is simple to show that, for low dissipation oscillators, this relation is equivalent to the ratio between the oscillating frequency and the damping rate ($Q = \Omega_m/\gamma_m$ for a mechanical mode, for example) [29, 30].

When referring to damping rate, one is typically concerned about the slow decay (in the low loss limit) of the amplitude of oscillation. However the devices also suffer influence from the surrounding environment, which can cause fluctuations to both phase and amplitude of the oscillations, which are called phase- and amplitude-noise. In terms of phase-noise, a common quantity used to asses the performance of the resonator is the Qf-product, which for mechanical oscillators, for example, quantify their decoupling from the environment at a finite temperature [31]. The Qf-product also allows for a better comparison between resonators, as this parameter becomes frequency independent for resonators whose losses are limited by material absorption [32, 33].

Although low loss, or high quality factor, optical microcavities have been demonstrated [21, 34], obtaining high Q's in micromechanical devices is still a challenge, with loss mechanisms and methods to suppress them being objects of recent studies [35–39]. Ultimately, mechanical resonators are limited by material absorption, but for micro- and nanomechanical devices the necessary supports become an important dissipation channel, as energy may leak through them towards the substrate [40–42], what is commonly called anchor loss.

Of course that many solutions to suppress anchor loss emerged, such as using a periodic structure presenting (partial) phononic band gaps at the frequencies of interest [20, 43], using deep trenches to cerate mesas [44] and destructive interference of the radiated elastic waves [38, 45]. All of these methods present their advantages and disadvantages; for instance, the phononic band gap approach is very efficient in shielding mechanical modes on the GHz scale, but for modes below the 100 MHz scale their large footprint can make them impractical for integrated devices, although they have been used for other purposes [7].

And reducing losses in optomechanical devices is not only interesting for increasing the efficiency of the optomechanical effect. Because many substrates used as platforms for optomechanics also present non-linear optical susceptibility, and the stored energy density in micro-cavities can easily be high enough for other non-linear phenomena to take place, mechanical losses and the optomechanical couping rate are the key parameters that determine if the device will operate as intended or if other phenomena are going to hinder its functionalities.

Self-pulsing in silicon micro-cavities

Among the most common materials chosen for fabricating micro and nano-scale optomechanical devices is silicon. That is because all the processes involved to obtain the final structures are well established thanks to the great development of the electronics industry. Moreover, because the electronics industry is largely based on silicon, this is thought to lead to easier integration of optomechanics, photonics and electronics in the future.

However, silicon has high optical non-linear susceptibility [46], which means it can produce non-linear optical phenomena if pumped with high power. Moreover, the imaginary part of this non-linear susceptibility is also large, which leads to significant two-photon absorption (TPA). This non-linear absorption, more than just adding to the linear [47] optical losses of an optical cavity, may also cause what is called self-pulsation of the transmitted light [48, 49]. This process is understood to take place when the dispersion caused by the TPA generated free charge-carriers (FC dispersion) and the one caused by the thermo-optical effect, which are opposite in silicon, compete and drag the optical resonance frequency up and down, producing pulses like those exemplified in figure 1.3.

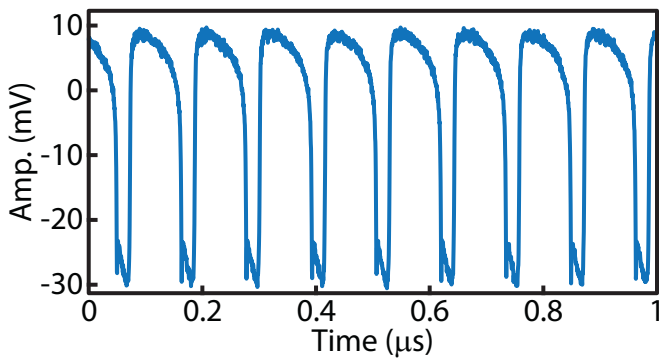

Figure 1.3: **Pulses generated on a silicon optical micro-cavity.**

If this process happens for input powers lower than the threshold of optomechanical self-sustained oscillations, it can completely compromise the optomechanical device's performance. On the other hand, these non-linear pulses have been demonstrated to lock to the optomechanical oscillations [50, 51], which actually presents a new area to be studied.

1.3. Summary of this thesis

In the first part of this work in this thesis we demonstrate a silicon NFO device whose mechanical resonator's losses are limited by bulk material and surface related mechanisms. For that we designed a device in which anchor losses are suppressed by elastic wave interference, which led to room temperature (293 K) mechanical quality factors of 7.6k for a given mode, operating at approximately 55MHz. The material and surface dependence of this Q-factor is demonstrated by measuring the devices at temperatures ranging from 20 K up to

293 K, as well as submitting the devices to processes that are know to improve the surface properties, such as chemical cleaning and annealing. Part of this work was presented at the ENFMC Brazilian Physical Society Meeting of 2015, in which it received an award as "The best poster on the optics and photonics area". Also, the final results were presented at the Conference on Lasers and Electro-Optics®of 2016 (CLEO 2016) [52]. A paper has also been submitted for publication and is currently under revision, but a preprint version can already be accessed on arXiv [53].

When trying to set these NFO devices into self-sustained oscillations at room temperature, we observed self-pulsation with powers much lower than the estimated threshold for optomechanical oscillations. Because the samples fabricated at the foundry also included coupled optical cavities in their design, this appeared as an opportunity to test the possibility of the pulses of one cavity to couple to those of the other, much similar to what has been demonstrated in an optomechanical system [12]. Hence we studied this self-pulsing effect, first by performing measurements on a single cavity, used to understand the kind of experiments that should be performed and the basic results they would produce. Also, with the single cavity, we demonstrate the possibility of locking the pulses with an external weak tone in high order harmonics of the pulses [54]. And finally the synchronization of the pulses in two optically coupled cavities was demonstrated. This last part of the work was presented at the CLEO 2017 conference and a complete paper is under preparation.

1.4. Thesis structure

This thesis is divided in 6 chapters, with the first being this introduction. Chapter 2 presents the fabrication process through which the samples are produced, while chapter 3 presents a few details on the main measurement and data treatment techniques. Chapter 4 shows the results on the work in which we demonstrated the suppression of anchor loss in an NFO device, and that this led to material and surface limited mechanical Q-factors. Chapter 5 presents the work in which we studied the self-pulsation in silicon optical micro-cavities and demonstrated that self-pulsing of two coupled cavities can couple and synchronize, with only the optical field as the coupling mechanism. Chapter 6 is an outlook, conclusions and perspectives chapter. Additional information can be found in the references cited along the thesis and/or in the appendix when mentioned.

Chapter 2

Fabrication

There are various reasons why silicon-on-insulator (SOI) is largely used by the optomechanics and micro-photonics community. One of the main reasons is the fact that the fabrication processes are very well established thanks to the electronics industry development. In this thesis the possibility of mass production of photonic and optomechanical devices is demonstrated, as the samples tested were all fabricated in a commercial foundry.

This chapter presents a few details on the steps taken to obtain the samples used in this thesis, as well as compare the advantages and disadvantages of producing samples through a commercial foundry.

2.1. Foundry vs. in-house fabrication

The samples measured in this thesis were all fabricated by IMEC, a commercial foundry based in Belgium, through the ePIXfab Alliance. The ePIXfab is a program that allows for any company or research group to submit a photonics chip design to be processed in a CMOS compatible processing chain. See appendix I for the code used to generate the design of the samples presented in chapter 4. General details on the program, design rules and fabrication specifications can be found in their website[1].

Choosing the foundry over fabricating at UNICAMP's facilities have both advantages and disadvantages. One of the advantages is that more than one group can participate on the chip design, including their devices of interest in it, optimizing the chip space usage. In this way the cost of contracting the foundry is split between the groups and is fully compensated by the amount of research that can be done in each batch that is ordered. On the other hand, the timescale from design to samples delivery makes it very difficult to do prototyping, which is very often desired in device research.

Also, because of the technology used by the foundry to fabricate the samples, they specify that the minimum width of lines and spacing is of 150 nm, which is why the smaller dimensions in the devices we studied are of 200 nm, avoiding problems due to the foundry's limitations. Moreover, the devices produced in-house typically present better etched surfaces, leading to optical modes with higher quality factors because of less scattering induced by roughness. Although, the effect of the etched borders on optical quality factor depends on the device

[1] `http://epixfab.eu`

design, as demonstrated by another work developed in our group with photonic-crystals fabricated by the same foundry, which presented optical quality factors of the order of 10^6 [21].

Figure 2.1 shows two scanning electron microscope (SEM) images of the edge of disk optical cavities. On the left is a device produced at the foundry and on the right a device produced in-house at UNICAMP. Note that the roughness of the disk border on the left (foundry) is very apparent, while the device fabricated in-house presents very little roughness. The device on the right is a silicon optical micro-disk cavity fabricated by Felipe Santos, a recently graduated PhD of the group.

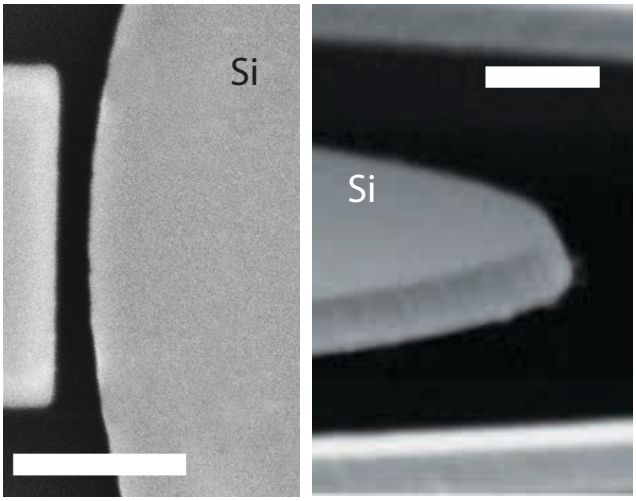

Figure 2.1: **Comparison of edge roughness in devices produced by the foundry and in-house.** Left: Near-field optomechanical device produced at the foundry. Right: Silicon disk optical cavity fabricated entirely at UNICAMP by Felipe Santos, a recently graduated PhD of the group. The scale bar on the left is 2 µm and on the right 1 µm.

But these problems are surpassed by the simplicity of just developing a design and receiving the devices all done a few months later, whereas the in-house fabrication may lead to longer time-scales if calibration of the processes are needed, which was the case during the development of this work. Besides, fabricating the devices in a commercial foundry also demonstrates that, despite all the limitations, the technology is ready for mass production and commercialization.

2.2. Fabrication step-by-step

General steps

The general fabrication process follows the sequence presented in figure 2.2. A wafer of SOI, which is composed by a 220 nm thick silicon layer on top of a 2 µm thick silicon oxide (or silica) thermally grown on a silicon substrate, have its surface covered by a photo sensitive resin (photoresist). The photoresist is exposed to UV light ($\lambda = 193$ nm)

with a mask and developed, leaving the mask's pattern imprinted on the photoresist. Then an ICP-RIE (Inductively-coupled plasma, reactive ion etching) plasma etches the material of the wafer exposed by the photoresist pattern, transferring this pattern to the first layer of the wafer. Finally, the devices are released by partially etching the oxide layer with a buffered oxide etcher (BOE), which is a buffered solution of 1 part of hydrofluoric acid (HF) to 6 parts of ammonium fluoride. Of all these steps, only the last is performed in-house.

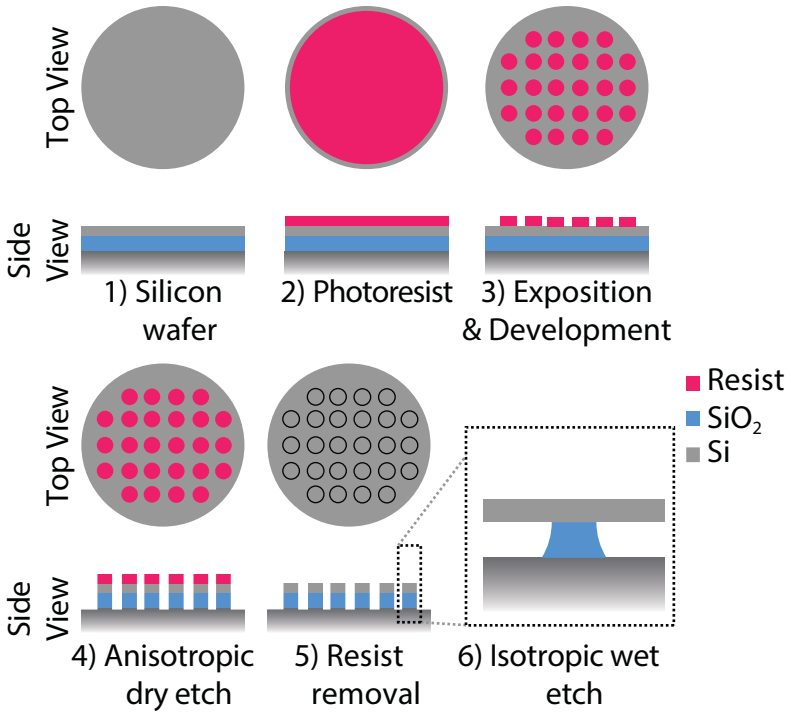

Figure 2.2: **Schematics of fabrication steps.** 1) A silicon on insulator (SOI) wafer is prepared. 2) A photosensitive resin (photoresist) is deposited on to of the wafer. 3) A pattern is imprinted on the photoresist using UV light. 4) An anisotropic plasma etch removes material around the photoresist mask. 5) The photoresist is removed. 6) An isotropic wet etch removes part of the oxide, leaving the devices suspended. Steps 1 through 5 are performed by the foundry, while step 6 is performed in-house.

Wet etching

The wet etch step is important not only for the mechanical devices, granting them their mechanical degrees of freedom, but also for the optical cavities tested. That is because the optical modes are probed by a tapered fiber (taper) and not an integrated waveguide, what requires that no oxide exist on top of the sample. If the bottom oxide layer was not removed the optical symmetry of the device is broken, distorting the optical modes [55], which can reduce the coupling of light from the taper to the optical cavity. Moreover, because the top silicon layer of the SOI is only 220 nm thick, when the taper is close to the cavity it would also be close to the silica below, which would lead to leak of optical power to the silica, also decreasing the amount of power coupled into the cavity. As mentioned before, from the steps presented in

figure 2.2, the foundry performs all but this last one, which is executed in a clean room of the Device Research Laboratory, at UNICAMP's Physics Institute. For the devices presented in this work, the etching times of this last step vary between 5 minutes of immersion in BOE, for the smaller disks presented in chapter 5, and 15 minutes, for the optomechanical devices presented in chapter 4.

A few steps are taken to properly release the samples in the wet etching process. First an optical mask isolates the regions of the devices being released. That is because the foundry uses a dummy-tilling structure in empty spaces of the chip to guarantee the spatial uniformity of their process (fig. 2.3a). Unfortunately, these structures are typically much smaller than the typical devices tested, which means that they usually detach from the substrate and float randomly over the sample, possibly landing on a device (fig. 2.3b) and deteriorating both optical and mechanical properties.

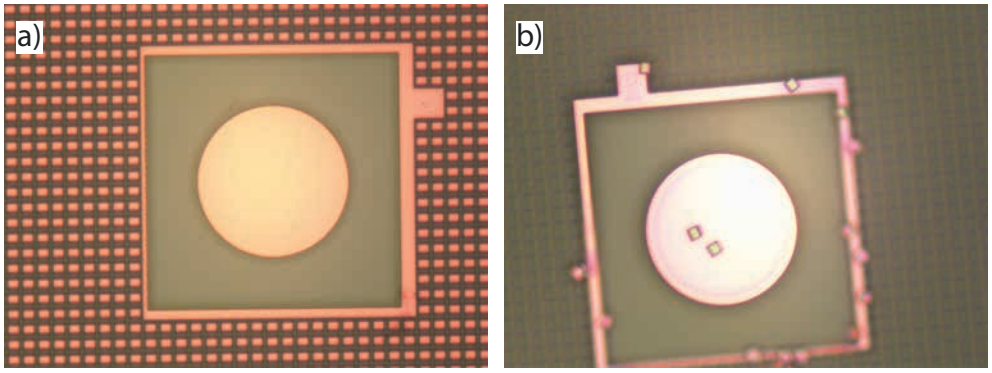

Figure 2.3: **Example of filling-factor structure landing on a device.** a) Disk optical cavity before wet etch. b) The same disk in (a) after the release without a protecting mask, with the dummy-tilling all gone and landing in random spots of the sample.

The procedure to obtain the mask for oxide etching start by cleaning the sample by rinsing it first with acetone, to remove any residual organic compound (e.g., photoresist used by the foundry), and then with isopropyl alcohol (IPA), to remove residual acetone. This cleaning process is important to guarantee proper adhesion and uniformity of the resist over the sample.

After cleaning it is necessary to use an adhesion promoter for better and reproducible results. This step depends on the photoresist used, which in this case was the SC1827. For this resist we chose to use the adhesion promoter Surpass 3000. Following the promoter's datasheet, we hydrate the sample for 30 seconds in deionized (DI) water, then immerse it in promoter for 1 minute and immerse it again in Di water for another 30 seconds. Then, the sample is dried by blowing clean nitrogen on it.

The photoresist is applied on the sample by the spinning process. For that the sample is inserted in a protected spinner, whose sample holder works by sucking air through an orifice with the help of a mechanical vacuum pump. If the sample is smaller than the spinner's sample holder, it is necessary to protect the orifice by placing the sample on a adhesive tape larger than the sample holder. Enough photoresist to cover the sample is dropped over the latter

and the spinner is turned on. The spinner was set to spin at 4000 rpm for 40 seconds.

After the spinner stops a soft-bake of the resist is performed on a temperature controlled hot-plate (if a tape was used on the spinner, it must be removed first). This soft bake is performed at 90 ºC for 90 seconds. After soft-baking, the sample is ready for exposition of the mask. In our laboratories we count on a MJB-3 mask aligner for exposing soda-lime glass masks. The mask was prepared in-house by the students Felipe Santos, Jorge Soares e Laís Fujii as well as the lab staff Antonio Augusto Von Zuben (Totó). After aligning the mask to the sample, it is exposed for 25 seconds. The development of the photoresist is then performed by immersing the sample for 1 minute on the AZ 300 MIF (metal ion free) developer and rinsed with DI water to stop the developing process.

The last step on the lithography procedure is to hard-bake the resist, so it becomes harder and more resistant to the etching process. This is done by taking the sample back to the hot-plate, this time with the temperature set to 120 ºC. The sample is left on the hot-plate for 5 minutes before going through etching. Finally, as mentioned before, etching is performed immersing the sample for a given amount of time into a BOE solution.

Figure 2.4 shows an example of a disk optical cavity whose bottom oxide was partially etched, producing a suspended device. Notice that the pedestal is approximately circular due to the isotropic nature of oxide wet etching. And this is another example of a sample in which the dummy-tile protecting mask was not used, leaving dummy-tiles scattered over the entire sample. The device shown in this example is a bullseye optomechanical resonator, produced in the same sample as the devices of this thesis and studied by Felipe Santos [20, 56].

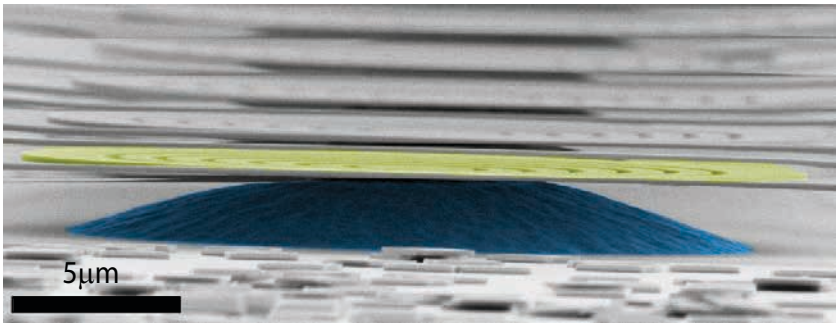

Figure 2.4: **Example of pedestal produced by BOE etching a disk optical cavity.** Notice that in this case the protecting mask was not used, leaving the dummy-tiles scattered all over the sample. This device is a bullseye optomechanical cavity, object of study of Felipe [20].

The etching process ends with the sample immersed in DI water, used to stop the etching process. Now the sample must be cleaned and properly dried to avoid any damage to the devices' structures.

Cleaning

After the release step is complete the sample is cleaned, first by immersing the sample in acetone, then in isopropyl alcohol (IPA) and finally Di water again, removing most of the remaining photoresist and acetone residuals. After that we follow the advice of Borselli, Johnson and Painter [57] to reduce optical absorption due to states on the surface of the silicon device caused by oxidation and dangling bonds. For that the sample is immersed for 10 minutes in a boiling solution (approx. 140 ºC) of sulfuric acid and hydrogen peroxide ($H_2SO_4 : H_2O_2$ - 3 : 1), called piranha solution. In this solution the sulfuric acid removes any residual organic substance from the surface and the H_2O_2 has the function of oxidizing the surface, forming a thin layer of silicon oxide. The passivation of the surface is performed by a 30 seconds dip in a 10% solution of HF in DI water, which removes the thin oxide layer and, as Borselli*et al.*argue, fills the left silicon surface dangling bonds with hydrogen atoms.

The whole process ends with the sample immersed in DI water, which needs to be dried so the devices can be tested. Because part of the structures are mechanically compliant and water's surface tension, while it is evaporating, apply a force on them towards the substrate, they tend to collapse.

Drying

We used two processes with high yield of suspended devices. The first is with a critical point dryer (CPD) and the second with methanol dried on a hot-plate. For the CPD process, performed in a Tousimis Autosamdri®-931 Series (here called CPD), after the sample is clean it is immediately moved from water to IPA and inserted into the CPD chamber, which is also field with IPA. The machine gradually exchanges all the IPA inside the chamber for liquefied carbon dioxide (CO_2). Then it brings the CO_2 past its phase transition critical point (pressure at 7.39 MPa and temperature at 31.1 ºC), when it has zero surface tensions and can be gradually removed from the chamber without damaging the devices [58]. This process typically has a 100% yield for the samples processed, but required transport of the sample between laboratories, as the machine is not in the same place where wet etching and cleaning are performed.

Due to the distance between the processing lab and the CPD tool, the methanol technique, which has a yield typically greater than 80% for our samples, was explored. In this process, after the sample is clean, water is substituted by methanol and the sample is then placed on a hot plate set to 100 ºC. This is considerably hotter than methanol's boiling point (64.7 ºC), hence the alcohol quickly evaporates. Because methanol's surface tension is about a third that of water [59, 60], this process have a yield high enough to obtain good samples.

Chapter 3

Measurement techniques

In this thesis, different phenomena are measured through the effects they cause on the proper ties of the optical cavities. This is performed by measuring light transmitted through the optical cavity, which requires that its optical properties are well characterized. Moreover, it is necessary to properly set the signal detection scheme to obtain the data necessary to study each phenomena. These tasks, although part of the daily activities of any optics and photonics laboratory, present some subtleties that are not always described in literature.

This chapter is dedicated to some details on the measurement techniques used to characterize the devices. It presents the problems encountered on determining the optical resonance and dispersion and how they were solved. A few details on the experimental setups are presented, specially concerning the vacuum and cryogenic setup, through which I also collaborated in other works developed by the group [20, 21, 61–64]. Then it presents the two different methods used to measure the signals produced by the non-linear interactions of the optical field with the material.

Before proceeding to the next section, we want to define a few relevant symbols that will be used throughout this thesis, to avoid confusion. Unless otherwise specified, Q refers to the quality factor of a mechanical resonator, while γ_m refers to the mechanical damping rate and κ to the optical damping rate. Also, Ω refers to a mechanical angular frequency and ω to an optical frequency. Other symbols can be found in the List of Symbols and are defined along the text when needed.

3.1. Optical spectra

Coupling light into and out of the optical cavity

To probe the optical properties of a cavity it is necessary to provide a communication channel for the input light to enter and exit the resonator. For micro devices this is typically done through integrated optical waveguides, which are fabricated on the same chip as the tested devices, or through tapered fibers (taper). In our group we chose to use tapers because they typically have low insertion loss ($<$1.5 dB) and they allow for quick change from a device to the other, as well as for controlling the coupling regime between waveguide and cavity.

The fabrication of the taper involves heating a single mode fiber (SMF) and pulling along its axis in a controlled way [65, 66]. The original fiber core diffuses due to the heat

making the fiber no longer single-mode, but as it stretches its diameter decreases [65], down to the point when it becomes a single-mode glass fiber with air cladding, when the taper diameter is of about 1.1 µm. The taper is desirably single-mode because to input and extract light through it the laser is still coupled to standard SMF; if light couples to any of the higher order modes of the taper, when it reaches the SMF it will be lost, what will be accounted as extra cavity losses [67]. In appendix F more details on the fabrication and set-up of the taper is given.

The optical resonances of a cavity are probed by approaching the taper to the cavity (fig. 3.1, left). Because the taper is thin, it has a considerable amount of optical power on its mode's evanescent field, which extends outside of the fiber. This evanescent field, on the region close to the cavity, couples the taper mode to the cavity's modes, allowing light to couple into de optical resonator [68]. It is then possible to probe the cavity's resonances by varying the frequency of the input laser and collecting the transmitted light with a photodetector.

The transmitted light presents well defined dips when the laser frequency matches those of the cavity's resonances (fig. 3.1, right). It is easy to obtain analytical functions with the expected shapes of these dips [29], which are left to appendix A. By fitting these functions to the a resonance dip it is possible to obtain all the characteristics pertaining to the optical resonance, namely the total optical decay rate ($\kappa = \kappa_i + \kappa_e$) that results in the full-width at half minimum of the resonance dip, and the coupling rate between cavity and waveguide (κ_e) that is related to the depth (or extinction ratio) of the resonance dip. From these two quantities it is possible to estimate the losses due only to processes inherent to the cavity, called intrinsic losses and typically symbolized by κ_i.

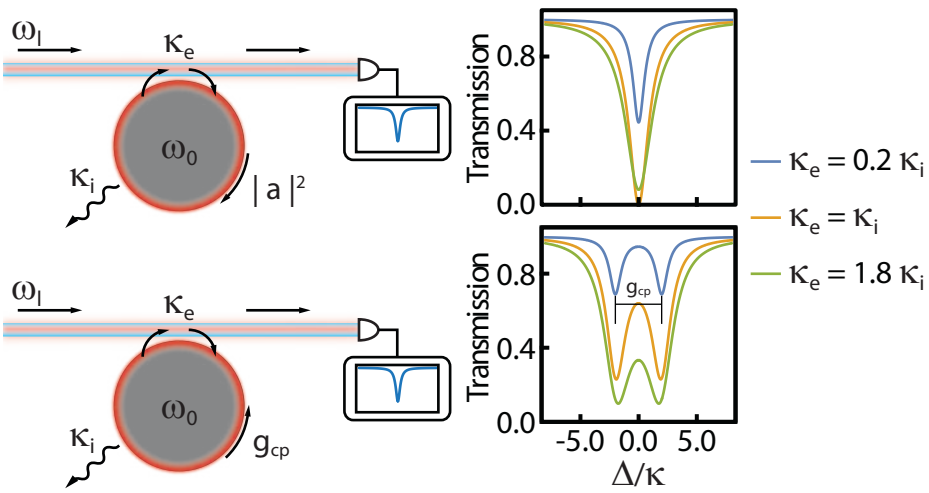

Figure 3.1: **Schematics of cavity-waveguide coupling schemes.** The top figures show the schematics of a one-port cavity coupled to a waveguide (left) and the detuning dependent transmission over one of its resonances (right). The bottom shows the schematics of a two-port cavity (left) and the transmission over one of its resonances (right). The colors on the transmission curves represent the undercoupled (blue), critically-coupled (yellow) and overcoupled (green) coupling regimes. $\Delta = \omega_l - \omega_0$ is the angular frequency detuning between the input laser and the cavity's resonance and g_{cp} is the coupling rate between counterpropagating modes.

Now, the proper determination of κ_e requires knowledge of the condition of cavity-

waveguide coupling. Note in figure 3.1 that two situations are presented. On top is an ideal disk cavity, in which light only propagates in one direction before coupling back to the fiber. This device will produce single dips as the ones shown on the top-right and the depth of the dips are determined by κ_e, such that if $\kappa_e < \kappa_i$ the transmission is never zero; this condition is called undercoupled regime. Zero transmission occurs only when $\kappa_e = \kappa_i$, being this condition called critically-coupled regime. And when $\kappa_e > \kappa_i$, the overcoupled regime, the transmission doesn't reach zero again. This means that it is possible to obtain, for the same resonance, two pairs of κ and κ_e that would make the analytical function to properly fit the measured resonance. The only way to determine the correct pair of decay rates is by experimentally testing the condition of coupling while testing the device.

That may not be a problem when the cavity presents coupling of counterpropagating modes of the cavity [69]. This coupling may happen for various reasons, being the most common of them roughness of the disk's surface [70], and causes the splitting of the resonance dip into two dips. In this case the cavity may behave similarly to a two-port cavity (e.g., a Fabry-Pérot cavity), such that increasing κ_e always increases the dips extinction ratio, with zero being an asymptote to this process. In this case the knowledge of coupling condition at the moment of measurement is substituted by the knowledge that the dips are due to coupled modes.

The last information that may be drawn from the optical characterization is the resonance frequency (or wavelength). This can be obtained by properly relating the transmission dip to the laser wavelength at which it occurred. Also, the dips of optical modes of the same family are separated from each other on the spectrum by a certain amount called the free-spectral range (FSR), which is not necessarily constant with varying resonance wavelength. This variation of the FSR can be related to the variation of the group velocity of the light coupled in the different mode, which is called the dispersion of the optical modes. This information is important as it helps to determine the optical mode, such as demonstrated in section 4.5 of the chapter 4, but for that a few extra steps are needed, as will be detailed later in this section.

Data acquisition

To obtain the optical transmission spectra of the cavities we use a setup represented by the schematics presented in figure 3.2. In this setup the light of an external cavity tunable laser (Yenista's Tunics Reference – 1460-1610 nm) is coupled into a single-mode optical fiber (SMF28) and then into a taper. The taper is positioned close to the cavity with the aid of high precision micro-positioners (Suruga Seiki Co.'s – KYC06020-G and KZC06020-G – for room conditions and Attocube's – ANPx101/RES, ANPz101/RES, ANSxy100lr and ANSz100std – for vacuum and cryogenic conditions). The fiber usually touches the device or a structure close to the device designed for that, this guarantees that the the taper is stable during the experiments. The light transmitted through the taper is then detected by a power-meter (Thorlabs PM200), whose voltage output is measured either by a data acquisition system (DAQ

– National Instrument's NI-USB6259) or by an oscilloscope (Agilent's DSO-9254A).

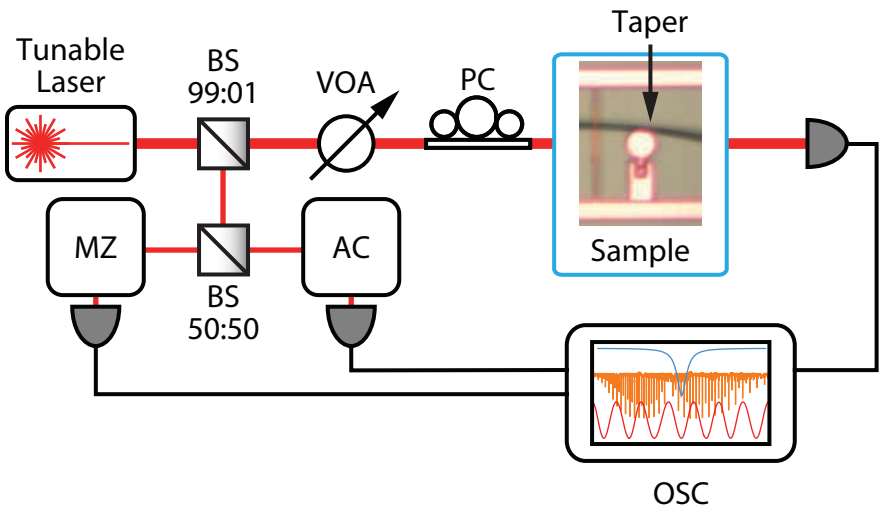

Figure 3.2: **Schematics of experimental setup for optical spectrum characterization.** BS: beam-splitter; VOA: variable optical attenuator; PC: polarization controller; MZ: Mach-Zehnder interferometer; AC: acetylene reference cell; OSC: oscilloscope.

To control the power inserted into the optical cavity a variable optical attenuator (VOA – OZ Optics') is used, maintaining the laser output power constant and stable. Also, the optical modes of the devices have a preferred polarization, hence a fiber polarization controller (PC) is used to optimize the coupling of light from the taper into the cavity. Finally, with the correct power and polarization one can obtain the optical spectrum of the cavity by sweeping the laser wavelength while monitoring the output transmitted light. Figure 3.3 shows an example of the typical data obtained using either a DAQ or an oscilloscope.

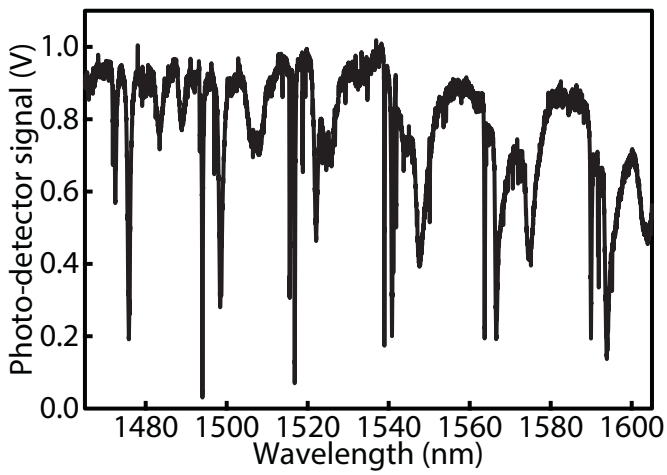

Figure 3.3: **Data of an optical transmission spectrum with uncorrected wavelength axis.**

It is important to note that to obtain reliable data one should sweep the laser slowly, such that the energy change in the cavity while the laser frequency passes by the optical resonance is adiabatic. By slowly we mean that the laser frequency has to stay quasi-static for at least the typical time-scale of the cavity (τ), which is characterized by its total decay rate

$\kappa = 1/\tau$. The effects of a fast sweeping measurement, such as rapid wavelength dependent oscillations of the transmitted power, can be found in reference [71]. For the cavities shown in this work speeds on the order of 1 nm/s to 10 nm/s are typically used and result in good quality data, without distorting the resonance dips.

Note, however, that the wavelength axis on figure 3.3 was obtained by constructing a linearly spaced vector with the same amount of elements as there are points in the acquired dataset. That is because the laser position is read by an electric output of the laser, which is a voltage proportional to the laser wavelength and, as can be seen in the example in figure 3.4, this output presents two main problems: 1) the start and stop times are not very well defined because the curve has smooth start and stop regions (marked in red); 2) the curve is not a perfect straight line, as expected if the laser sweeping speed was considered constant.

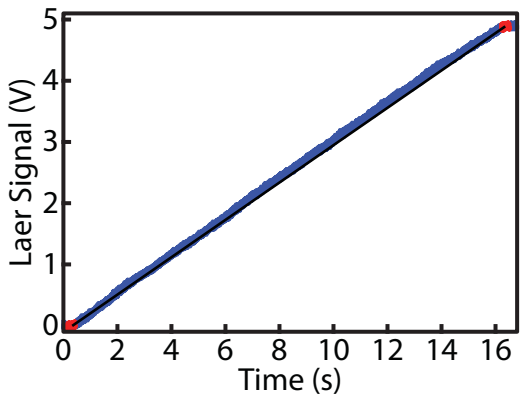

Figure 3.4: **Laser output voltage for wavelgnth reference.** Colored lines are data, while the black line is a straight line reference connecting arbitrary initial and final points. In red the region where start and stop wavelength must be defined.

This creates a problem for defining the start and stop wavelength and to rely on the exact wavelength spacing between points. Hence if one wants to determine the precise position of the resonances or the dispersion of the modes, which involves correctly determining the distance between modes of a given family (free-spectral range – FSR), a process for correctly determining wavelength axis of the data is needed.

Wavelength correction

To correctly determine the resonant wavelengths of the cavities, two references are used. A fiber based Mach-Zehnder interferometer (MZI) with known FSR is used as a relative reference. And an acetylene cell (AC) is used as an absolute reference, as its absorption lines positions have been precisely characterized and easily found in literature [72] (see appendix B for the spectrum used in this thesis). In order to guarantee that the signal of these references doesn't depend on the cavity input power, 0.5% of the laser output power for each reference is separated before the VOA.

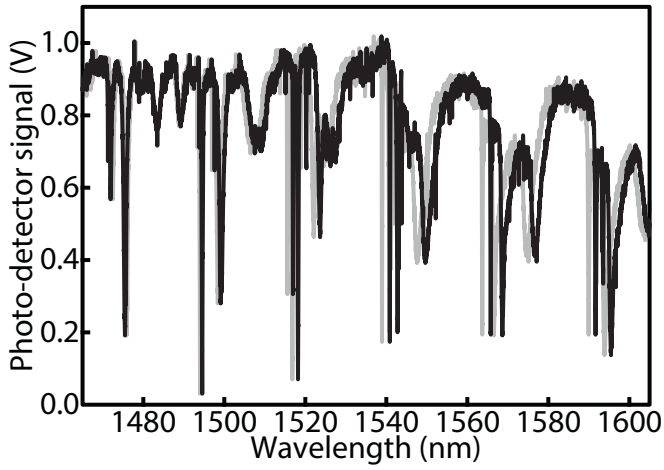

Figure 3.5: **Data of an optical transmission spectrum with corrected wavelength axis.** The gray shade behind is the raw data of fig. 3.3.

Assuming that the MZI has a fixed FSR along the whole spectrum span, which is reasonable as it is expected to vary by about 0.1% from 1460 nm to 1616 nm due to optical fiber chromatic dispersion, its signal is used to correct the wavelength vector used to plot the cavities' data. For that, the minima and maxima of the MZI signal are counted and a frequency vector is created, with the same amount of points equally separated by one interferometer FSR from each other. Then, to obtain the correct absolute wavelength, this frequency vector start point is shifted such that the AC resonances are in the correct position. After correcting for both relative and absolute wavelength variations we obtain spectra like the one shown in figure 3.5. Notice the difference between the corrected (black) and the naively generated wavelength (gray) data.

Normalizing the spectrum

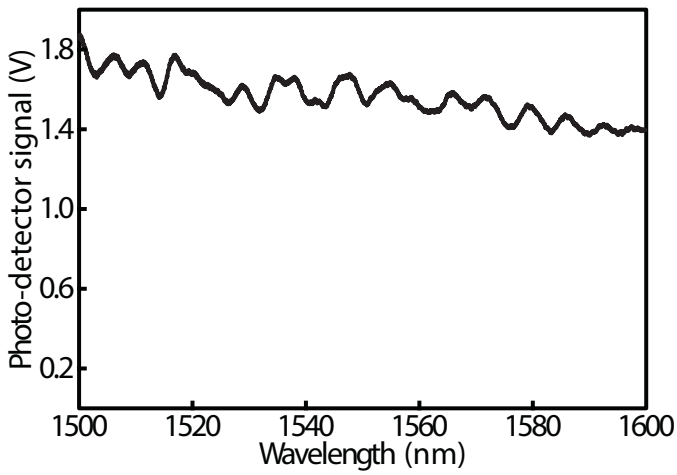

Figure 3.6: **Raw data of a taper fiber waveguide spectrum.**

Note that the transmission background is nor smooth neither constant. That is because the taper transmission is not smooth, as can be seen in figure 3.6. These data were taken

while the taper was far from the sample, hence all features are exclusively due to the taper, as the laser is know to be very stable in this wavelength range. These variations can be explained by different reasons, such as scattering in particles or defects on the taper; also, the taper is mounted with a loop on its thinnest part (see appendix F) where scattering may also take place. However, these causes were not investigated as it is beyond the scope of this work.

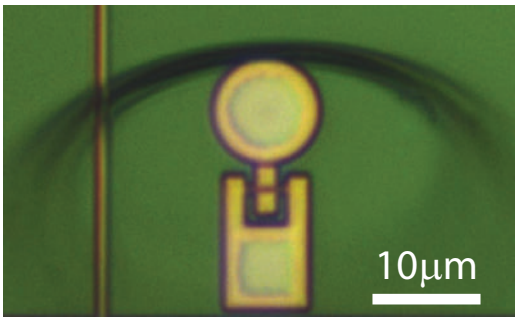

Figure 3.7: **Example of a taper coupled to an optical cavity.** Usually the taper either touches the cavity or some structure close to it, such as the vertical suspended silicon bridge on the left of the NFO.

One could readily suggest to divide the cavity signal by the taper's, both normalizing and removing the taper influence in the former. However, the taper transmission can only be obtained with the fiber far from the sample, while the cavity data is taken with the fiber touching either the cavity (fig. 3.7) or some structure close to it, as stated before. The fact that the taper touches the sample reduces the overall transmitted signal by approximately 2 dB, besides potentially creating new features in its spectrum. This makes it impractical to use its spectrum to normalize the cavity's.

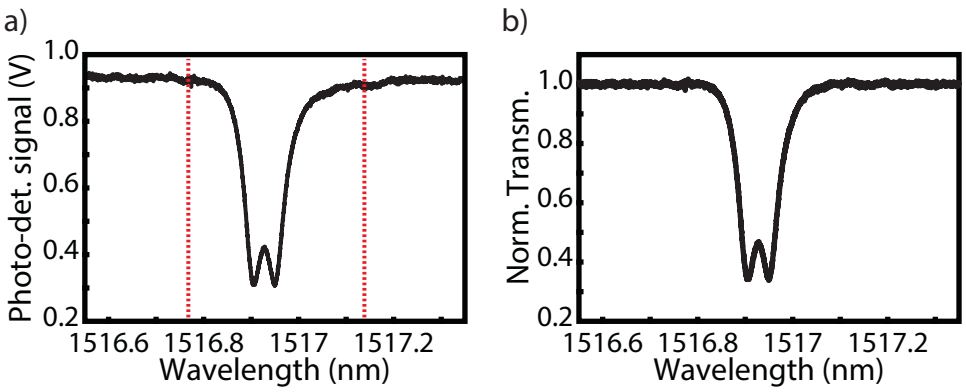

Figure 3.8: **Normalization of a single resonance spectrum.** a) Resonance with corrected wavelength but non-normalized. b) Same resonance from (a) but after normalization.

Another way to normalize the resonance is by obtaining its background separately by fitting it with a polynomial function. Of course this must be done for each resonance, independently, since it is practically impossible to solve this problem to the whole spectrum at once because the resonance dips vary in broadness and depth. In order to perform this background fitting it is necessary to isolate the resonance, cutting it out of the data in points like those shown

in figure 3.8a. The a polynomial function, which in this case could very well be a simple straight line, can be fitted to the remaining data. Figure 3.8b shows the result of dividing the original data by this fitted function. Now it is possible to fit the theoretical transmission function to the cavity data and obtain its resonance properties. Moreover, with the corrected wavelength it is also possible to correctly determine the resonances dispersion by identifying the related modes and calculating their distance in the spectrum.

3.2. Room conditions, vacuum and cryogenic measurements

Room conditions

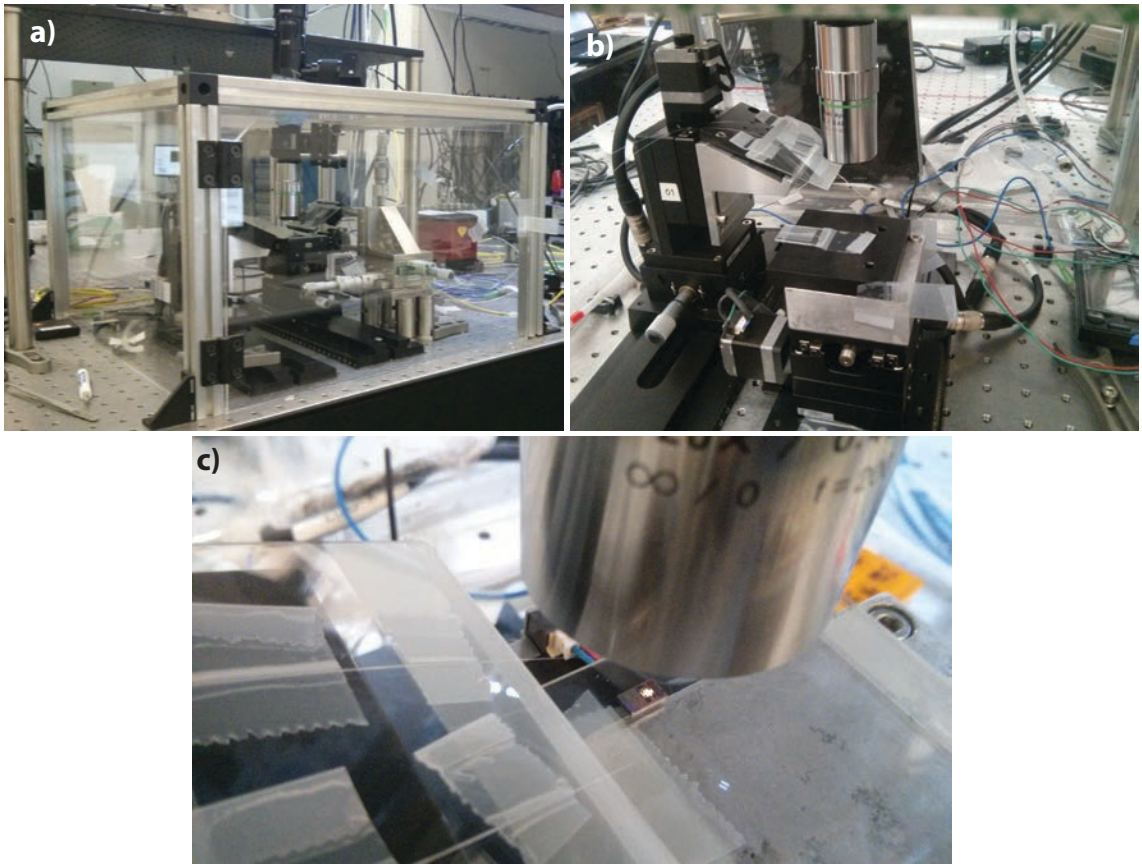

Figure 3.9: **Room conditions measurement setup.** a) Overview of the partially sealed box with positioning motors for sample and taper, constantly purged with nitrogen gas. b) Detail of the moving stages with the microscope objective (20x in this case); the taper is held on the glass blade sticked to the vertically moving stage on the left. b) Detail of a sample with the taper touching a device.

Because the taper is very thin (about 1µm in diameter) it is very susceptible to the environment, such that its transmission loss may increase due to adsorption of contami-

nant molecules, such as water. To decrease such a degradation, increasing the taper life-time, all room condition (293 K and atmospheric pressure) measurements are performed inside a partially sealed box with a constant flux of nitrogen gas (fig. 3.9a). This increased the taper life-time from less than a week to over a month, even though the nitrogen flux is off during experiments to avoid the motion of gas causing motion of the taper.

To correctly position the taper close to the devices in the sample, precision motors by Suruga Seiki Co. are used to move the sample on the horizontal plane, while the taper moves in the vertical direction. A microscope is used to image the systems under test, with a camera attached to it allowing for real-time video and photo recordings when necessary. To facilitate the imaging process the microscope is held on a (x, y, z) stage whose vertical axis is controlled by a step-motor, while the (x, y) motion is made manually. This allows for fast and automatic focus corrections, while minimizing vibrations on the table. The hole setup is mounted on an optical table suspended by pneumatic isolators, all fabricated by Newport.

Vacuum and cryogenics

Although the optical measurements do not suffer from problems related to the air around the devices, the same does not hold for the mechanical resonators studied in chapter 4. The mechanical motion, as demonstrated in appendix E, can be severely damped by the air viscosity, completely impairing the resonator's operation. To avoid this, the optomechanical devices are tested inside the vacuum chamber shown in figure 3.10, which has a cold-finger cryostat inside that also allows for cryogenic temperature measurements. This increases the typical mechanical quality factor of the a given mechanical mode from 650 to almost 10k.

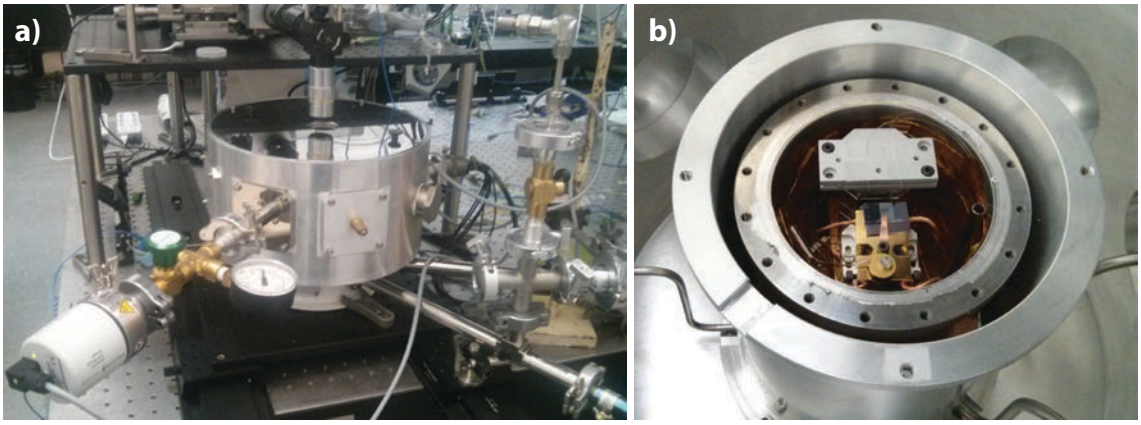

Figure 3.10: **Vacuum and cryogenic measurement setup.** a) A vacuum chamber on top a cold-finger cryostat allows for vacuum and low temperature measurements. On top a microscope with a 10x objective allows for sample imaging through a sapphire window. b) Detail of the inside of the chamber, with a sample clamped on the sample holder, close to a thermometer (screwed to the holder), and the taper on top.

This system is composed by an ST500 cold-finger cryostat around which two vacuum chambers were assembled. The entire system but the aluminum taper-holding pieces was

designed by professor Thiago Alegre, a member of the group, and assembled by Janis Research Company. The system has two chambers because it was thought to allow the injection of helium gas inside the inner one, while the outer one is kept in vacuum. This is interesting because it will allow for quicker and better cooling of the samples. However, this feature was not used for the measurements presented in this thesis.

Inside the inner chamber structure (number 1 in figure 3.11) is in direct contact with a cold finger, which is cooled by liquid helium. On top of this structure a series of Attocube stages (number 2 in figure 3.11) allow for precise positioning of the taper on the devices, while the entire system is imaged by a microscope through sapphire windows (number 3 in figure 3.11). To optimize the cooling performance of the system, the structure below the positioners and the sample holder on top are gold plated; copper braids are also attached to the sample holder to reduce thermal impedance from the sample to the cold finger.

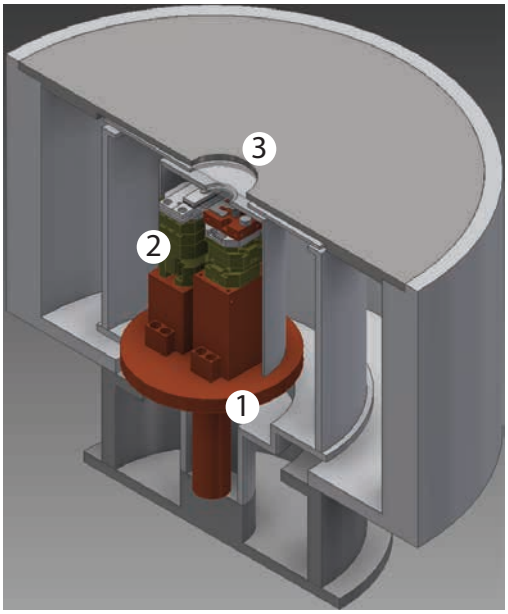

Figure 3.11: **CAD of Vacuum and cryoogenic measurement setup.** CAD showing a cut view of the inside of the cryostat's chamber. Number 1 marks the structure created to support and conduct heat from the positioning stages, marked as 2, and samples. Number 3 marks sapphire windows that allow imaging of the sample during measurements.

During the measurements, both in vacuum and cryogenic temperatures, we kept the inner chamber open, as no gas helium buffer was used, and pumped the whole system through the outer chamber outlet. Good high vacuum pressures ($\approx 1.5 \times 10^{-5}$ mbar) were achieved using a Pfeiffer pump station (HiCube 80 Eco). When the cold-finger is cooled down to 4.7 K, close to liquid helium boiling point, the pressure reaches the 10^{-7} mbar scale due to the cryopump effect, which reduces the amount of free particles inside the chamber by trapping them in the cold-finger region.

Because of the reduced size of the taper holder of this chamber, if compared to the room conditions glass holders, the taper has to be shorter than those used in the latter. While the room conditions tapers have tapering regions almost 4 cm long, those used in the vacuum

chamber are about 25% shorter. This is enough to increase coupling of the light coming from the SMF into higher order modes of the tapering region. Moreover, the waist region for the cryostat taper is intentionally not single mode, increasing its stiffness to reduce oscillations caused by the moving stages, which cause difficulties on coupling the taper to the cavity and whose causes are commented further in this section. This results in lossier tapers; while the room conditions tapers can have less than 1 dB of insertion loss, the vacuum ones have at best 1.5 dB insertion loss.

Also, residual absorption due to substances adsorbed on the taper surface also causes the taper to heat and, because of the lack of air inside the chamber to dissipate this heat, the taper may be damaged. This greatly limited the capabilities of testing our samples in vacuum conditions, as the input laser power could not exceed approximately 1 mW. This could be resolved by cleaning the taper before inserting it into the chamber, but we use tapers with a loop to guarantee that it touches only one device at a time, and this loop comes undone in the cleaning process. Hence we have to further manipulate the fiber after cleaning, which is enough to hinder the cleaning process.

Another challenge we encountered on the vacuum and low temperature measurements was positioning the taper on the device. The Attocube stages move all by piezo-actuated motors, with the coarse motion being executed using the slip-stick principle [73]. In this type of motion drive a mass moves slowly part of the cycle, caring another mass with it through static friction; at the end of the cycle this mass rapidly returns to its initial position, such that the inertial force of the second mass is larger than the friction, what results in the second mass staying put at the final position. This principle is the same of the table-towel trick, in which a swift pull of the towel leaves everything on the table at their original position, while a slow pull will carry the objects with the towel.

This kind of motion causes the taper to vibrate, making the positioning very difficult due to the lack of air to damp the oscillations that last for a considerable amount of time. The solution to this is to use another stage to realize the fine positioning, which moves only by stretching or contracting a piezoelectric component. But this also presented vibrations, although much weaker than the coarse motion stages, because the change of on the driving voltage of the piezoelectric component was discrete with minimum steps of 10 mV instead of continuous. And this change of 10 mV was enough to also cause small vibrations that, although they do not hider the experiment, make it harder to correctly land the taper on the sample.

3.3. Radio-frequency spectra readout

Now, the devices presented in this thesis have optical modes that are perturbed by different phenomena. In chapter 4 the optical modes are perturbed by the periodic motion of a mechanical resonator through the optomechanical interaction, while on the devices presented in chapter 5 the resonances are perturbed by the periodic variations of temperature and free

charge-carrier density. These perturbations manifest themselves first as oscillations of the optical resonant frequency, which in turn result in periodic oscillations of the transmitted light intensity. This transduction depends on the detuning between the input laser frequency and the cavity resonance frequency (Δ), the relation between the total optical decay rate (κ) and the frequency of the perturbing phenomenon (Ω) and on the detection scheme used [74].

The transmitted light, when detected by a photodetector, produces a photocurrent whose spectral density carries the information of the mechanism causing the perturbations on the optical resonance. For the optomechanical case, for example, the spectral density of the photocurrent can be expressed as

$$S_{II}(\Delta,\Omega) = F(\Omega)\, K_{D,H}(\Delta,\Omega)\, G_{\mathrm{OM}}^2\, S_{xx}(\Omega)\, P_{in}\ , \tag{3.1}$$

where $F(\Omega)$ is the photodetector gain, G_{OM} is the coupling rate of mechanical motion to optical resonance shift, $S_{xx}(\Omega)$ is the mechanical displacement spectral density, P_{in} is the input optical power and $K_{D,H}(\Delta,\Omega)$ is a transduction function dependent on the measurement scheme and the detuning between the pump laser and the optical resonance (Δ), which will be explained later in this section. This expression is easily extended to other phenomena by substituting other coefficients, such as the coupling of temperature or free-carrier density to the optical resonance, for the optomechanical coupling rate (G_{OM}).

Also, the relation between Ω and κ defines two regimes of operation for the transduction performed by the cavity. These regimes are called resolved sideband regime when $\Omega \gg \kappa$ and unresolved sideband regime when $\Omega \ll \kappa$ [31]. In this thesis all the frequencies measured for the fluctuations of the transmitted light intensity are on the tens of MHz scale, while the cavity decay rates are always on the GHz scale, which leaves all the phenomena studied in the unresolved sideband regime ($\Omega \ll \kappa$).

Direct detection

The simplest measurement scheme is the direct detection. In this scheme the output light of the cavity is measured by a single photo-detector. The experimental setup for this type of measurement (fig. 3.12) is very similar to the one showed for the optical characterization. A tunable laser light is coupled into a taper after passing through a variable attenuator and a polarization controller. The transmitted light is collected by a photo-detector (NewFocus 1617AC) whose response-time is smaller than the period of the signal we want to measure; e.g., if we want to test a system whose RF signal is in the 100's of MHz scale we should use a detector that responds at least at those frequencies, ideally higher. In the experiments presented in this thesis, signals that span up to 500 MHz are measured, while the detector used has a nominal cutoff frequency at 800 MHz. The photocurrent output of the detector is measured with both an oscilloscope (Agilent's DSO9254A) and an electrical spectrum analyzer (ESA –

Agilent's N9030A PXA Signal Analyzer).

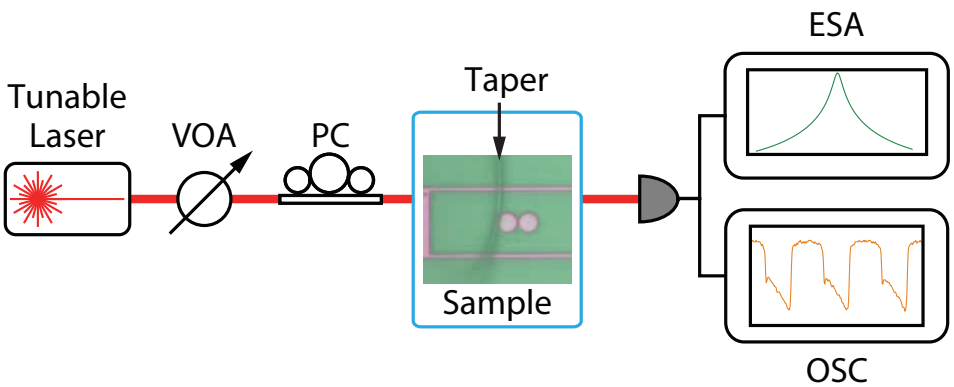

Figure 3.12: **Schematics of experimental setup for direct detection of RF signals.** BS: beam-splitter; VOA: variable optical attenuator; PC: polarization controller; ESA: electrical spectrum analyzer; OSC: oscilloscope.

As mentioned before, the photocurrent of the detector is proportional to the incident optical power, which in turn depends on the transduction of the optical resonance modulation to the transmitted light intensity. For the direct detection scheme, in the unresolved sideband regime ($\Omega \ll \kappa$), the transduction can be expressed by

$$K_D(\Delta,\Omega) = \frac{4\Delta^2\ (\kappa-\kappa_e)^2\ \kappa_e^2\ \Omega^2}{\left(\Delta^2+(\kappa/2)^2\right)^4}, \tag{3.2}$$

where K_D is the cavity transduction coefficient, $\Delta = \omega_l - \omega_0$ is the detuning between the input laser angular frequency (ω_l), and the cavity resonance angular frequency (ω_0), $\kappa = \kappa_i + \kappa_e$ is the total optical decay rate given by the sum of the intrinsic cavity decay rate (κ_i) with the coupling with the waveguide (κ_e) and Ω is the optical resonance perturbation frequency. For more details on the equations for optical transduction of the cavity resonance to the optical field we refer to Felipe's PhD thesis [56] and to reference 74.

Noticeably this function is zero for $\Delta = 0$, while attaining its maximum value at $\Delta = \pm\kappa/\sqrt{12}$ (see fig. 3.13). For the measurements presented in chapter 5 this has little impact, as the measurements are all made varying the input laser frequency and it is always blue-detuned ($\Delta > 0$) with respect to the cavity resonance. Also, it is important to note that this function was obtained by assuming that the amplitude of modulation of the optical resonance ($\delta\omega_0$) is very small, i.e., $\delta\omega_0 \ll \kappa$. And, as it will be shown in chapter 5, this is not the case for the oscillations caused by temperature and charge-carriers density variations. Hence, this analysis can't actually be done for that experiment, although direct measurement is used.

For the optomechanical case presented in chapter 4, on the other hand, this transduction function is valid, as the mechanical motion probed through the optical field has very little amplitude as a result of the sample having a finite temperature, causing very small amplitude oscillations of the optical resonance frequency. However, in that case we are interested in

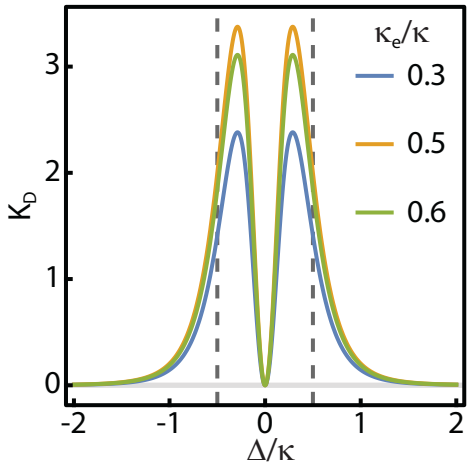

Figure 3.13: **Direct detection transduction coefficient as a function of laser detuning.** Vertical dashed lines mark $\Delta = \kappa/2$. The colors indicate the cavity-waveguide coupling regime, for a single port cavity: blue – undercoupled; yellow – critically-coupled; green – overcoupled.

obtaining intrinsic (bare) mechanical properties of the resonator and, for $\Delta \neq 0$, optomechanical feedback affects both the mechanical damping rate and frequency [31, 75, 76] (see also my Master's degree dissertation [77]). For that it would be desirable to measure the optomechanical signal with the laser frequency to the optical cavity resonance.

Homodyne detection

One way to produce non-zero optical transduction at $\Delta = 0$ is by using the Hansch-Couillaud scheme [78]. This scheme uses the fact that the modes of the optical cavity are polarization dependent to create a Mach-Zehnder interferometer. The system of interest is in one of the of the polarizations (one of the arms – signal) and the other polarization becomes a phase reference (or the local oscillator – LO). In our measurements this is accomplished by using an in-fiber polarization controller (PC) to control the polarization of the optical cavity input light, such that just a fraction of it couples into the optical mode of interest, with the remaining light becoming the LO (see fig. 3.14). This process can be understood in terms of projection of the polarization of the light. If the cavity mode preferential polarization is, let us say, in the horizontal one, then the input light will be mostly vertical, such that the projection of the total polarization in the vertical direction is much larger than in the horizontal direction. Then, if the input light had a linear polarization, i.e., the phase difference between LO and signal is zero, after the cavity the total transmitted light will have an elliptical polarization, becasue the signal gains an extra phase by coupling into and out of the cavity.

By passing this elliptically polarized light through a second PC the major axis of the elliptical polarization is rotated, such that when it passes through a polarizing beam-splitter (PBS) the vertical and horizontal components are separated in two linearly polarized beams, with orthogonal linear polarization and equal intensity. In this last step, because LO and signal

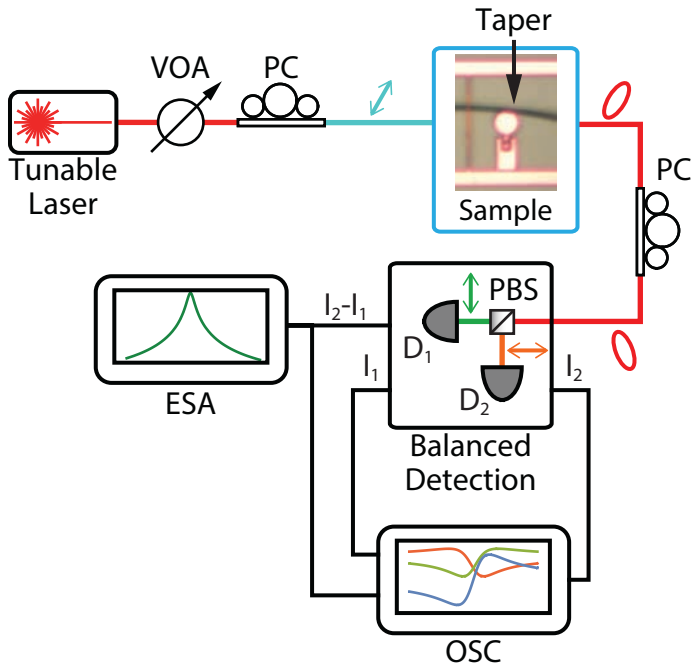

Figure 3.14: **Schematics of experimental setup for homodyne detection of RF signals.** BS: beam-splitter; VOA: variable optical attenuator; PC: polarization controller; PBS: polarizing beam-splitter; ESA: electrical spectrum analyzer; OSC: oscilloscope. Green and orange polarizations indicate the separation between signal and local oscillator (LO). The cyan path indicates the path in which signal and LO interfere.

are set to the same polarization in each output port of the PBS, they can interfere and this interference pattern is then detected by a pair of photo-detectors, whose photocurrents are measured in a differential scheme ($I_2 - I_1$). This setup is very similar to a homodyne detection scheme, missing only the ability to freely chose the phase of the local oscillator arm (polarization out of the cavity – LO).

The cavity transduction coefficient for this detection scheme, on the unresolved sideband regime, is given by

$$K_H(\Delta,\Omega) = \frac{\left(\kappa\ (\kappa - 2\kappa_e) - 4\Delta^2\right)^2\ \kappa_e^2\ \Omega^2}{\left(\Delta^2 + (\kappa/2)^2\right)^3 \left(4\Delta^2 + (\kappa - 2\ \kappa_e)^2\right)} \tag{3.3}$$

and its detuning dependency can be more clearly seen in figure 3.15. In this case the transduction is not only different than zero but also maximum for $\Delta = 0$, which allows us to probe the optomechanical devices' mechanical properties without any effect of optomechanical feedback. We call attention to the fact that the these curves were generated for a single port cavity, in which $\kappa_e = \kappa/2$ is possible and results in the cavity-waveguide critical-coupling regime ($\kappa_e = \kappa_i$); for a two port cavity $\kappa_e = \kappa/2$ is an impossible condition and the critically-coupled regime results from $\kappa_e = \kappa/3$. Hence the zero transduction at $\Delta = 0$ for the critically-coupled regime is only possible for single-port cavities. Again we point to reference 74 for more details on the deduction of this expression.

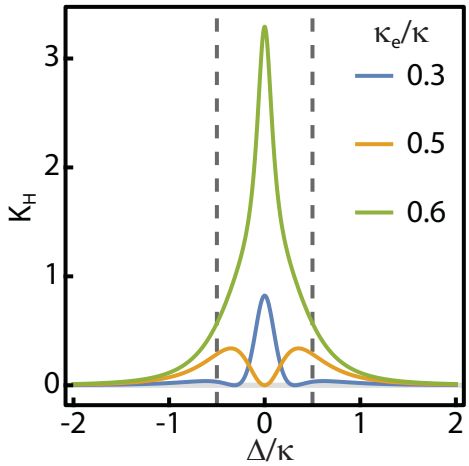

Figure 3.15: **Homodyne detection transduction coefficient as a function of laser detuning.** Vertical dashed lines mark $\Delta = \kappa/2$. The colors indicate the cavity-waveguide coupling regime, for a single port cavity: blue – undercoupled; yellow – critically-coupled; green – overcoupled.

In our case the photo-detector pair used is the NewFocus's 1617AC system, comprised of two photo-detectors connected to a differential amplifier, all in the same chip to reduce the mismatch of the two detectors. This detector system has three DC outputs, two that give the DC photocurrent of each detector (I_1 and I_2) and one that gives the DC component of the difference between these photocurrents ($I_2 - I_1$). These DC outputs are all measured in an oscilloscope (Agilent's DSO9254A) with the laser frequency sweeping over the resonance, which allows for proper adjustment of the polarization controllers (PC). To adjust the input PC the cavity resonance is monitored on the computer, with the transmitted light detected with a power-meter in the same manner presented in section 3.1. For this adjustments the laser frequency is swept in a short range, just enough to cover most of the optical resonance, using an internal piezoelectric motor of the laser system. Figure 3.16 shows the resulting detuning dependent transmission of I_1 and I_2 (green and orange), their sum (black) and difference (yellow) obtained experimentally (a) and from the transfer matrix analytical model (b – see appendix C).

Note that the optical resonance presents two peaks, result of the coupling of counter-propagating modes. Nevertheless this doesn't impair the correct adjustment of the PC's to obtain the correct transmission signal, although it requires previous understanding of the expected signal in this case, which is possible by comparing the experimental data to the theoretical analytical traces (fig. 3.16).

A fourth output in the 1617AC system gives only the AC component of the $I_2 - I_1$ signal. This output is measured with an ESA (Agilent's N9030A PXA Signal Analyzer) and its data treated to obtain the mechanical properties of the optomechanical system.

But allowing measurements with zero detuning it not the only advantage of this detection scheme. As Agrawal demonstrates in his book [79], the homodyne detection can also increases the signal to noise ratio (SNR) of the measurement by a factor 2. This is because the power on the photo-detectors are typically dominated by the power of the local oscillator,

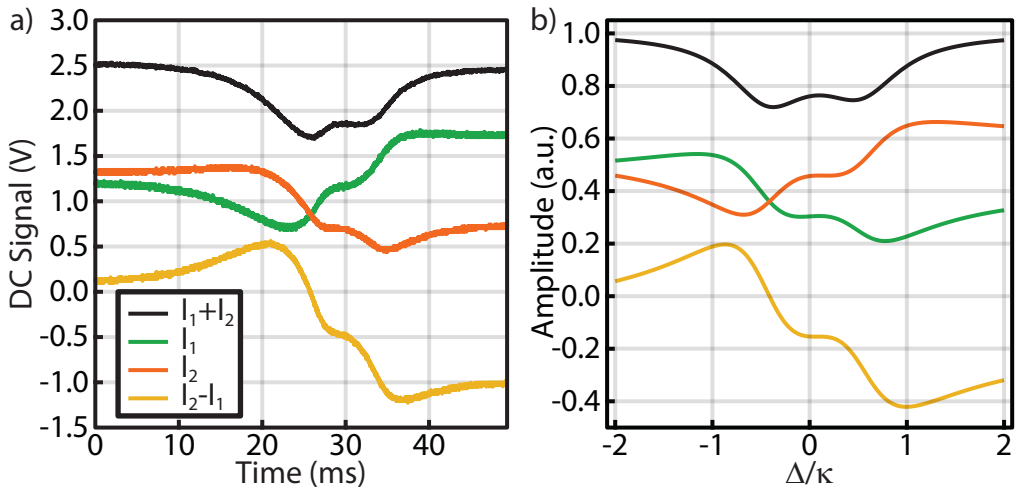

Figure 3.16: **Signals on the outputs of a homodyne detection scheme.** a) Experimental signals for the DC photocurrents (green and orange), their sum (black) and difference (yellow) when the laser frequency is varied over a resonance. b) Result of the analytical model of the PBS output signals.

which can lead to the detection noise being dominated by shot-noise (noise originated from the corpuscular nature of light) instead of thermal and electronic noise, if the LO power is made high enough.

3.4. Mechanical spectra

Once the signal in figure 3.16 is set, the laser is tuned to the center of the resonance, which results in the difference DC signal going to zero. Then we are able to measure the RF spectrum due to the mechanical motion, without optomechanical changes to the mechanical resonant frequency or damping rate. Figure 3.17 shows an example of a 20 MHz span of the power-spectral-density (PSD) obtained for the optomechanical devices we studied. The smaller peaks close to 40 MHz and 56 MHz are due to mechanical modes, which can be identified comparing their frequency to numerical simulations. The sharp, intense peak close to 56 MHz is due to a phase modulation imprinted in the input laser before it is coupled to the optical cavity. The modes we study in chapter 4 are those close to 56 MHz.

This measurement, as well as all similar measurements, is performed accumulating and averaging 50 spectra, which is automatically done by the ESA. The validity of fitting this averaged dataset was assessed by taking the ESA averaged signal and applying the bootstrap fitting method [80]; then, 50 independent non-averaged spectra were obtained and fitted separately. Because the average of the independently fitted parameters, as well as their standard deviation, resulted in the same values (less than 1% variations) as the bootstrapping method, we concluded that the averaged data is very reliable.

The phase modulation peak is used to measure the vacuum optomechanical coupling rate [31, 74]. Also, we can use this measurement to convert the electrical power-spectral-

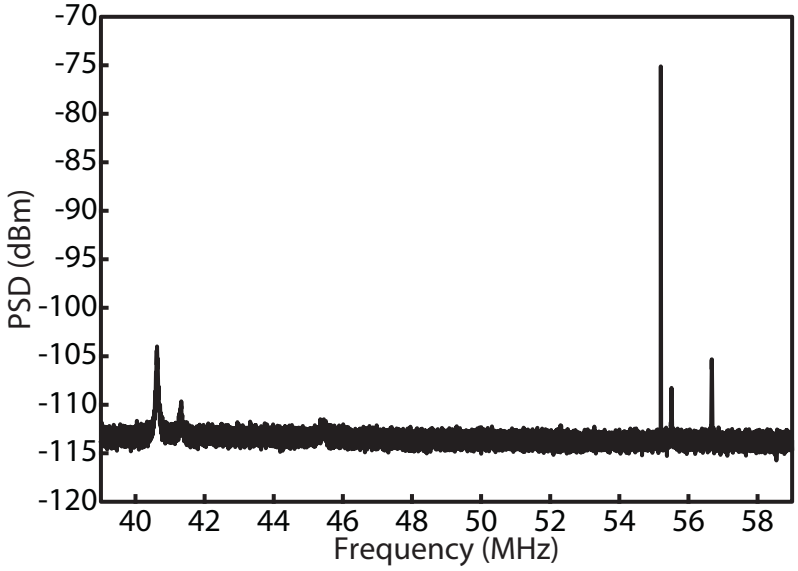

Figure 3.17: **Experimental power-spectral-density of a near-field optomechanical device.** The peaks smaller peaks close to 40 MHz and 56 MHz are due to different mechanical modes. The sharp, intense peak close to 56 MHz is due to a phase modulation of the input laser.

density to a displacement spectral-density, which gives us the notion of displacement sensitivity in our experiment. The detailed derivation of the relationship between the phase modulation and mechanical peaks can be found in reference [74]. In summary, the mechanical motion causes a phase-modulation (PM) of the light stored in the cavity, which is then converted to an amplitude-modulation (AM) by the cavity itself. What Gorodetsky *et al.* [74] have shown is that one can obtain the vacuum optomechanical coupling rate by comparing the amplitude of a known PM passing through the cavity to the signal due to the optomechanical interaction. Moreover, this technique eliminates the necessity of absolute knowledge of all losses, couplings and transfer functions of the measurement setup and optical cavity, reducing systematic errors. The expression that summarizes that work is

$$g_0^2 = \frac{1}{2n_m}\frac{\phi_0^2\Omega_{PM}^2}{2}\frac{S_{II}(\Omega_m)}{S_{II}(\Omega_{PM})}\frac{\Gamma_m/4}{ENBW}, \tag{3.4}$$

where g_0 is the vacuum optomechanical coupling rate [31], n_m is the phonon occupation at the mechanical mode's frequency Ω_m, ϕ_0 and Ω_{PM} are the amplitude and the frequency of the PM, Γ_m is the decay rate of the mechanical mode, $ENBW = RBW\sqrt{\pi/(4log(2))}$ is the effective noise bandwidth determined by the resolutions bandwidth (RBW) of the spectrum analyzer and $S_{II}(\Omega)$ are the current spectral-densities at the frequencies of the mechanical mode and PM.

The only parameters that must be known besides the data obtained from the PSD measurement are the temperature of the sample, to calculate the phonon occupancy at the mode's frequency (n_m), the amplitude of the PM (ϕ_0), which can be calculated from the modulators drive voltage once the modulators V_π is known, and the spectrum analyzer's RBW, which is typically set by the person realizing the experiment. Although the expression uses the elec-

trical current spectral-density (S_{II}) for both mechanical and modulation signals, they are both measured at the same time with the same equipment that gives the electrical power spectral-densities, which is proportional do the current.

To obtain the properties of the mechanical spectral density we fit the function

$$S_{II}(\Omega) = 10^{S_b/10} + \frac{10^{S_0/10}\,\gamma_m^2\,\Omega_m^2}{\left(\Omega_m^2 - \Omega^2\right)^2 + \gamma_m^2\,\Omega^2} \tag{3.5}$$

to the data of the ESA. In this function S_b is the background noise considered to be frequency independent as no phase noise around the signals measured is expected, $S_0 = S_{II}^{meas}(\Omega_m)$ is the peak signal at the mechanical angular frequency Ω_m and γ_m is the mechanical damping rate. Note that the ESA data is obtained in log scale (dBm/Hz), hence the powers of 10 to convert $S_{b,0}$ to linear scale (W/Hz).

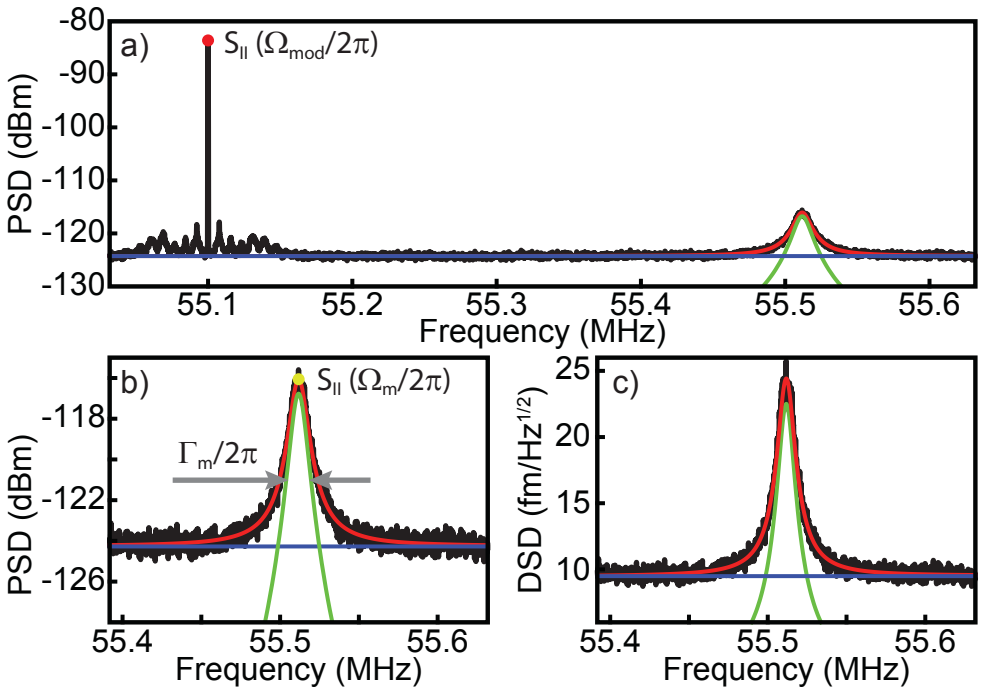

Figure 3.18: **Calibration of the power spectrum into displacement signal.** a) Original data with modulator signal to the right and mechanical signal to the left. b) Zoom in the mechanical signal indicating the relevant parameters. c) Calibrated displacement spectral density (DSD). In all graphs the lines are fitted functions: blue is the background noise, green the function of the mechanical signal and in red the total function fitted to the data.

The measured g_0 is then used to translate the PSD data into mechanical spectral density. For that one must obtain the optomechanical coupling rate, $G_{OM} = g_0/x_{zpf}$, where $x_{zpf} = \sqrt{\hbar/(2m_{eff}\Omega_m)}$ is the displacement quantum zero-point-fluctuation, with m_{eff} being the mechanical mode's effective mass. The effective mass is determined from numerical simulations of the mechanical modes. In our case this is done using the commercial package COMSOL®. Figure 3.18 shows the original PSD data, with equation 3.5 fitted to the mechanical peak, before and after calibrating the vertical axis.

Chapter 4

Suppression of Anchor Loss Through Destructive Interference of Elastic Waves

The interaction of optical and mechanical fields in microscale devices enables the manipulation and control of mechanical modes vibrating at radio-frequencies. Some remarkable examples resulting from such an optomechanical interaction include the preparation and measurement of harmonic oscillators' quantum ground states [8, 81, 82], optically induced synchronization between mechanical oscillators [12], phase noise suppression [13] and highly sensitive sensors [83–86]. A major limitation in these microdevices is mechanical energy loss that leads to reduced sensitivity [87], lower coherence [31], and increased power consumption [88]; it also remains among the most challenging issues in micromechanical devices, depending on design and fabrication processes.

This chapter presents an optomechanical device whose mechanical dissipation is limited by material and surface related mechanisms. The main loss channels are determined by testing the devices in vacuum, at room and cryogenic (20 K) temperatures. Results related to the operation of the devices at room conditions (293 K and atmospheric pressure) will be left to appendix E, as the problem of air damping is already well documented in the literature [89–94].

4.1. Device presentation

This device is part of a near-field optomechanical (NFO) system based on a mechanical resonator that interacts with a nearby silicon micro-disk optical cavity (fig. 4.1). The mechanical resonator is composed by two square paddles (2 µm × 2 µm), attached on both sides to suspended beams through 4 nanostrings (200 nm wide) separated by a 200 nm gap. They are fabricated following the steps detailed in chapter 2, with devices defined on the SOI platform by the IMEC foundry, and the mechanical degrees of freedom granted by wet etching performed at the Device Research Laboratory's clean room, at UNICAMP's Physics Institute. Because the mechanical device's structure is completely detached from the optical cavity's, we are able to design the former without any changes to the latter. Then, in order to reach a perfect balance between mechanical waves radiating to the supporting beams, the length of the back paddle (L) is offset from the front one by a small length δ (see fig. 4.1a). Each chip fabricated by the foundry has a series of devices where the back paddle has its length varied, while the front paddle's is fixed and the optical cavity is nominally the same for every different mechanical device. This

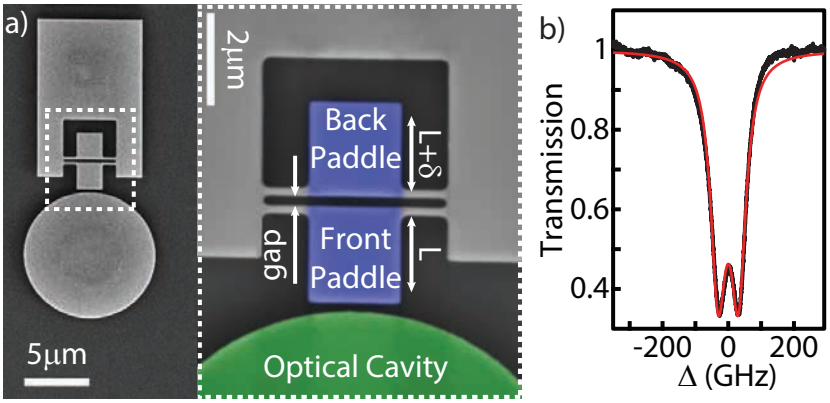

Figure 4.1: **Scanning electron microscopy and optical resonance of the near-field optomechanical device.** a) On the left an overview image of the paddles and the optical cavity microdisk. On the right a zoom in the region marked on the left, with the false color highlighting the paddles (blue) and the cavity (green). The names of the paddles are used to refer to each one of them throughout the chapter. The front paddle is 200 nm away from the disk border. The gap between paddles is of 200 nm and the initial paddle length L is 2 µm, with δ being a symmetry breaking parameter. In this image $\delta = -50$ nm. b) Typical optical resonance used to probe the mechanical motion of the paddles. The center wavelength is $\lambda_0 = 1516.93$ nm with a loaded optical quality factor $Q_{opt} = 35$k.

back paddle asymmetry is varied from $\delta = -200$ nm up to $\delta = 200$ *nm*, in 25 nm steps.

The devices are designed such that the front paddle is 200 nm away from a 5 µm radius disk optical cavity. This optical cavity supports whispering gallery modes (WGM) [28], whose electromagnetic fields are mostly concentrated on the disk's edge. Figure 4.1b shows the transmission of a low power laser ($\approx$ 500 nW) whose frequency was varied over one of these resonances. This resonance presents a split dip due to the coupling of counter-propagating modes, which can be caused by roughness on the disk's border [70] and the presence of the paddle. Nevertheless, these resonances present high loaded (total) quality factors of approximately 35k (55k - intrinsic), obtained by fitting the function of the transmission of coupled resonances (see appendix A) to the data. This optical spectrum had its frequency axis calibrated following the procedure presented in chapter 3, section 3.1.

4.2. Numerical simulation

Because the supporting beams couple the paddles' motion, symmetric (S) and antisymmetric (AS) combinations of individual paddle modes are formed, such as the in-plane modes shown in the finite element method (FEM) [95] numerical simulation of figure 4.2a. These simulations were all performed using the commercially available package COMSOL®. The color code for S (blue) and AS (red) modes will be used throughout the entire chapter.

FEM calculations of the mechanical modes show that the resonant frequencies of the coupled mechanical modes display the avoided crossing behavior when δ is varied (fig. 4.2b), a signature of coupling of the paddles' motion (see sec. 4.3 and reference [96]). The resonances

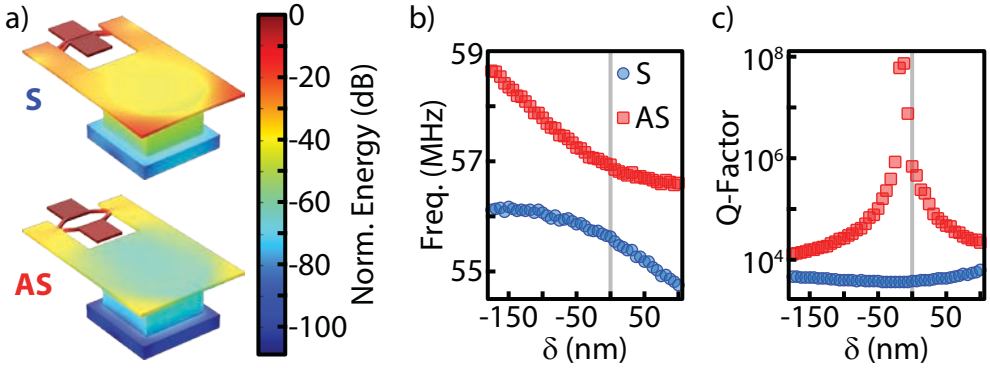

Figure 4.2: **Finite element method simulations of the coupled paddles mechanical resonator.** a) Mode shape of the mechanical modes of interest. The color scale indicates the total mechanical energy distribution throughout the device, normalized by the maximum, with the same log-scale for both S and AS modes. b) Real part of the eigenfrequency for each mode for various values of paddle asymmetry parameter δ. c) Quality factor (Q) of each mode for various values of δ. These quality factors don't include material absorption or surface related mechanisms. The vertical axis is in log-scale.

appear centered at 56.5 MHz, separated by 1 MHz, at $\delta \approx -15$ nm. The simulations also show that the AS mode has consistently higher anchor loss limited Q's when compared to the S mode (fig. 4.2c). This difference appears because the S mode induces a larger displacement on the supporting beams, due to the two paddles' in-phase motion, coupling energy from the paddles to the pedestal and leading to a higher loss rate. On the other hand, the AS mode, due to the anti-phase paddle motion, drastically reduces the displacement at the anchor points, minimizing dissipation to the substrate when the two radiated mechanical waves are balanced. Moreover, we observe a rapid increase of this effect when the paddles are more symmetric ($\delta \approx 0$), indicating that it is possible to eliminate anchor losses simply by balancing the paddles. Note however that the point of minimum dissipation of the AS mode happens with $\delta \approx -15$ nm, due to geometry asymmetry of the single-sided pedestal supporting the beams.

A perfectly matched layer (PML) [97] is used to obtain dissipation due to mechanical energy radiation to the substrate (anchor loss). Similarly to the conformal transformation typically used in electromagnetic problems to solve curved regions [98], the PML is a transformation that maps the imaginary component of the material properties (associated with energy absorption) into the space variables, creating a perfectly absorbing region in the computational domain. But more than that, it does so in such a manner that the transition from standard to absorbing region is continuous, minimizing reflection in the interface and granting reliability on the resulting complex eigenfrequencies.

Nevertheless, because FEM divides the computational domain in a discrete mesh whose nodes are the points where the problem is solved, the PML has to be fine tuned so that the variation from one node to the other is smooth enough, minimizing reflections inside the PML itself, what could cause the return of energy from the absorbing region back to the standard domains, reducing the effective damping rate calculated. To account for that we performed a

series of simulations, changing the PML parameters until minimum quality factor was achieved for the S mode.

In the simulations shown here, the PML region was placed bellow the structure presented in figure 4.2a, although not shown. Also, it is important to note that this simulation only predicts losses due to radiation to the substrate, with bulk and surface material mechanisms left out. Figure 4.3 shows the expected behavior when some material damping rate, larger than the maximum radiation damping rate, is added to the results of the FEM simulations. Notice the smooth dependence close to $\delta = -15\ nm$, which is the result of almost constant Q-factors even for tens of nanometers variation in δ. This is a great contrast if compared to the bare anchor loss simulations, where any minimal variation in δ causes great changes in Q.

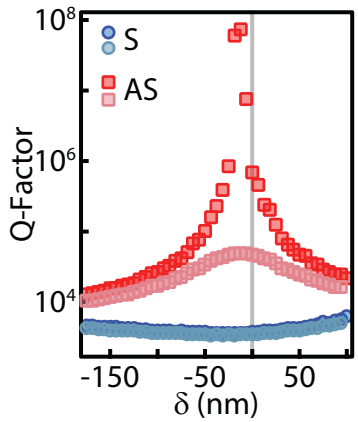

Figure 4.3: **FEM calculated mechanical Q with material loss contribution.** Representation of the expected asymmetry dependence of mechanical Q with material related losses contribution. The vertical axis is in log-scale.

This suppression of anchor loss through wave interference is not new in literature, being known since at least the invention of the tuning fork resonator, and is widely used by the micro-electro-mechanical systems (MEMS) community [99, 100]. But only recently it has been used to increase the performance of optomechanical devices by reducing mechanical dissipation [5, 38, 45].

4.3. Analytical model

A mass-spring lumped coupled oscillators model can be used to explain the tuning fork effect that suppresses anchor loss in the devices. The model consists of two mass-spring oscillators (m_1 and m_2 in fig. 4.4), which represent the two paddles, coupled to a third mass-spring oscillator (m_b in fig. 4.4), which represents the pedestal (or base) of the devices. Besides the indirect coupling of oscillators 1 and 2 through oscillator b, a direct coupling between oscillators 1 and 2 is also included. This direct coupling is necessary for the model to properly describe both losses and eigenfrequencies.

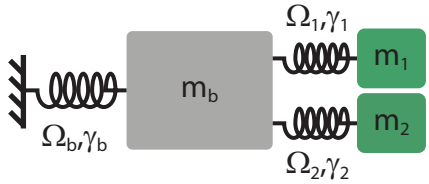

Figure 4.4: **Mass-spring coupled lumped oscillators schematics.** The masses and springs represent the paddles (1, 2) and the pedestal or base (b).

This system is represented by the following system of equations:

$$\begin{aligned} \frac{dx_1}{dt} &= \mathrm{i}\Omega_{m,1}\, x_1 + \mathrm{i}\frac{\beta_{1b}}{2}\, x_b + \mathrm{i}\frac{\beta_{12}}{2}\, x_2 \\ \frac{dx_2}{dt} &= \mathrm{i}\Omega_{m,2}\, x_2 + \mathrm{i}\frac{\beta_{2b}}{2}\, x_b + \mathrm{i}\frac{\beta_{21}}{2}\, x_2 \quad , \\ \frac{dx_b}{dt} &= \mathrm{i}\Omega_{m,b}\, x_b + \mathrm{i}\frac{\beta_{b1}}{2}\, x_1 + \mathrm{i}\frac{\beta_{b2}}{2}\, x_2 \end{aligned} \tag{4.1}$$

where the frequencies $\Omega_{m,i} = \Omega_{m,i} + \mathrm{i}\gamma_{m,i}$ are allowed to be complex, $\beta_{12} = \beta_{21}$ are the couplings between resonators 1 and 2 and $\beta_{1b} = \beta_{b1} = \beta_{2b} = \beta_{b2}$ are the couplings of oscillators 1 and 2 with 3, t is the time variable and x_i are the amplitudes of motion of the oscillators.

This model takes into account losses due to radiation to the substrate, given by a combination of $\gamma_{m,b}$ and β_{ib}, and intrinsic channels, given by $\gamma_{m,i}$. The frequencies of oscillators 1 and 2 (paddles) are estimated as those of doubly clamped silicon beams [30, 36], given by

$$\Omega = \left(\frac{k}{L}\right)^2 \sqrt{\frac{Y\, w^2}{12\, \rho}} \tag{4.2}$$

where L is the beam length (4 µm), w is its width in the direction of motion (200 nm), Y is silicon Young' modulus and $k = 4.73$ is a constant obtained from the equation of motion of a doubly clamped beam, considering the first mode [30, 36]. The density of the material (ρ) is modified to account for the extra mass of the paddles, without any change to the elastic properties. The expression for the modified density is given by

$$\rho = \frac{\rho_{Si}\left(V_{str} + V_{pad}\right)}{V_{str}}, \tag{4.3}$$

where ρ_{Si} is the density of silicon, V_{str} is the volume of the string and V_{pad} is the volume of the paddle, which may depend on the parameter δ, allowing changes to the mass of one of the oscillators. This still results in a minor (less then 2 %) deviation between the model's eigenfrequencies and the experimental ones, which is corrected with a scaling factor. The frequency of oscillator b is estimated to be 76 MHz from FEM simulations of the device without the paddles and nanostrings.

Solving the system of equations 4.1 results in a set of three complex coupled mode

eigenfrequencies, two for the symmetric (S) and anti-symmetric (AS) combinations of modes of the oscillators 1 and 2, and a third for the pedestal. By varying the mass of one of them (e.g. m_2) the expected avoided crossing of the coupled mode resonant frequencies and the shape of the damping rate observed in the FEM simulations is reproduced (fig. 4.5). The eigenfrequency and Q related to the base mode is not shown in figure 4.5 because its frequency is much higher than the graph top limit. Note that the example of solutions shown in figure 4.5 have maximum AS-mode Q when $m_1 = m_2$, which is not the case for the FEM simulations and, as will be shown later in this chapter, neither for the experimental data. This is easily accounted for by making $m_1 \to m_1 + \delta m$, which displaces the peak in Q to $m_1 - m_2 - = \delta m$.

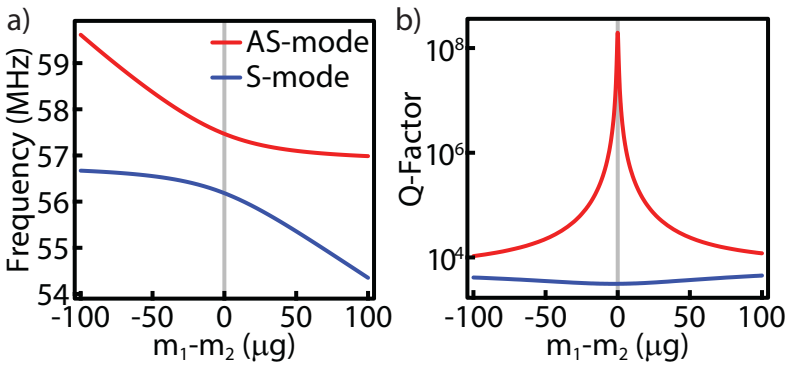

Figure 4.5: **Frequency and Q-factor obtained from the lumped model.** a) Frequency of the S (blue) and AS (red) modes of masses 1 and 2, as a function of the difference between masses 1 and 2. The frequency related to the mass b is not shown because it is over the top limit of the graph, at 76 MHz. b) Q-factor of the modes in (a) versus the difference between masses 1 and 2.

4.4. Thermoelastic damping and the Akhiezer effect

One of the most common material damping mechanism in silicon micromechanical resonator is thermoelastic damping [30, 101]. The thermoelastic effect is the process of temperature change of the material due to deformation, which means it is related to the coefficient of thermal expansion of the material. In micromechanical systems the modes of oscillation typically produce regions with compression and distension and, through the thermoelastic effect, these regions will have different temperatures (fig. 4.6), creating a temperature gradient that in turn creates heat flow. Because heat flow is a diffusive process this can lead to irreversible energy loss from the mechanical system, causing the so-called thermoelastic damping (TED).

As pointed out by Zener in his work [102, 103], if the motion is slow enough such that the material is always in thermal equilibrium with its environment (isothermal regime), or if it is so quick that heat doesn't have time to flow at all before another cycle of mechanical oscillation begins (adiabatic regime), then almost no energy is lost by this process. However there is a condition in between these two that can maximize TED, i.e., when most of the thermal

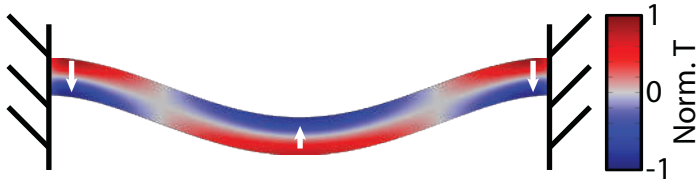

Figure 4.6: **FEM simulation of thermoelastic effect in a doubly clamped beam.** The arrows indicate heat flow between regions heated and cooled by the mechanical motion. Displacement exaggerated for clarity.

energy can flow from heated to cooled regions in each cycle. This relation between time-scales of mechanical and thermal processes is usually characterized by the product $\Omega_m \tau_{th}$, where Ω_m is the mechanical angular frequency and τ_{th} the thermal lifetime of the structure. Hence, when $\Omega_m \tau_{th} \ll 1$ the system is in the isothermal regime, while for $\Omega_m \tau_{th} \gg 1$ it is in the adiabatic regime.

To assess the role of TED in the devices presented in this thesis, we performed FEM simulations of this effect. A custom weak form was implemented and the validity of the FEM model was verified by comparing the numerical solution of a doubly clamped beam to the analytical model presented by Roukes and Lifshitz[101]. Figure 4.7a presents the results of this comparison, which shows great agreement between analytical and numerical models. To do this comparison the Young's modulus of the material was artificially varied in both cases.

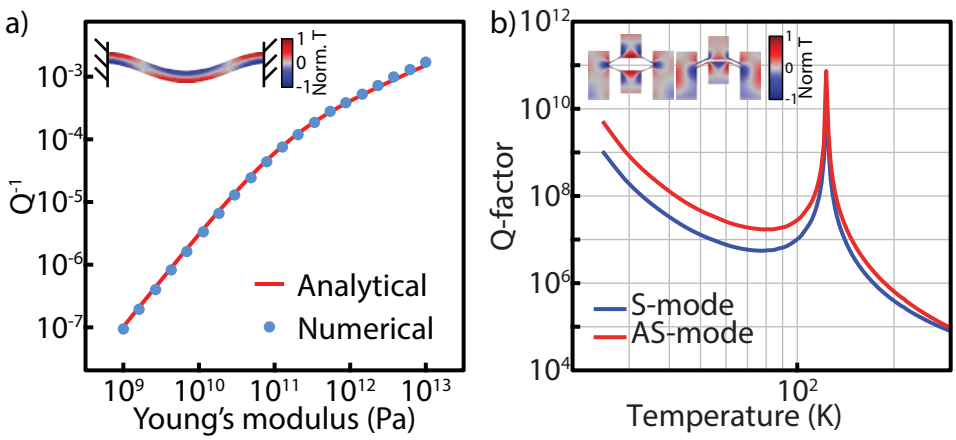

Figure 4.7: **FEM simulation of TED limited Q-factor.** a) Comparison of numeric and analytical models of TED on a doubly clamped beam. Inset shows the side-view of numerical thermal distribution. b) Numerical solution of temperature dependent TED limited Q for the S and AS modes of the paddles. Inset shows the top-view of numerical thermal distribution.

The FEM was then applied to the coupled paddles device, using temperature dependent material properties for temperatures varying from 300 K down to 25 K (see appendix G). The results for TED limited Q's are shown in figure 4.7b, where the minimum Q is 80k, at room temperature, and it increases to almost 10^{10} at 25 K. The peak around 125 K is due to the coefficient of thermal expansion of silicon going to zero at this temperature. In section 4.7 it will be shown that, in vacuum, the measured mechanical Q-factors are always much smaller

than the values obtained in this simulation, at all temperatures. This discrepancy indicates that, when anchor loss is suppressed, the tested devices are not limited by TED, but other mechanisms. This is easily understood from the $\Omega_m \tau_{th}$ relation for these devices, which is in the order of a few hundreds as the typical thermal lifetime is of a few microseconds and the mechanical mode of interest is in the tens of MHz (hundreds of rad/s) scale, leaving the system well in the adiabatic regime.

Another effect that is known to cause mechanical dissipation in silicon micromechanical resonators is the Akhiezer effect (AKE) [104]. This effect can be understood as follows (fig. 4.8): because the sample is always at a finite temperature it has natural thermal vibrational modes of its crystalline structure excited, with these thermal vibrations following a given dispersion relation [105, 106]; the mechanical motion of a given mode of interest locally distorts the crystalline lattice of the material, locally changing the dispersion of the thermal vibrations, which takes the thermal vibrations out of thermal equilibrium; finally, the system can thermalize to the new dispersion, which irreversibly removes energy from the mechanical mode.

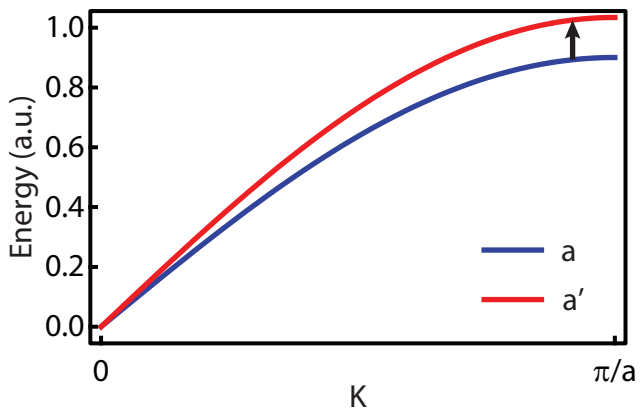

Figure 4.8: **Schematics of acoustic dispersion modification.** Mechanical motion locally distorts the material lattice ($a \rightarrow a'$), which in turn leads to a modification on the acoustic waves dispersion, taking the vibrations out of thermal equilibrium.

Again, this process has two limits, one isothermal, when the mechanical motion is so slow that the thermal vibrations are always in equilibrium, and one adiabatic, when the mode is so fast that the thermal vibrations never have time to recover equilibrium. This means that this effect can also be represented by a model similar to that Zener derived for the thermoelastic effect, but in this case the material property that maps the energy transfer from the mechanical motion to the thermal system is the so-called Grüneisen parameter. This parameter is defined as $\gamma = -(\partial \ln(\Omega)/\partial V)T$, i.e., it relates the change of the natural frequency of the crystalline modes (Ω) to the local change in volume (V) at constant temperature (T). It is important to note that this parameter is rigorously a tensor, with different components related to different polarizations and directions of propagation of the thermal vibrations, typically referenced to the crystalline planes. However, for the estimate of losses due to the AKE, it is usually substituted by an average constant value [107, 108].

The characteristic product that determines the regime the system is operating is

$\Omega_m \tau_{ph}$, where τ_{ph} is the thermal phonons (or vibrations) lifetime. Another common nomenclature found in literature is that for $\Omega_m \tau_{ph} \ll 1$ the system is said to be in the Akhiezer regime, while for $\Omega_m \tau_{ph} \gg 1$ it is said to be in the Landau-Rumer regime. Using the typical thermal phonons lifetime [109], it is easy to determine that the paddles devices of this thesis are in the Akhiezer regime, as $\Omega_m \tau_{ph} \approx 0.3$. Even being in this isothermal-like regime, it is known that this effect can still cause significant energy dissipation [110].

This effect is typically treated as a local process, not involving energy flux between different regions of the device, hence any dependency on the mechanical mode's shape is neglected. Then we look only for analytical models to try to estimate the role of this phenomenon in the coupled paddles devices. There are several works in the literature that derive analytical expressions for the AKE [107, 110–112]. We used the well accepted [43, 110] expression derived by Woodruff and Ehrenreich [107], that in the Akhiezer regime reduces to

$$\gamma_{m,\mathrm{AKE}} = \frac{\gamma^2 c_p T}{3\rho v_D^2}\, \Omega_m^2 \tau_{ph}, \tag{4.4}$$

where v_D is the Debye average speed of vibrations propagating in the $[110]$ direction [113], τ_{ph} is the phonon life-time, for which the values for thermal phonons interacting with acoustic phonons propagating in the $[110]$ direction with polarization in the $[1\bar{1}0]$ direction are used [109, 113], γ is the Grüneisen parameter, c_p is the specific heat, ρ is the material density and T is the equilibrium temperature. Note that these values are not all available for temperatures below 80 K, hence we have to extrapolate the values for sound speed and phonon life-time to obtain estimates below this temperature. The crystalline planes chosen are based on the relation of the direction of motion of the modes studied.

Usually, thermal conductivity is substituted for the thermal phonons lifetime using the relation $k = c_p v_D^2 \tau_{ph}/3$. But, as discussed by Ilisavskii [109], the thermal phonons lifetime in silicon is very dependent on the polarization and direction of propagation of the mechanical motion that affects their dispersion, which makes it difficult to perform this substitution. Hence we chose not to use thermal conductivity when evaluating the role of AKE in our devices.

Also, the literature is very divergent on the values used for the Grüneisen parameter, being the most common value at room temperature $\gamma = 1.5$ [30, 108]. However, we couldn't find reliable sources with this parameter's dependence on temperature that agreed with this value at 300 K. Hence an upper boundary for the AKE Q limit was defined based on the values given by Philip and Breazeale [114], which state $\gamma(T = 300\ K) = 0.45$, and a lower boundary shifting all values from reference 114 such that $\gamma(T = 300\ K) = 1.5$. It will be shown in section 4.7 that this model's lower boundary renders a Q-limit that is only a factor two larger than the best experimental results, indicating that this effect can indeed have an important role in the mechanical energy dissipation of the devices presented. This is expected because with $\Omega_m \tau_{ph} \approx 0.3$ the system is in the isothermal (Akhiezer) regime, but not too far from the maximum attenuation condition ($\Omega_m \tau_{ph} = 1$).

4.5. Optical mode polarization and radial order

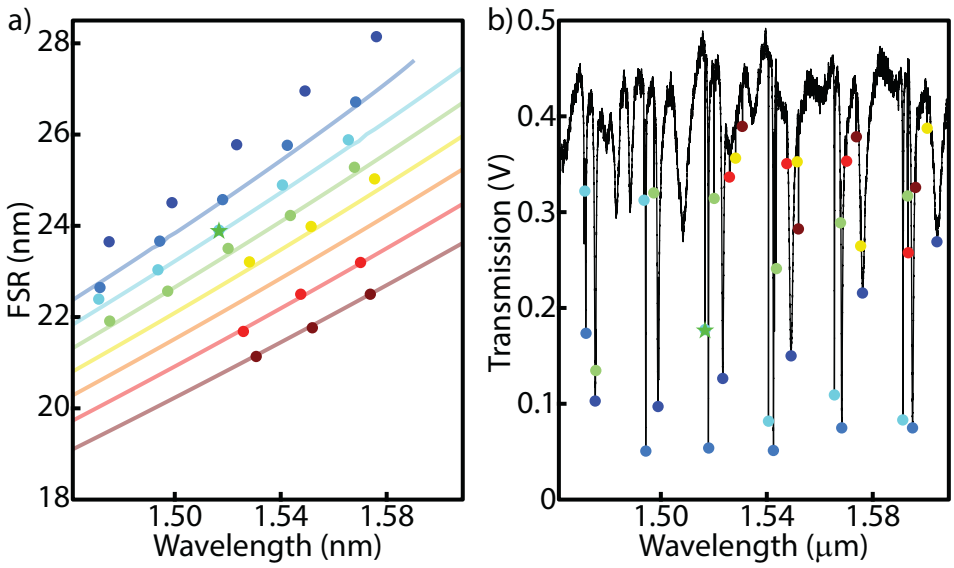

Figure 4.9: **Determination of optical mode polarization and radial order.** a) Dispersion of experimental (dots) FEM calculated (solid lines) TE-like optical modes. Radial order increases from bottom to top, 1st to 7th. b) Experimental optical spectra for the TE-like polarization. Circles on (a) and (b) are related by color. The green star marks the optical mode used to probe the mechanical resonator.

The polarization (transverse electric – TE or transverse magnetic – TM) and radial order of the optical modes are determined by comparing FEM numerical solutions of the disk's modes to the measured spectra. This is done by solving for the modes' azimuthal numbers (m) for various wavelength values (λ_0) and calculating their separation (free-spectral-range or FSR). This results in the curves shown as solid lines in figure 4.9a, where the radial order increases from bottom to top. This curves are related to the dispersion curve as the FSR is proportional to the group velocity associated with each mode. Then the experimental families of modes are determined on the experimental transmission data, their FSR is calculated and ploted (FSR vs. λ_0) over the numerical solution; these are shown as dots in figure 4.9. The optical mode used to probe the mechanical resonators is marked with a green star.

The wavelength axis is calibrated following the procedure presented in section 3.1. This results in excellent agreement with the numerically calculated dispersion of a 4.9 μm radius silicon disk, which is only 2% smaller than the nominal disk that is below any fabrication precision. Repeating the procedure with TM-like numerical and experimental data (not shown) also result in very good agreement. The fact that there are families of modes with smaller FSR than the one used to probe the mechanical resonator (green star) demonstrates that we used a high radial order mode to perform the measurements; in this case the mode is likely a 6th radial order TE-like mode.

4.6. Dependence of g_0 on the optical mode radial order

In order to readout the motion of the paddles, the front paddle is designed to be 200 nm away from a 5 µm radius disk optical cavity (fig. 4.1) supporting whispering gallery modes (WGM) [28]. Optical readout is possible because the motion of the paddles modulates the frequencies of the optical modes through evanescent field perturbation.

The figure of merit of this interaction is the vacuum optomechanical coupling rate [31], $g_0 = (\partial\omega/\partial x)x_{\mathrm{zpf}}$, which measures the amount of optical frequency shift caused by a displacement with a quantum-mechanical zero-point fluctuation amplitude ($x_{\mathrm{zpf}} = \sqrt{\hbar/2m_{\mathrm{eff}}\Omega_m}$, where $\hbar$ is the reduced Planck's constant and m_{eff} and Ω_m are the mechanical effective mass and frequency, respectively). Although there are usually two main contributions to the optical resonance shift, namely boundary motion [22] and photo-elastic effect [23], only the former is considered because the mechanical modes studied in this thesis induce negligible strain throughout the material volume.

The moving boundary optomechanical coupling rate (g_0) can be estimated through perturbation theory by [22]

$$g_0 = x_{zpf}\,\frac{\omega_0}{2}\frac{\int_S |\mathbf{U}_n|\left(\Delta\varepsilon|\mathbf{E}_t|^2 + \Delta\varepsilon^{-1}|\mathbf{D}_n|^2\right)dA}{\int_V \varepsilon_0\, n^2\, |\mathbf{E}|^2 dV}, \tag{4.5}$$

where $x_{zpf} = \sqrt{\hbar/(2m_{eff}\Omega_m)}$ is the quantum zero-point fluctuation of a mechanical mode with effective mass m_{eff} and angular frequency Ω_m, ω_0 is the optical unperturbed resonance frequency, $\mathbf{U}_n$ is the normalized mechanical displacement perpendicular to the surface S, $\Delta\varepsilon = \varepsilon_0(n_{in}^2 - n_{out}^2)$ is the difference of electrical permitivity inside and outside the material and $\Delta\varepsilon^{-1} = \varepsilon_0^{-1}(n_{in}^{-2} - n_{out}^{-2})$, $\mathbf{E}_t$ is the electric field tangent to the surface, $\mathbf{D}_n$ is the electric displacement normal to the surface and $\mathbf{E}$ is the total electric field distributed in the volume V.

Also, the optical effective mode volume can be defined as [115]

$$V_{eff} = \frac{\int_V \varepsilon_0 n^2 |\mathbf{E}|^2 dV}{\varepsilon_0 n_{max}^2 |\mathbf{E}|_{max}^2}, \tag{4.6}$$

where $|\mathbf{E}|_{max}^2$ is the maximum field intensity and n_{max} is the refractive index of the medium at the point where the field is maximum.

Then equation 4.5 can be written as

$$\frac{g_0}{x_{zpf}} = \frac{\omega_0\,\Gamma_{OM}}{2\varepsilon_0 n_{max}^2 V_{eff}}, \tag{4.7}$$

where the optomechanical moving boundary overlap integral is defined as

$$\Gamma_{OM} = \int_S |\mathbf{U}_n|\left(\Delta\varepsilon|\tilde{\mathbf{E}}_t|^2 + \Delta\varepsilon^{-1}|\tilde{\mathbf{D}}_n|^2\right)dA, \tag{4.8}$$

with $|\tilde{\mathbf{E}}_t|^2 = |\mathbf{E}_t|^2/|\mathbf{E}|^2_{max}$ and $|\tilde{\mathbf{D}}_n|^2 = |\mathbf{D}_n|^2/|\mathbf{E}|^2_{max}$.

For the in-plane modes presented in section 4.2, g_0 is estimated using equation 4.5 for various radial orders of the optical TE modes, which were calculated using FEM, using the axial symmetry of the optical cavity to reduce the problem from 3D to 2D. More details on the geometry used to estimate g_0 can be found on appendix D. To obtain the radial order dependence, the optical modes' azimuthal number (m) is calculated for a fixed wavelength. This invariably returns non-integer m values, which are not physically correct, as the periodic boundary condition imposes integer numbers for the azimuthal index [18]. Nevertheless, this doesn't invalidate this analysis because, in this case, we are interested in determining what difference in g_0 should be expected if a given mode was of first or 8th radial order. The calculated g_0 values, for the perfectly balanced device, range from tens to several hundred Hz, as shown in figure 4.10, increasing for higher radial order optical modes.

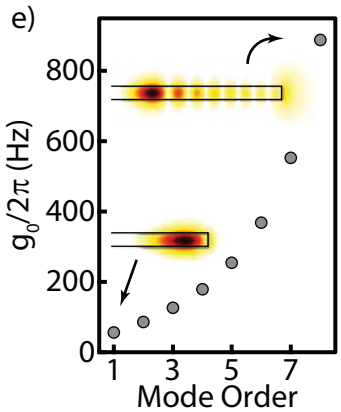

Figure 4.10: **Dependence of g_0 with the optical mode radial order.** Insets show the distribution of the radial component of the electric field for the first (bottom) and 8th (top) radial order. The wavelength is artificially the same for all points and is equal to 1520 nm.

This behavior is counter-intuitive for those used to look only to the confined field in WGM cavities, as the higher optical intensity region is located further from the disk's border for higher radial order modes. But it is easily explained once the decay characteristics of the evanescent field is evaluated.

In equation 4.7, only Γ_{OM} and V_{eff} depend on the field distribution, hence they must be the terms that determine the dependence of g_0 on the modes' order. Using FEM simulations V_{eff} and Γ_{OM} are computed for TE modes with radial orders varying from 1 up to 8. Figure 4.11a shows the calculated values of Γ_{OM} and V_{eff} normalized by the values obtained for the first order mode. While V_{eff} changes by at most 20%, Γ_{OM} increases greatly, almost 16 times for the 8th order mode. Hence the g_0 dependence presented on figure 4.10.

The behavior of Γ_{OM} is explained by the evanescent field of different radial order modes as a function of the distance from the disk border (fig. 4.11b). Although the field intensity for each order may vary at the edge of the disk, at the closest paddle's position (dashed line in fig. 4.11b) the decay rate difference results in higher field intensities for higher order modes.

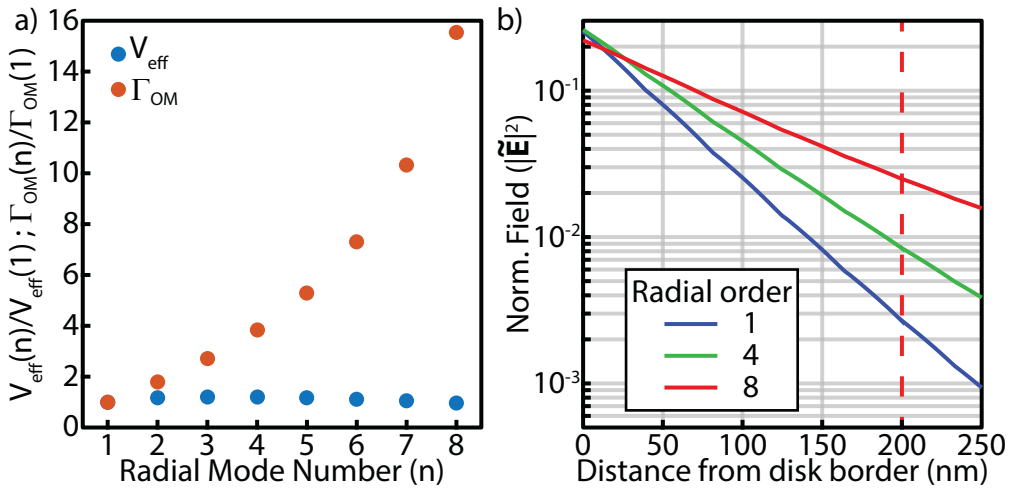

Figure 4.11: **g_0 field dependent components and evanescent field deay profile.** a) Effective mode volume (V_{eff}) and Γ_{OM}, calculated at 200 nm away from the disk's border, for different radial order modes, normalized by the value for the first order mode. b) FEM calculated evanescent field profile, for three different radial order modes, outside of a 5 µm radius and 220 nm thick Silicon disk optical cavity. The field in (b) is normalized by the maximum field value for each mode, which occurs inside of the cavity; the dashed vertical line indicates the position of the paddle closest to the disk.

Note that the surface integral in Γ_{OM} should be calculated on all the surfaces of the two paddles but, because of the characteristic field decay length, only the surface closest to the disk contributes significantly to g_0. This allows for determining the better balanced device in the samples by measuring g_0. That is because only for this device the amount of amplitude of motion of the front paddle is approximately the same for both S and AS modes, resulting in similar Γ_{OM} and, consequently, similar g_0.

Nonetheless, one may ask why the devices are measured with the mode indicated in figure 4.9 if there are at least two other modes with higher radial order, hence higher g_0. The answer is because the signal we obtain doesn't depend only on g_0, but also on the optical damping rate. This can be easily observed taking equation 3.1 evaluated at $\Delta = 0$ and with the transduction function for the homodyne detection scheme of equation 3.3, which results in

$$S_{II}(\Omega) = F(\Omega)\, S_{xx}(\Omega)\, P_{in} \left(\frac{8\, g_0\, \kappa_e\, \Omega}{x_{zpf}\, \kappa^2} \right)^2 . \tag{4.9}$$

Then, because the higher the optical mode radial order the lower the quality factor, as easily observed on the optical spectra of the cavities, we chose that particular mode for it was the one that yielded the best spectral density signal for our samples.

4.7. Experimental results

The devices are all measured following the procedure detailed in chapter 3, section 3.3, using the homodyne scheme. Measurement of g_0 using the phase-modulation signal as reference yields an optomechanical coupling rate of 450 Hz, which is low if compared to other optomechanical devices in literature that present coupling rates ranging from kHz [12, 21] up to MHz [23]. But this g_0 is expected for NFO devices and is highly dependent on the distance between paddles and disk [116]. Also this value agrees very well with those from numerical simulations (see sec. 4.6). The mechanical modes are identified by directly comparing measured frequencies with those from FEM simulations, which agree within a 2% margin. All measurements are performed with the optical cavity undercoupled to the taper ($\kappa_e < \kappa_i$), even though the experiments are performed with the taper touching the optical cavity. This is due to the fact that the taper is a silica (n=1.45) waveguide with air cladding, while the optical cavity is a silicon (n=3.45) resonator with air cladding. That makes the propagating constants of the confined light in each structure very different and, consequently, reduces the cavity-taper coupling rate.

The room temperature (RT) mechanical quality factors (Q) are obtained from the measured power spectral density (PSD) of the two in-plane mechanical modes while the sample is in a vacuum chamber (10^{-5} mbar). Using the homodyne detection scheme [78] the samples are probed with the laser tuned to the center of the optical resonance, thus avoiding any optomechanical feedback that could affect the mechanical quality factor [31, 75, 76]. Figure 4.12(a,b) shows the measured calibrated displacement spectral density, as well as Lorentzians fitted to the data, for the device with $\delta = -50$ nm, which has the highest AS mode quality factor, $Q_{\mathrm{AS}}^{\mathrm{RT}} = (7.61 \pm 0.07)$k, and $Q_{\mathrm{S}}^{\mathrm{RT}} = (4.53 \pm 0.04)$k for the S mode. The mechanical resonance frequencies of these coupled modes are around $f \approx 56$ MHz with a frequency splitting of $\Delta f_m = 940$ kHz, in good agreement with the FEM simulations.

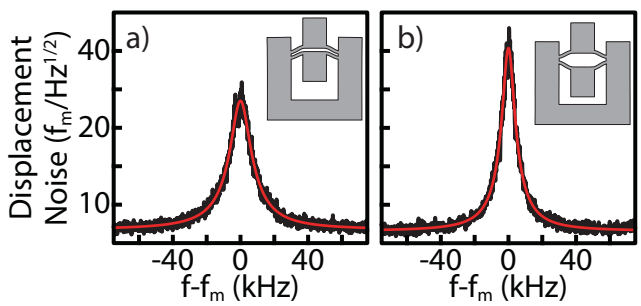

Figure 4.12: **Displacement spectral density at room temperature.** S (a) and AS (b) modes' calibrated displacement spectral density at room temperature. Data is shown in black and fitted Lorentzians in red. $f_m \approx 56$ MHz and splitting of 940 kHz. Data of device with $\delta = -50$ nm.

In chapter 1 it was mentioned that one important figure of merit of oscillators is the Qf-product, which gives a frequency independent feature of the system, when it is limited by

material losses, facilitating the comparison between different devices. For this particular device this product yields $Qf = 4 \times 10^{11}$ Hz, which is no record for silicon based micromechanical oscillators [108], but probably the highest for NFO devices fabricated in photonics compatible SOI platforms (silicon thickness between 100 nm and 400 nm) [117, 118], operating at room temperature and on the 50 MHz frequency scale.

The fact that this device, with $\delta = -50$ nm, is the one with best anchor loss suppression is determined by measuring the frequency, Q and optomechanical coupling rate for devices with varying balance between paddles, as shown in figure 4.13. Here we show the frequency difference between S and AS modes, because the absolute frequencies present a relatively large fluctuation due to fabrication variations [119], making it harder to identify the avoided crossing and the better balanced device. There is still a fluctuation in the frequency difference around $\delta = 0$ whose origin is unknown, as no significant variations of the geometry were found in SEM images.

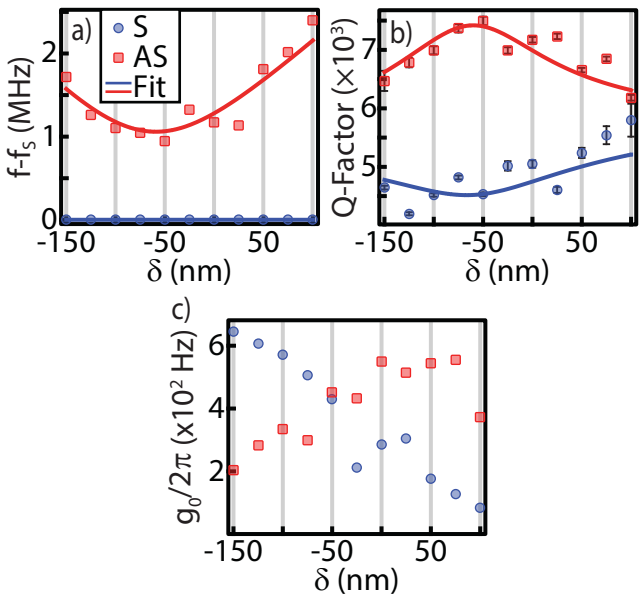

Figure 4.13: **Dependency of frequency, Q and g_0 on δ at room temperature.** a) Dependence of frequency difference between S and AS modes on δ. Solid lines are the analytical model with parameters fitted to the data. b) Mechanical Q-factor dependency with δ for S and AS modes. Solid lines are the analytical model with parameters fitted to the data. c) Dependence of g_0 on δ for the S and AS modes.

This device not only has the smallest frequency difference and highest AS Q, but it also has S and AS modes with almost identical measured optomechanical coupling rates. Due to the similar effective masses and frequencies of S and AS modes, this further indicates that the optical overlap of the front paddle displacement is also balanced, which results in similar G_{OM} and, consequently, similar g_0 for both modes. Experimentally, the best balance of mechanical waves radiation occurs for a δ-value different from the simulated results, which can be explained by deviations in the devices geometries, such as the buried oxide pedestal shape and the rounded corners in the clamping regions of the nanostrings. The analytical model (sec. 4.3)

is fitted to the data, resulting in the following parameters and their respective fitting standard errors: (β_{12}, β_{1b}, Q_b, $Q_{1,2}$) = (0.65 ± 0.06 MHz, 4.0 ± 0.4 MHz, 323 ± 9, 7380 ± 60).

Comparison of the S and AS modes' quality factors, for devices with different δ (fig. 4.13b), shows consistently higher quality factors for the AS modes, suggesting an important contribution from anchor loss for the unbalanced devices. Nevertheless, its modest two-fold improvement compared to the S mode — even for the best resonator — indicates that other loss mechanisms are also playing an important role in the overall dissipation.

Some of these mechanisms, such as thermo-elastic damping and Akhiezer effect, depend on material properties that typically vary with temperature. Then, to suppress temperature dependent mechanisms and intensify the role of the radiation suppression scheme in the overall mechanical losses, the sample is inserted in a cold-finger cryostat to cool it down to 22 K. At these low temperatures (LT), a high enhancement of 385% for the AS mode quality factor, reaching $Q_{\mathrm{AS}}^{\mathrm{LT}} = (37.0 \pm 0.6)$k (fig. 4.14b) is observed, while the S mode increases only by 80%, up to $Q_{\mathrm{S}}^{\mathrm{LT}} = (8.2 \pm 0.1)$k (fig. 4.14a), for the device with $\delta = -50$ nm.

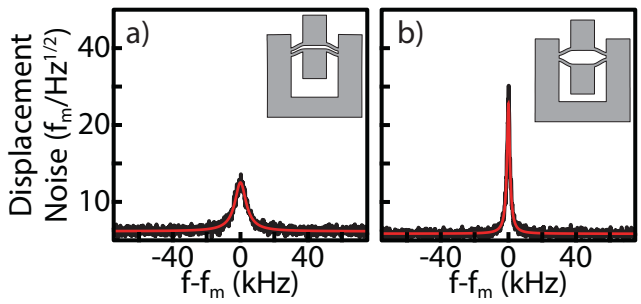

Figure 4.14: **Displacement spectral density at cryogenic temperature.** S (a) and AS (b) modes' calibrated displacement spectral density at cryogenic temperature. Data in black and fitted Lorentzians in red. $f_m \approx 56$ MHz with splitting of 960 kHz. Data of device with $\delta = -50$ nm.

These Q-enhancements are accompanied by a small (0.7%) increase in mechanical frequencies due to an expected material stiffening at LT, resulting in a Qf-product of 2×10^{12} Hz. Such a high contrast between the S and AS modes' quality factors at LT clearly indicates the efficiency of the destructive interference scheme. Note that the LT limit for the Q of the S mode is approximately two times greater than the predicted by the FEM simulations shown in figure 4.2c, which can be explained by differences on the pedestal shape that affect how much mechanical energy can leak to the substrate. Nonetheless, the calculated anchor loss limited Q is much higher for the AS mode, an indication that the devices may have reached some kind of material or surface related limit at 22 K.

I further investigate the nature of the low temperature Q-limit by increasing the cryostat base temperature from 22 K up to 200 K, while monitoring the mechanical quality factors (fig. 4.15). The measured Q temperature dependence reveals a capped behavior below $\sim$ 100 K and a power-law reduction up to 200 K; above 200 K there is an apparent increase in both S and AS quality factors. The power law and the limit bellow 100 K are assessed by

considering two common material related loss channels in silicon devices, the thermoelastic damping (TED) [101] and the Akhiezer effect (AKE) [104, 107]. The expected TED-limit Q's temperature dependence, based on FEM calculations, are shown in figure 4.15 as red and blue lines. As presented in section 4.4, the expected RT TED-limited Q values are close to 10^5, while the expected LT TED limits are well above the 10^8 level, without any decrease below the RT limit. Hence, TED cannot explain neither the LT, nor the temperature dependent, nor the RT Q limits. This is expected due to the large mismatch between the mechanical period and thermal lifetimes in these devices.

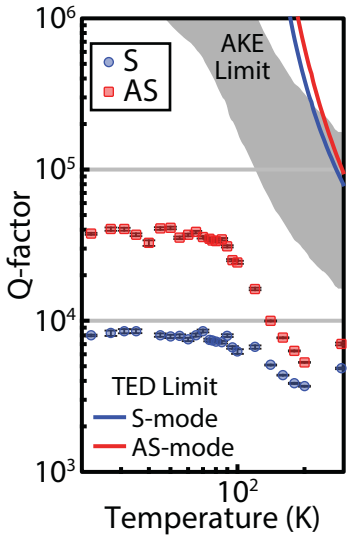

Figure 4.15: **Temperature dependence of mechanical Q-factor.** Dots mark the experimental data for the S and AS modes. Solid lines ar the TED limits for S and AS modes' Qs. The shaded area indicates the region bounded by the upper and lower AKE limits.

In order to verify the role of the Akhiezer effect (AKE) we considered the model by Woodruff and Ehrenreich [107] with temperature dependent material properties [113, 114, 120] (see sec. 4.4 and appendix G). As mentioned before, among the parameters involved in this model, the Grüneisen parameter (γ) has the largest range of reported values [108], resulting in an upper and a lower Q-limit due to the AKE, respectively. Therefore, to obtain temperature-dependent boundaries for the AKE damping, we used the measured γ temperature dependence [114] for the upper AKE Q-limit, whereas we rescaled these γ values such that at RT $\gamma^{RT} = 1.5$, resulting in the lower limit. The gray area on figure. 4.15 is bounded by these upper and lower limits, and the lower-limit is roughly within a factor 2 above the RT measured values. Comparison of the variation of Q with temperature suggests that this effect is the most likely material damping mechanism to affect our devices from room temperature down to 100 K. However, the mismatch between analytical model and experimental data also suggests that some other effect also has an important impact in the mechanical losses, at all temperatures.

The Q-limit observed at LT could be attributed to a residual asymmetry in the fabricated paddles. To investigate this possibility we measured the δ dependency of the quality factor of these modes in a second cool-down of the sample (fig. 4.16). Again the AS mode

presents consistently higher Q-factors and the fitted model results in the following parameters: (β_{12}, β_{13}, Q_b, $Q_{1,2}$) = (0.65 $\pm$ 0.06 MHz, 4.0 $\pm$ 0.4 MHz, 320 $\pm$ 20, 27900 $\pm$ 1300). The values for the coupling rates (β_{12} and β_{13}) are the same as the ones for the RT case because we fixed them at those values. This is justified by the very small change in frequency and splitting (0.7%) at LT.

Notice that Q_b changed by less than 1% from RT to LT, while $Q_{1,2}$ varied by a factor 4, indicating that the increase in Q and in its dependence with δ can be reasonably explained by a decrease in material related losses, without necessarily changing anchor losses. Also, the slowly varying AS mode Q-enhancement towards the higher symmetry region ($\delta \approx -50$ nm) suggests that the mechanical Q is not being limited by variations in the device geometry (see fig. 4.3 in sec. 4.2). Moreover, numerical simulations confirm that small (up to 5 %) variations on any of the device transverse dimensions would not quench the AS quality factors to the LT measured levels. Hence, we infer that the AS mode LT Q-factor is not being limited by failure of the destructive interference scheme.

However, note that the variation from $\delta = -25$ nm to $\delta = 25$ nm also increased, with the Q of device with $\delta = 25$ nm presenting larger enhancement than its neighbors. This indicates that this fluctuation might be caused due to variations on the geometry of these devices, which are changing how anchor loss affects each one of them, although the actual cause of this changes have not been determined. Nevertheless, this seems to be an effect confined to the devices with $\delta = -25$ nm and $\delta = 25$ nm, hence it should not invalidate the analysis presented previously on the limitation of the device with $\delta = -50$ nm.

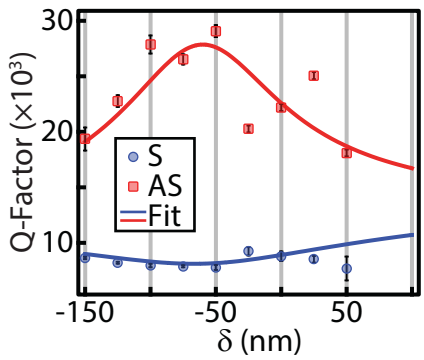

Figure 4.16: **Dependency of Q on δ at low temperature.** Mechanical Q-factor dependency with δ for S and AS modes at 22 K. Solid lines are the analytical model with parameters fitted to the data.

Another loss channel that could be considered to be limiting the performance of these devices is related to surface effects, which are known to be important damping mechanism in very thin (less than 1 μm thick) silicon devices [121–124]. An important hint about the role of surface dissipation is evident in the data presented so far. Note that the maximum Q in figure 4.16 is 35% smaller than the data shown in figure 4.15. In fact, the data presented in figure 4.15 was taken during the first cool-down of the sample, while the data in 4.16 was taken in the second cool down. In the meantime the sample was not removed from the vacuum

chamber, although the vacuum pump was turned off keeping the valves closed, what caused an increase in the chamber inner pressure, but not up to atmospheric pressure ($\approx$ 5 mbar). This suggests that some sort of surface modification could have occurred in the devices.

To assess the role of surface effects, we measured the impact of surface treatment – cleaning [57] and local laser annealing [125] – on the Q temperature dependence. These measurements were carried out from liquid nitrogen temperature (LNT, with the sample reaching $\approx$ 82K) up to room temperature. We chose to use liquid nitrogen (LN), instead of helium (LH), because of the time-scale of the experiment. Usually an 8h experiment takes approximately 60 L of LH to cool the sample and to keep the temperature stable. On the other hand, the same amount of LN can be used for 2 to 3 experimental processes. Moreover, although the Physics Institute of UNICAMP has a cryogenic workshop, where both LH and LN are continuously produced, the time-scale to obtain LH is of about one week, due to the liquefaction rate and demand, while LN can be obtained in a daily basis. The results of the surface treatment tests are summarized in figure 4.17, where the data of figure 4.15 is repeated in lighter colors for comparison, as well as the AKE and TED theoretical limits.

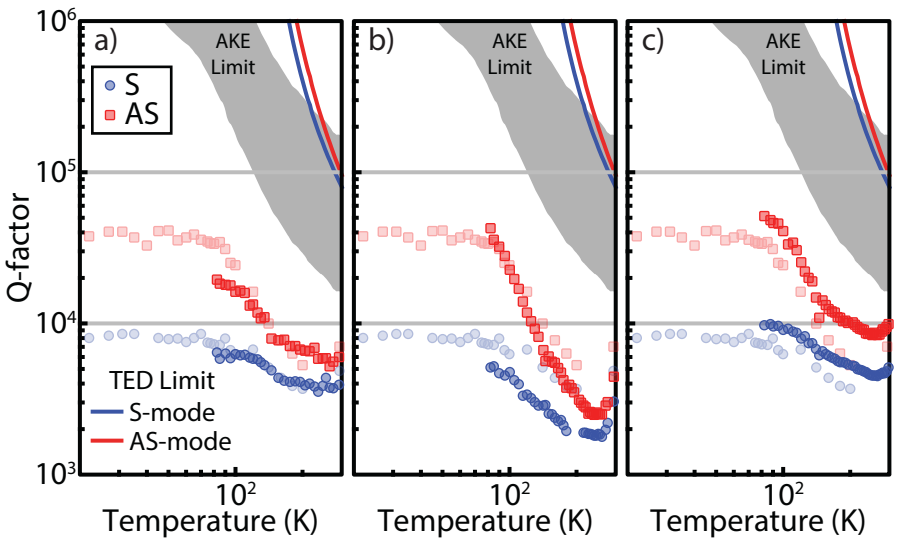

Figure 4.17: **Temperature dependence of Q-factor at different surface conditions.** a) After a few months stored in a box with N_2 rich atmosphere. b) After cleaning with piranha solution and HF dip. c) After in-situ laser annealing – device with $\delta = -75$ nm. The first cool down measurement is kept in every figure for comparison (lighter colors). Shaded area marks the Akhiezer limits and the blue and red lines the TED limits.

The description of each measurement in figure 4.17 is listed below:

Fig. 4.17a: First the sample is measured after being stored in a box with N_2 rich atmosphere for a few months after the measurements presented before (lighter colors). The modes of interest are probed at RT (293 K), at 82 K and while the temperature increases from 82 K up to RT. Observe that both S and AS modes had their RT Q degraded, indicating that changes on the device have occurred since it was last

measured. Also, the temperature dependence of both modes was very similar to the first cool down, but the AS mode saturated with a Q of 20k at 82 K, half of the maximum obtained in the first cool down and 70% of the second (fig. 4.16). Again, this is indicative that some structural changes might have occurred while the sample was stored.

Fig. 4.17b: After that, the sample was cleaned using piranha solution and a 30 seconds dip in a 1:10 solution of HF in water, and the measurements repeated. After cleaning, the sample remained in contact with air for about one hour before measurements. An overall reduction of the Q's at room temperature was observed, and the S mode presents lower Q factors for all temperatures. However the AS mode reached a Q = 45k at 82 K and it is hard to tell if it would saturate or continue rising if temperature continued decreasing. This is a 13.5% increase with respect to the value at 22 K in figure 4.15 and 45% if compared to the maximum value in figure 4.16.

Also, a minimum in Q for both modes around 220 K is clearly observed, which seems also to be present on the first cool down measures and is not easily observed due to lack of points around these temperatures. Similar minima have been observed in other structures[124, 126–130] and, although typically associated with dislocation relaxation[126] or surface related effects[124, 127], their actual origin still lack proper explanation and its detailed investigation lies beyond the scope of our work.

Fig. 4.17c: Finally, we performed in-situ laser annealing [125], while the sample was in vacuum at room temperature, and repeated the whole temperature dependent measurement process. The annealing is performed by focusing a continuous-wave green laser, with approximately 500 mW of power, on the sample. This is accomplished by launching the laser through the objective of a microscope, which is also used to image the samples. We note here that, although we could measure the device with $\delta = -50$ nm at RT, it was damaged in a second annealing attempt before the cool down. This prevented me from acquiring the temperature dependent data for this device. Nevertheless, the RT data presented an increase on Q's for this device, with the AS mode's reaching 10k, while the S mode was limited to 5.0k, close to the value measured on the first cool down (lighter colors in fig. 4.17).

Because the device with $\delta = -50$ nm was damaged, which was used in the dataset so far, and because we wanted to avoid changing the sample for these tests, we were forced to measure the temperature dependence for the second better balanced device at room temperature (δ=-75 nm). We annealed this new device at RT and repeated the cooling and heating process. Note that this device, although not as well balanced as the one with δ=-50 nm, reached a Q of 54k for the AS mode at 82 K, repeating the best result of the previous measurement (after cleaning), while

the S mode saturated at the 10k plateau. This is a 103% increase for the AS mode if compared to the values measured at 82 K in figure 4.17a. Also, the S mode maintained a Q value, at RT, very close to the obtained before the first cool down, but the AS mode reached a Q of 10k, indicating that even this device is not limited by anchor loss, at RT.

I note that, on these last measurements, the AS mode seems to saturate its LNT Q at about 54 K. However, this device is not the best balanced on this sample, hence it is not possible to determine if this limit is due to material/surface effects or failure of the anchor loss suppression scheme.

4.8. Conclusion

In summary, we have demonstrated the use of destructive interference of elastic waves as an effective approach to obtain high-Q mechanical resonators at the 50 MHz frequency scale. The data clearly shows that symmetric modes are highly susceptible to anchor loss, while the antisymmetric modes may be limited by other mechanisms, such as surface scattering and the Akhiezer effect. To further increase these devices' performance one should pay attention to the fabrication process, including surface treatment steps [125, 130, 131], reducing surface related dissipation and increasing the Q limit for the AS mode. We expect these devices to serve as platforms for studies of arrays of optically coupled mechanical resonators, as well as very sensitive force sensors.

The consistently higher Q_{AS}, obtained after the surface-treatment of the same sample (for the better balanced device, $\delta = -50$ nm), suggests that the AS mode quality factors were limited by surface related mechanisms. Although further investigation would be required to reduce surface-loss, the observed Q-enhancement after surface treatment suggests that the LT Q-limit is not due to failure of the destructive interference effect.

Chapter 5

Self-pulsing in Silicon Micro-cavities

One very common material used for developing optomechanical devices is silicon. Its use is encouraged by the fabrication process, which is very well established thanks to the development of the electronics industry in the late 21st century. Moreover, it increases the possibility of integrating optical, mechanical and electronic systems, all in the same platform. However, silicon is a material with relatively high non-linear optical properties, with two-photon absorption (TPA) as the main process limiting its usage for non-linear optics and also optomechanics. In optical micro-cavities, this process, associated with the thermo-optical effect (change of refractive index with temperature), can lead to what is called self-pulsing of the stored energy [48, 49, 132], a process that can affect the operation of optomechanical systems [50, 51].

In fact this phenomenon was observed in the NFO devices presented in the previous chapter, what inhibited tests with the devices set to optomechanical self-oscillations. On the other hand, self-pulsing became an object of interest, both to learn how to suppress it and because it can become an important asset in the development of integrated photonic platforms.

This chapter addresses self-pulsing in silicon optical micro-cavities, presenting the basic model and its results, as well as the experimental demonstration of this oscillations in an optical cavity. Also, it shows that this effect can couple between different optical cavities, which takes the problem to coupled optomechanical systems, but also paves the way for the study of the dynamics in coupled optical based oscillators.

5.1. Device presentation

The process to obtain the devices presented in this chapter is detailed in chapter 2. After wet etching and cleaning the samples, they are all characterized in room conditions (atmospheric pressure and approximately 293 K). Two systems were studied, one composed by a single cavity (fig. 5.1a,b) and another with two optically coupled cavities (fig. 5.1c,d). In both cases the cavities are 2 μm radius disks supporting whispering gallery modes with typical quality factors of 70k to 80k for modes with resonances close to 1470 nm. The two disks of the double cavity system are separated by 300 nm (measured at the smallest distance between disks).

The optical spectrum of the single cavity system (fig. 5.1b) presents a splitting due to coupling of counter-propagating modes [70] with coupling rate of 13.6 GHz. The double

cavity spectrum (fig. 5.1d) presents two kinds of splitting, a smaller one due to the coupling of counter-propagating modes and a larger one due to the coupling of the two cavities [96]. The double disks smaller coupling rate is of 6.3 GHz, while the larger coupling rate is 28.2 GHz. Although the smaller splitting is hard to control, because it depends on the roughness of the cavity surface, the larger splitting is easily tailorable by changing the distance between the two cavities, which is translated into a change in the coupling rate between their modes. These optical spectra are typically obtained with the input laser power set to less than 500 nW, as powers higher than that usually distort the peaks due to non-linear effects [133].

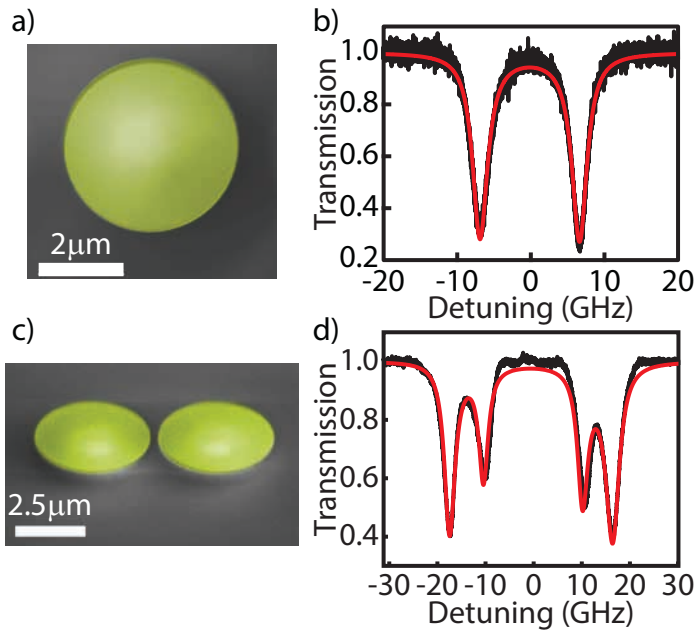

Figure 5.1: **SEM and optical spectra of the 2 μm radius optical cavities.** a) Top view scaning electron microscope (SEM) image (false-color) of a single 2 μm radius silicon optical micro-cavity. b) Optical spectrum of one resonance of the single disk of figure (a), showing the splitting due to coupling of counter-propagating modes (g_{cp}). Center wavelength is 1471.4 nm, with linewidths of 2.5 GHz ($Q = 81.6$k) and $g_{cp} = 2\pi \times 13.58$ GHz. c) Angled view SEM of a double cavity system. The cavities are nominally identical, with 2 μm radius and a minimum separation of 300 nm. d) Optical spectrum of the coupled cavities shown in (c); it shows the two splittings due to the coupling between cavities (g_{12}) and the coupling of counter-propagating modes (g_{cp}) in both cavities. Center wavelength is 1472.1 nm, with linewidths of 2.9 GHz ($Q = 70.3$k), $g_{cp} = 2\pi \times 6.36$ GHz and $g_{12} = 2\pi \times 28.2$ GHz.

5.2. Model

Although silicon is transparent for light with wavelengths longer than approximately 1.1 μm [134], if light intensity is high enough, two-photon absorption (TPA) [46, 135] may become important, creating enough free-carriers (FC) to significantly decrease the refractive index of the material [136]. In an optical cavity this process will lead to an increase, or a blue-shift, of the resonance frequency. On the other hand, the generated FC will absorb light

and generate heat, which will produce an increase in the refractive index due to the thermo-optic effect [137] and, consequently, shift the resonance to lower frequencies (red-shift).

As indicated in figure 5.2a, the optical filed is concentrated on the disk's edge, where it is absorbed and generates FC and heat. The generated FC have typical life-times on the order of nanoseconds [138, 139], most likely due to surface facilitated recombination [140]. Heat, on the other hand, is dissipated mainly to the substrate through the supporting oxide pedestal, which has poor heat conduction characteristics, leading to thermal life-times on the order of microseconds. The resonance frequency shift caused by these two effects alters the amount of energy stored inside the cavity, closes the feed-back loop represented in figure 5.2b and amplify small thermal fluctuation, which causes the self-pulsing of the stored and transmitted light.

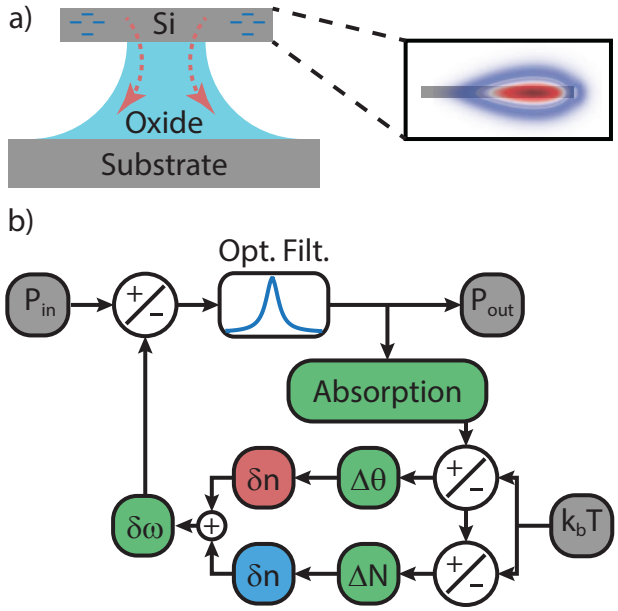

Figure 5.2: **Schematics of self-pulsing in silicon optical microcavities.** a) Scheamtics of the side-view of a micro-disk silicon cavity, indicating the formation of charge-carriers and the flow of heat through the pedestal. b) Schematics of the feed-back loop that produces the self-pulsing, with δU being the stored energy, δN the variation in charge-carrier density, δT the variation of temperature and $\delta\omega_0$ the variation of the resonance frequency.

For a single cavity we model this phenomenon with three coupled equations, one for the optical field (eq. 5.1), one for the density of charge carriers (eq. 5.2) and one for the temperature variation (eq. 5.3) [48, 49]:

$$\frac{da(t)}{dt} = i\left[\Delta + g_\theta \theta(t) + g_N N(t)\right] a(t) - \frac{\kappa + \alpha_{TPA} \mid a(t) \mid^2 + \alpha_N \left|N(t)\right|}{2} a(t) + \sqrt{\kappa_e P_{in}} \tag{5.1}$$

$$\frac{dN(t)}{dt} = -\gamma_{FC} N(t) + \beta_{FC} \mid a(t) \mid^4 \tag{5.2}$$

$$\frac{d\theta(t)}{dt} = -\gamma_{th}\theta(t) + \beta_{th}\left(\kappa_{lin} + \sigma_{Si} v_g N(t) + \alpha_{TPA} \mid a(t) \mid^2\right) \mid a(t) \mid^2 \tag{5.3}$$

The definition of the parameters of these equations are summarized on table 5.1.

Table 5.1: **Parameters of the self-pulsing equations.**

Parameter	Description	Parameter	Description
$\mid a \mid^2$	Intra-cavity stored energy	γ_{FC}	Free-carriers decay rate
N	Density of carriers	γ_{th}	Thermal decay rate
$\theta = T - T_0$	Temperature variation with respect to equilibrium	g_θ	Coupling coefficient of optical resonance to temperature variation
$\Delta = \omega_l - \omega_0$	Pump laser frequency detuning with respect to the optical resonance of the cavity	g_N	Coupling coefficient of optical resonance to the density of carriers
κ	Total linear decay rate of the optical cavity (includes linear absorption, scattering and coupling to the waveguide)	α_{TPA}	Two-photon absorption loss parameter
κ_e	Coupling rate between optical cavity and waveguide	α_N	Free-carrier optical loss parameter
κ_{lin}	Optical decay rate due to linear absorption	β_{FC}	Free-carrier generation parameter
v_g	Optical mode group velocity	β_{th}	Thermal source parameter
σ_{Si}	Silicon free-carrier absorption cross-section	P_{in}	Pump laser power

The coupling coefficients of the optical resonance to temperature and carrier density are given by

$$g_\theta = \frac{\omega_0}{n_g}\frac{dn}{dT} \tag{5.4}$$

and

$$g_N = \frac{\omega_0}{n_g}\frac{dn}{dN}, \tag{5.5}$$

where n is the refractive index, n_g is the group index of refraction, ω_0 is the optical resonance angular frequency in the absence of non-linear effects (cold-cavity) and T is the temperature. Note that the opposite effect of θ and N is implicit in this equations through dn/dT, which is positive, and dn/dN, which is negative.

The TPA and FC absorption parameters are defined as

$$\alpha_{TPA} = \frac{\Gamma_{TPA}\beta_{Si}c^2}{V_{TPA}n_g^2} \tag{5.6}$$

and

$$\alpha_N = \frac{\sigma_{Si}c}{n_g}, \tag{5.7}$$

where β_{Si} is the TPA constant for silicon and c is the speed of light.

The FC and thermal source parameters are defined as

$$\beta_{FC} = \frac{\Gamma_{FC}\beta_{Si}c^2}{2\hbar\omega_0 n_g^2 V_{FC}^2} \tag{5.8}$$

and

$$\beta_{th} = \frac{\Gamma_{disk}}{\rho c_p V_{disk}}, \tag{5.9}$$

where $\hbar$ is the reduced Planck constant and c_p is the material heat capacity. The parameters Γ_{TPA} and Γ_{FC} are overlap factors for TPA and FC absorption, respectively, while V_{TPA}, V_{FC} and V_{disk} are effective volumes available for TPA and FC absorption and the total disk volume, respectively. These parameters values are determined from finite element method (FEM) numerical simulations performed using COMSOL® and are defined as [133]

$$\Gamma_{TPA} = \frac{\int_{Si} n^4(\vec{r})E^4(\vec{r})d\vec{r}}{\int n^4(\vec{r})E^4(\vec{r})d\vec{r}}, \tag{5.10}$$

$$\Gamma_{FC} = \frac{\int_{Si} n^6(\vec{r})E^6(\vec{r})d\vec{r}}{\int n^6(\vec{r})E^6(\vec{r})d\vec{r}}, \tag{5.11}$$

$$V_{TPA} = \frac{\left(\int n^2(\vec{r})E^2(\vec{r})d\vec{r}\right)^2}{\int n^4(\vec{r})E^4(\vec{r})d\vec{r}} \tag{5.12}$$

and

$$V_{FC}^2 = \frac{\left(\int n^2(\vec{r})E^2(\vec{r})d\vec{r}\right)^3}{\int n^6(\vec{r})E^6(\vec{r})d\vec{r}}, \tag{5.13}$$

where $E(\vec{r})$ is the spacial distributions of the electric field amplitude.

Note that there are 3 distinct time scales present in equations 5.1 to 5.3. The fastest time-scale is the optical life-time ($\tau_{opt} = 1/\kappa$), which is in the order of tens of picoseconds for cavities with optical quality factors on the order of 80k. Then comes the FC life-time ($\tau_{FC} = 1/\gamma_{FC}$), in the order of a few nanoseconds. And the slowest time-scale is the thermal life-time ($\tau_{th} = 1/\gamma_{th}$), in the microsecond scale. One can then say that the optical field inside the cavity responds instantaneously to any FC or thermal variation. This means that the stored optical energy ($|a|^2$) is always in steady-state at any time, following any variations of N and θ instantly. We can then write $da/dt = 0$ and solve the first equation for $a(t) = a(N(t), \theta(t))$.

To do so it is necessary first to take care of a non-linear absorption term that depends explicitly on $a(t)$ in equation 5.1, namely the optical loss due to TPA. In fact, by solving the steady-state problem for the carriers density ($dN(t)/dt = 0$) it is possible to evaluate the contribution of each loss term in equation 5.1 at any given static amount of energy inside the cavity (fig. 5.3). For a typical input power of 1 mW to 2 mW, the stored energy inside of our cavities is on the order of 10 fJ. For this amount of energy both non-linear absorption coefficients are still smaller than the linear one (κ), but the terms due to TPA is much smaller than the other two,

unless for very little amounts of stored energy when it is comparable to the FC absorption term.

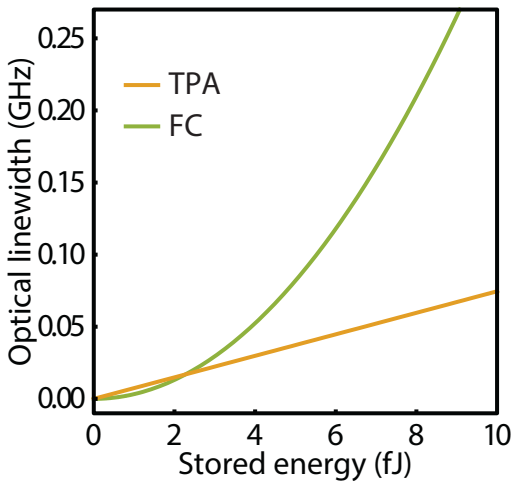

Figure 5.3: **Optica losses due to FC absorption, TPA and the linear losses as a function of the intra-cavity energy.**

Nevertheless, because the TPA term is always much smaller than the total optical decay rate, this term can be ignored and the steady-state solution of equation 5.1 can be simplified, resulting in a single and simple solution for the intra-cavity field amplitude, given by

$$a(t) = \frac{2\sqrt{\kappa_e P_{in}}}{2i\left(\Delta + + g_\theta \theta(t) + g_N N(t)\right) - \kappa + \alpha_N |N(t)|}. \tag{5.14}$$

Inserting equation 5.14 into equations 5.2 and 5.3 we obtain two equations of real arguments for the temperature variation and FC density, given by

$$\frac{dN(t)}{dt} = -\gamma_{FC} N(t) + \beta_{FC} U(t)^2 \tag{5.15}$$

$$\frac{d\theta(t)}{dt} = -\gamma_{th}\theta(t) + \beta_{th}\left(\kappa_{lin} + \sigma_{Si} v_g N(t) + \alpha_{TPA} U(t)\right) U(t), \tag{5.16}$$

where $U(t) = |\, a(t)\, |^2$, for simplicity. This approximation will be of special value when solving the problem of 2 cavities, as it will lead to a smaller memory consumption and shorter time to solve the problems. It is important to note that, although the TPA term was removed from the optical equation (eq. 5.1), this term is maintained in equation 5.3, minimizing the amount of approximations to solve the problem.

The material parameters used to properly solve the problem are obtained from the literature [47, 132, 133, 139, 141–143]. The thermal life-time was estimated by considering the conduction of heat from the top silicon layer through a truncated cone oxide pedestal, with top diameter given by the undercut of the disk obtained from optical images and bottom diameter was made equal to that of the disk. This produced a typical time-scale of 7 µs for the single cavity and 3.5 µs for the double cavity, with the difference given by the different undercut size in each sample. The FC life-time for both systems was assumed to be 4 times the value

presented in reference [139], which results in a timescale of 5.8 ns. We chose reference [139] because their measurements were performed in waveguides fabricated by the same foundry as the samples used in this work. The scale factor of the FC lifetime was chosen so that the time dependent solutions had similar frequencies to the experimental data. The linear absorption rate (κ_{lin}) was set to half of the intrinsic linear decay rate (κ_i), based on the results presented in reference [47].

Because the optical resonance shifts when the optical energy inside the cavity increases, it is necessary to solve equations 5.15 and 5.16 with a time dependent detuning ($\Delta = \Delta(t)$), as the example in figure 5.4. In this function $\Delta(t)$ varies from the blue side of the cold cavity ($\Delta/\kappa > 0$), until a given stop point on the red side of the cold resonance ($\Delta/\kappa < 0$). If this ramp is done too slowly, the solutions tend to show only static temperature and FC density. That is because the model doesn't take noise into account, hence there is nothing to perturb the solution out of its equilibrium.

On the other hand, if the ramp is done fast enough such that oscillations appear in the solutions, it typically causes artifacts on the solutions due to the variations of the stored optical energy being on the same time-scale of the phenomena of interest. To overcome this problem, the system of equations is solved multiple times, changing the stop detuning in each solution and storing only the data related to the times when Δ is static (red line in fig. 5.4). In this way the ramp of detuning can be done very quickly without affecting the final solution.

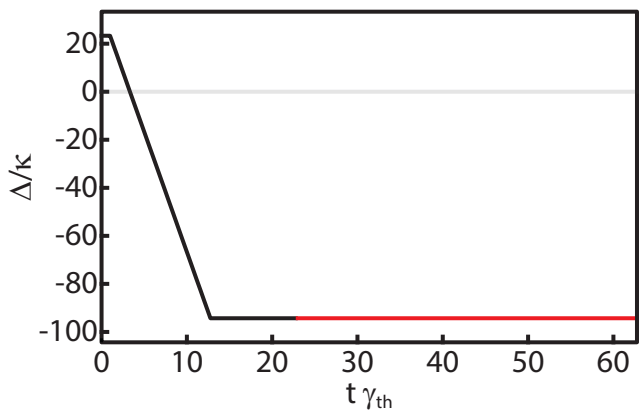

Figure 5.4: **Time dependent detuning function.** The black region simulates the laser frequency sweep, taking the optical resonance non-linear shift into account. The red region is where time dependent data is stored and its Fourier transform are evaluated. The horizontal axis is time normalized by the thermal life-time. The vertical axis is the laser detuning with respect to the cold cavity, normalized by the total cold-cavity linewidth.

An important observation is that the Δ values presented in figure 5.4 are relative to the cold cavity, i.e., without considering the non-linear resonance shift. As will be clear later in this section, the effective detuning is always positive with respect to the shifted resonance position. Also, we note that these numerical solutions presented here were obtained before proper characterization of the FC and thermal lifetimes of the samples, what invariably leads to deviations in quantitative results between model and experiment. Nevertheless, good agreement

in the general behavior of the systems is achieved for both single and double cavity cases.

Single cavity

To reproduce the single cavity experiments the optical modes are modeled with a splitting due to coupling of counter propagating modes [69, 70]. The expected optical transmission spectrum for a low power pump is shown in figure 5.5, with an optical decay rate $\kappa = 2\pi \times 2.5$ GHz and a coupling rate between modes $g_{cp} = 2\pi \times 13$ GHz. The cavity-waveguide coupling rate (κ_e) is 1.1 GHz and the central wavelength was set to approximately 1471 nm. The list of values for all parameters used in this case are listed in appendix H.

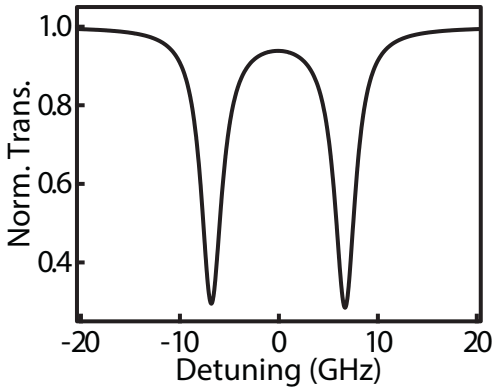

Figure 5.5: **Numerical optical transmission spectrum of a single cavity with coupling of counter-propagating modes.** The coupling rate between modes is 13 GHz and the total optical decay rate is 2.5 GHz.

The equations are solved in Mathematica® and, for a given final detuning value, result in time-traces like the ones shown in figure 5.6, which show the traces over one complete cycle of oscillation. By substituting the $\theta(t)$ and $N(t)$ solutions into equation 5.14 and calculating the normalized time dependent transmission, the curve presented in figure 5.6a is obtained. Figure 5.6b shows the frequency shift of the resonances relative to the equilibrium position, which is given by

$$\Delta\omega = g_\theta \theta(t) + g_N N(t) - \overline{\Delta\omega}, \tag{5.17}$$

where $\overline{\Delta\omega} = g_\theta \overline{\theta} + g_N \overline{N}$ is the shift caused by the mean variation of both temperature and FC density, with the overbar indicating time average. Figures 5.6c and 5.6d show the time behavior of FC and temperature variation over a single period. The colors indicate the regions where a relative blue-shift (blue) or red-shift (red) occurs, respectively.

From these traces it is already possible to understand the origins of the different features in the transmitted signal. At some point on the oscillation cycle, the FC density is at minimum and heat generated by carriers in the previous period is dissipated, causing the resonance to blue-shift and approach the frequency of the pump laser. Due to the non-linear (Lorentzian) build-up of optical energy inside the cavity, FC density start to quickly increase, increasing the blue-shift rate, up to the point where one of the peaks completely passes by the

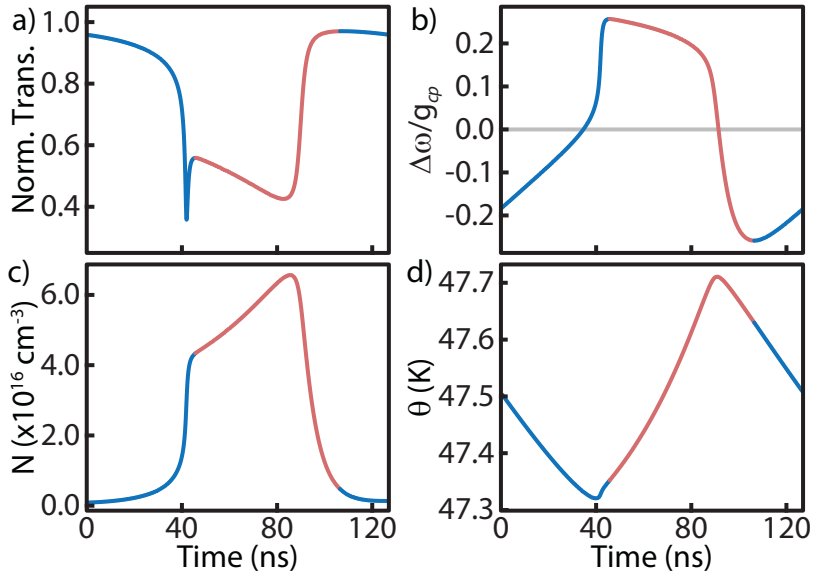

Figure 5.6: **Numerical time-traces of a self-pulsing single optical cavity over one period.** a) Optical transmission normalized by the input power P_{in}. b) Total resonance shift with respect to the mean resonance shift normalized to g_{cp}. c) Free-carriers density. d) Temperature variation with respect to the cold-cavity equilibrium value. The colors indicate the regions where there is relative red and blue-shift of the resonance.

pump laser, causing the sharp deep at the beginning of the pulse. Then the generated FC start to absorb light, generating heat and red-shifting the resonance, until another instability point is reached, when the FC density quickly depletes, rapidly red-shifting the resonance until another cycle begins. It is interesting to observe that the frequency shift over one period of oscillation is always much smaller than the coupling rate g_{cp} (fig. 5.6b), but it is larger than the linewidth of the peaks ($\kappa = 2\pi \times 2.5$ GHz). In fact it is large enough such that one of the peaks shifts over the pump laser position, causing the sharp deep in the beginning of the pulse.

The dynamics of the resonant frequency are more easily observed by plotting the optical spectra of the cavity, as would be observed with a weak probe laser, for each position in time. This is accomplished by plotting the transmission obtained with equation 5.14 for instantaneous values of $\theta(t)$ and $N(t)$, which produces the spectrogram presented in figure 5.7, where the vertical line close to 10 GHz marks the position of the pump laser frequency. Note that the laser is always blue-detuned with respect to the mean resonance position ($\Delta - \overline{\Delta\omega} = 0$).

Observe that the resonance path reproduces exactly the trace presented in figure 5.6b, and now it is possible to see the two moments when the bluer resonance passes by the laser position, causing the minima in the pulse pattern. Also, observe that because the two resonances are of the same cavity, experiencing then the same shifts due to the FC and temperature variations, both resonances move exactly in phase, never changing their relative distance.

These solutions also allow to obtain other information about the process by obtaining the phase-space diagram of the transmitted light and the $N \times \theta$-space diagram. The former (fig. 5.8a) is obtained by plotting the amplitude of the transmitted signal versus its time deriva-

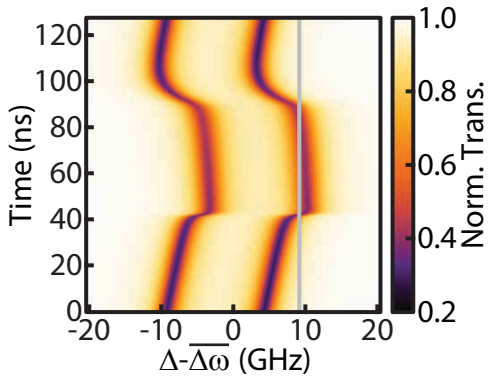

Figure 5.7: **Numerical time-dependent optical transmission spectrogram.** The vertical line indicates the position of the pump laser frequency.

tive, while the latter is a simple plot of the FC density versus the temperature variation θ. The fact that the process presented here is a self-oscillation one is again confirmed by the closed paths these diagrams present. But more than that, these diagrams are of help in the identification of different state of oscillations for the double cavity problems, as will be clear later in this section. To obtain a phase-space diagram that resembles that of the experimental data, a low-pass filter with cutoff frequency at 800 MHz was used on the transmitted signal of this model. This cutoff was chosen because it is the same cutoff frequency of the detector used on the experiments.

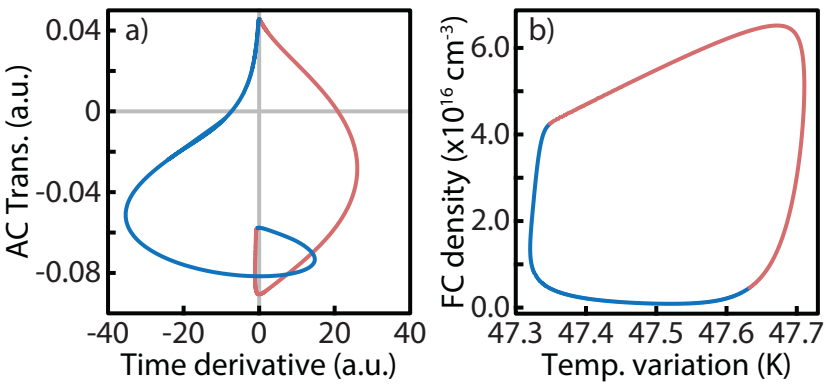

Figure 5.8: **Numerical phase and $N-\theta$ space of a self-pulsing single optical cavity.** a) Phase space of the transmitted light of a self-pulsing cavity. This plot was obtained after passing the signal through a low-pass filter with cutoff frequency at 800 MHz, simulating the measurement setup. b) $N-\theta$ space of a single self-pulsing cavity. The colors indicate the regions where there is relative red and blue-shift fo the resonance.

Finally, taking the Fourier transform of the optical transmission time-trace (fig. 5.6a) for different static detuning positions produces a spectrogram, with the time axis is substituted by a pump wavelength axis (fig. 5.9). The pump wavelength dependent transmission (fig. 5.9a) is obtained by taking the average of the oscillating transmission signal for each detuning. The pulses spectra present various harmonics, spanning up to the GHz scale, which is expected for the square-like pulses produced in this process. Note that the detuning for which oscillations start is very well marked by both an abrupt increase in the average transmitted

signal and the appearance of the peaks in the spectrum. This behavior, as will be shown in section 5.4 is precisely what is observed in experiments. Also, the first harmonic frequency presents a high detuning dependency, which is observed in the time domain as a change in the pulses duty-cycle, i.e., the ratio between the time the pulses are high and the oscillation period.

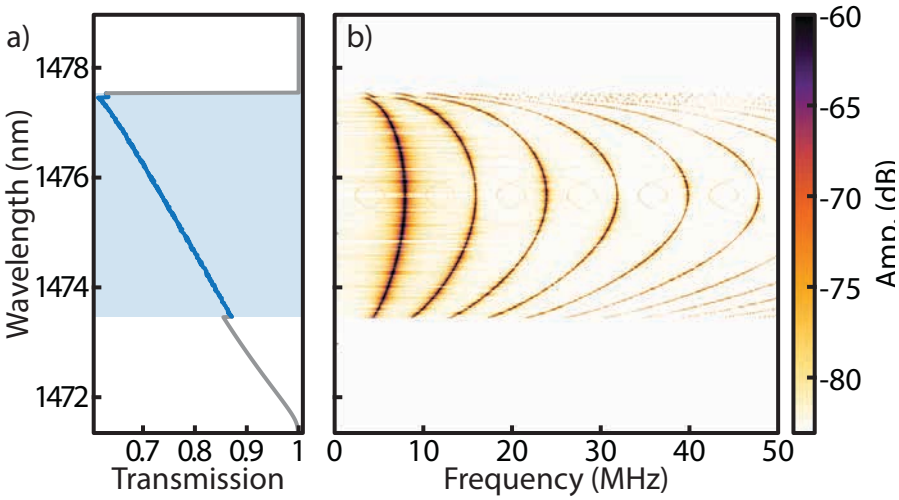

Figure 5.9: **Numerical wavelength dependent spectrogram of a self-pulsing single optical cavity.** a) Normalized transmission of a detuning sweeping pump laser, with the typical triangular shape due to non-linear bi-stability [133]. The blue region is where the self-pulsing occurs. b) Detuning dependent spectrogram of the transmitted self-pulsing light. The vertical scale follows the same scale in (a).

Double cavity

As shown in figure 5.10a, in this case one of the cavities is coupled directly to the waveguide (which will be called C_1), while the other (C_2) only receives light that coupled into C_1 (see appendix A for more details on the optical equations). Figure 5.10b shows the optical transmission spectrum for this system, as it would appear in a low input power measurement. The coupling rate between cavities is $g_{12} = 2\pi\times 28$ GHz, and the resonances are centered around 1471 nm with total linewidths $\kappa = 2\pi\times 2.5$ GHz.

Note that there is a slight asymmetry in the peaks extinction ratio; that is because a slight mismatch between the resonances of C_1 and C_2 is taken into account. This mismatch was created by making the C_1 with resonance ω_0 and C_2 with resonance $\omega_0 - \delta_0$, where δ_0 is a positive constant, making the resonance of C_2 redder than that of C_1. In this case the difference is $\delta_0 \approx 2\pi\times 1$ GHz. Besides this resonance frequency mismatch, the cavities are considered to be identical in terms of optical losses and material properties, as well as FC and thermal life-time.

Also, in the single cavity case it was demonstrated that the splitting due to coupling of counter-propagating modes doesn't add sensible information to the problem. At most it would cause split dips in the transmission time-trace, and only if the shift caused by temperature

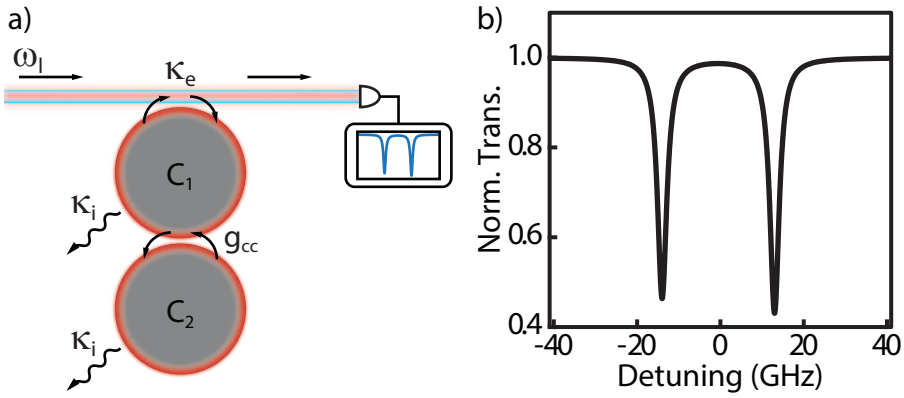

Figure 5.10: **Schematics and transmission spectrum of a coupled cavity system model.** a) Schematics of a coupled cavity system. The coupling between cavity modes is given by g_{12}. b) Optical transmission spectrum of a pair of coupled resonances. The coupling rate between modes is 28 GHz and the loaded optical decay rate is 2.5 GHz. The difference in extinction ratio is due to a mismatch in resonance frequency of 1 GHz between the two cavities.

and FC is large enough for both peaks to pass by the pump laser frequency. Hence we didn't take this feature into account for the double cavity problem, even though the real device presents two kinds of splitting, a larger one for the coupling between cavities and two smaller ones for the coupling of counter-propagating modes in each cavity.

It is important to note that the two peaks in the spectrum of figure 5.10b are not those of the individual resonances of C_1 and C_2. Instead, these are what are commonly named super-modes of the coupled system, which are comprised of symmetric and anti-symmetric combinations of individual cavity modes, and their distance is related to the coupling rate g_{12}. Throughout this chapter we will refer to these resonances by coupled resonances, in this manner distinguishing them from the individual cavities' resonances. See reference 96 for more details on the coupled mode theory and the relation between coupled resonances and individual ones. The function used to generate the spectrum in figure 5.10b is presented in appendix A.

In the double cavity case the importance of reducing the number of equations for each cavity becomes apparent. The whole problem involves three equations per cavity, and the equation for the optical field amplitude ($a(t)$) is complex, which in practice increases the number of equations to four per cavity, because any numerical solver will make $a(t) = A(t) + \mathrm{i}B(t)$ before starting to solve the system of equations. Removing the equation for $a(t)$ by the adiabatic approximation (the field responds instantly to the temperature and FC variations) reduces the problem to a set of two real equations per cavity, making the problem much simpler and quicker to solve. The system of equations for two cavities is given by

$$\frac{dN_1(t)}{dt} = -\gamma_{FC}N_1(t) + \beta_{FC}U_1(t)^2 \tag{5.18}$$

$$\frac{d\theta_1(t)}{dt} = -\gamma_{th}\theta_1(t) + \beta_{th}\left(\kappa_{lin} + \sigma_{Si}v_g N_1(t) + \alpha_{TPA}U_1(t)^2\right)U_1(t)^2 \tag{5.19}$$

$$\frac{dN_2(t)}{dt} = -\gamma_{FC}N_2(t) + \beta_{FC}U_2(t)^2 \tag{5.20}$$

$$\frac{d\theta_2(t)}{dt} = -\gamma_{th}\theta_2(t) + \beta_{th}\left(\kappa_{lin} + \sigma_{Si}v_g N_2(t) + \alpha_{TPA}U_2(t)^2\right)U_2(t)^2, \tag{5.21}$$

where N_i, θ_i and U_i are the FC density, temperature variation and intra-cavity energy of cavities C_1 and C_2. Notice that there is no direct coupling between N and θ of the two cavities, instead it is mediated exclusively by the optical field of the cavities, whose couping is implicit through U_i, which are given by

$$U_1(t) = \frac{4\left(4\Delta_2^2 + \kappa_2^2\right)\kappa_e P_{in}}{\left(4\Delta_1^2 + \kappa_1^2\right)\left(4\Delta_2^2 + \kappa_2^2\right) + g_{12}^2\left(2\kappa_1\kappa_2 - 8\Delta_1\Delta_2\right) + g_{12}^4} \tag{5.22}$$

$$U_2(t) = \frac{4g_{12}^2\kappa_e P_{in}}{\left(4\Delta_1^2 + \kappa_1^2\right)\left(4\Delta_2^2 + \kappa_2^2\right) + g_{12}^2\left(2\kappa_1\kappa_2 - 8\Delta_1\Delta_2\right) + g_{12}^4}, \tag{5.23}$$

where $\Delta_1 = \Delta_0 + g_\theta\theta_1 + g_N N_1$ and $\Delta_2 = \Delta_0 + g_\theta\theta_2 + g_N N_2 + \delta_0$ are the effective detunings due to the variation of θ and N in each cavity, with Δ_0 being the detuning with respect to the unperturbed resonance of C_1; and $\kappa_{1,2} = \kappa + \alpha_2 N_{1,2}$ are the decay rates of each cavity, contemplating both linear and non-linear contributions.

The process to solve this set of equations is the same used for the single cavity case, with a time dependent $\Delta_0 = \Delta_0(t)$, whose final position varies, and the time traces and Fourier transforms are generated for different static Δ_0. Figure 5.11 shows the resulting detuning dependent spectrogram, together with the non-linear transmission created by averaging the pulsing optical transmission for each detuning. In this case different features become apparent in the spectrogram and they were marked with different colors in the transmission curve for later reference on the time-traces. The values of the parameters used in this case are also listed in appendix H.

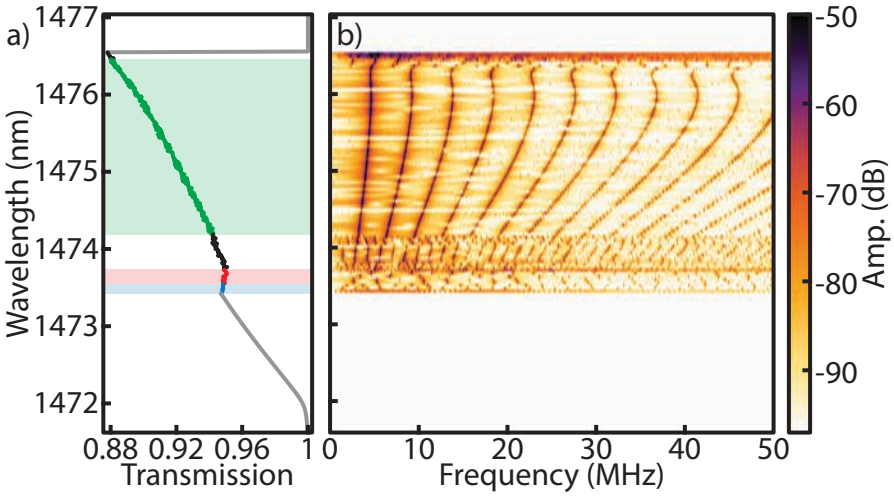

Figure 5.11: **Numerical wavelength dependent spectrogram of a self-pulsing double optical cavity system.** a) Normalized transmission of a detuning sweeping pump laser, with the typical triangular shape due to non-linear bi-stability [133]. b) Detuning dependent spectrogram of the transmitted self-pulsing light. The vertical scale follows the same scale in (a).

The colors in the transmission curve (fig. 5.11a) indicate regions of interest in which

we focused. Figure 5.12 shows examples of the transmitted signal time-traces for each of the indicated regions. For the first case (blue) a low repetition rate pulse appears, much similar to those of a single cavity, with a phase diagram indeed very similar to that of figure 5.8a, as expected if one of the cavities' resonances is practically stationary while the other oscillates. For the red region of the spectrogram, two pulses with distinct amplitudes appear, alternating one after the other, what becomes more evident in the phase diagram that presents two paths. This is indicative that the individual resonances might present complex dynamics, with intricate variations of their frequencies. Finally, on the green region the pulse shape becomes even more distinct from the previous two, with another dip appearing before its end, besides the first sharp dip in the beginning of the pulse. This second peak causes a distinct signature in the phase diagram that, despite showing a single path again, presents a second small loop at lower amplitudes due to the second slower dip.

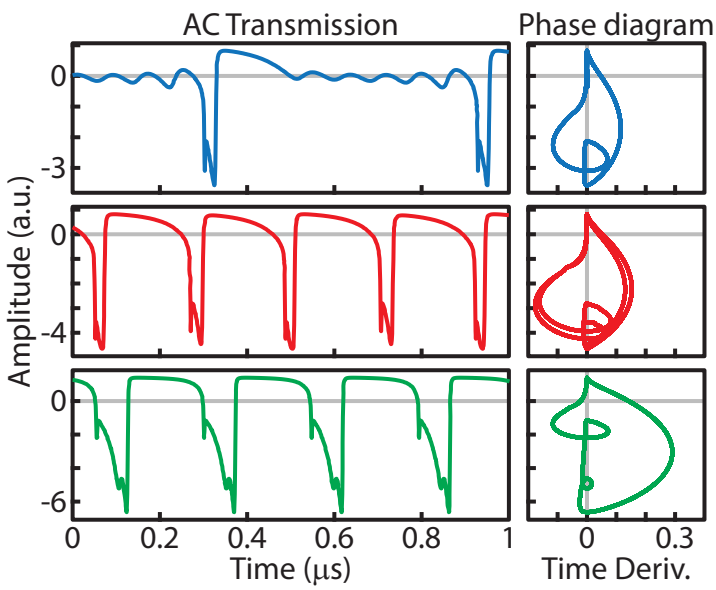

Figure 5.12: **Numerical transmission time-traces of a self-pulsing double optical cavity system.** Left) AC optical transmission, obtained by subtracting the RMS value from the oscillation. Right) Phase diagrams of the traces on the left.

It is possible to identify what differentiates the colored regions by looking at the temperature and FC time-traces in each one, as shown in figure 5.13. For better comparison on the temperature time-traces, only the oscillating (AC) component is shown by subtracting the root-mean-square (RMS) from the total solution. For the blue region, cavity C_1 (the one coupled to the waveguide) has both its temperature and FC density fluctuations much smaller than C_2, indicating that only C_2 has its resonance frequency significantly shifting and participating in the pulse formation. In the red region, both cavities have similar FC and temperature variation amplitudes of oscillation, but the amplitude of oscillation for each cavity seems to alternate. This creates complex features on the transmitted light, as the dominance of thermal and FC effects on the individual resonances vary considerably.

Finally, in the green region, both cavities temperature variation have very similar

amplitudes, but a difference in the phase of the oscillations also causes the individual resonances to shift at different times. Moreover, the FC density of C_1, although presenting higher amplitude, presents much sharper pulses with a significant delay with respect to the FC density in C_2. This also produces complex dynamics for the individual cavity resonances, also presenting signatures of the coupling between cavities on the optical transmission pulses. These results indicate that the optical coupling between self-pulsing cavities is capable of coupling the FC density and temperature oscillations of them, causing them to synchronize as the phase of the oscillations seem to be always locked in these three situations.

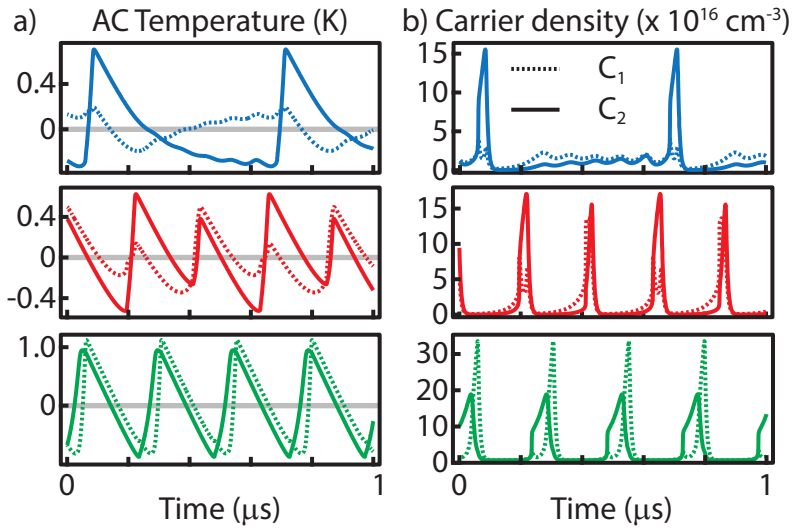

Figure 5.13: **Temperature variations and FC density of a self-pulsing double optical cavity system.** a) AC temperature variation of the two cavities for each of the marked regions in fig. 5.11a. This is obtained by subtracting the root-mean-square of each temperature solution. b) FC density of the two cavities for each of the marked regions in fig. 5.11a.

To better understand the causes of the different features in the transmitted signals, we can look at the time dependent individual resonance frequencies, as shown in figure 5.14. In figure 5.14a the frequency shifts of the individual resonances, $\Delta\omega_1 = g_\theta \theta_1 + g_N N_1$ and $\Delta\omega_2 = g_\theta \theta_2 + g_N N_2 - \delta_0$, displaced by the mean shift $\overline{\Delta\omega} = \left[\left(g_\theta \overline{\theta_1} + g_N \overline{N_1}\right) + \left(g_\theta \overline{\theta_2} + g_N \overline{N_2}\right)\right]/2$, are plotted normalized by the optical coupling rate g_{12}. This shows the expected high amplitude of the C_2 resonance, while C_1 presents very low amplitude of oscillations.

Figure 5.14b shows the distance between the individual resonances, which is given by $\Delta\omega_1 - \Delta\omega_2$, again normalized by g_{cp}. Note that the resonance frequency difference crosses zero twice in a period, which obviously coincides with the moment when the C_1 and the C_2 resonance frequencies cross each other, as observed in figure 5.14a. In terms of coupled mode theory this means that an anti-crossing between the coupled resonances happens twice every period, in this case with one of the individual resonances moving while the other remains almost static.

This anti-crossing process becomes more apparent looking at the time dependent spectrogram of the coupled resonances shown in figure 5.15. In this figure the colors represent

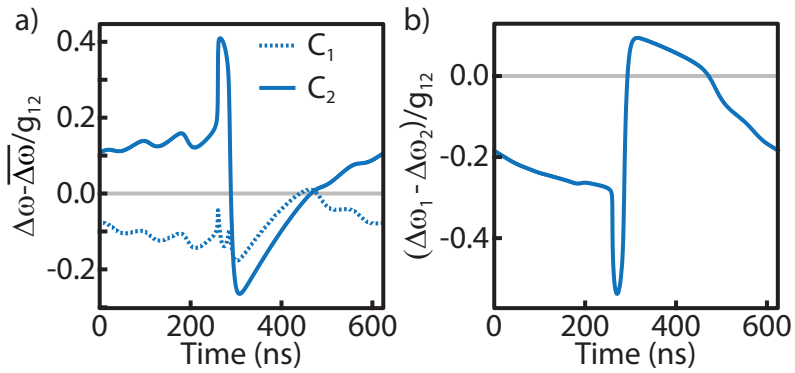

Figure 5.14: **Time-traces of individual resonance frequencies shifts of coupled optical cavity system – blue.** a) Individual resonance frequencies shifts normalized by g_{12}. b) Spectral distance between individual cavity resonances normalized by g_{12}.

the extinction ratio of the transmission, with darker colors for lower transmission, and the horizontal line indicates the effective detuning of the pump laser. Before the pulse happens it is possible to note that the redder resonance (farther from the laser) has lower transmission (it is darker) than the bluer. Right after the pulse this relation has completely inverted, with the bluer resonance having the lower transmission dip, indicating the first anti-crossing had happened. Then, the second anti-crossing happens and the transmission dip relation returns to the original situation of the beginning of the period.

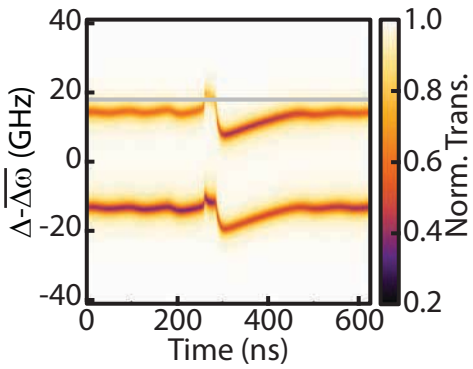

Figure 5.15: **Optical spectrogram of a coupled optical cavity system – blue.** Time-dependent optical transmission spectrogram, with the horizontal line indicating the pump laser frequency.

Although we can see this resonance frequency dynamics from the model's solutions, there seems to be little signature of them in the transmitted pulsed signal (fig. 5.12) for this first case. The only signature on the pulses that is not present in the single cavity case is the small oscillation of the transmitted signal before the pulses, which are also observed in the experimental data as will be shown later in this chapter.

Now, looking at the resonance dynamics for the red region of the spectrogram (fig. 5.16) we observe much more complex dynamics for the individual resonances. Note that the anti-crossings happen once for each pulse in the transmitted signal. Noticeably in this case the two individual resonances have significant shifts, but their dynamics are much more com-

plex than on the previous case. For the first pulse, both individual resonances suffer a strong blue-shift, but there is a delay for C_2, which causes the anti-crossing to occur when C_1's resonance is already red-shifting while C_2's is still going through a blue-shift (C_2). For the second anti-crossing, on the other hand, C_1's resonance blue-shift is weaker than that of the C_2's resonance, but when they both red-shift C_2's resonance has a much steeper change and crosses the other resonance.

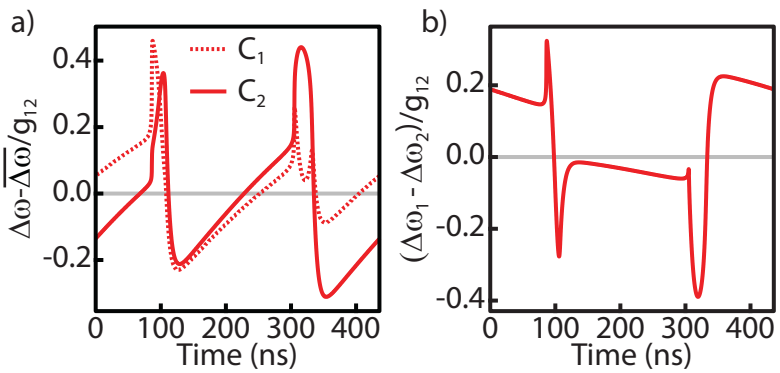

Figure 5.16: **Time-traces of individual resonance frequencies shifts of coupled optical cavity system – red.** a) Individual resonance frequencies shifts normalized by g_{12}. b) Spectral distance between individual cavity resonances normalized by g_{12}.

This behavior is explained by the temperature and FC dynamics, as for the first pulse they cause a strong but quick blue-shift of C_1's resonance while the C_2's resonance blue-shift is delayed and slower, causing the resonances to switch places Again this anti-crossing is apparent in the coupled resonances spectrogram, with the depth of each resonance inverting every two pulses, which determines the period of oscillation in this situation. This can also be interpreted as if C_1's resonance is oscillating with half the frequency of C_2's resonance and the much smaller amplitudes observed each two pulses in C_1's temperature, FC density and resonance are only a weak response due to the variations on the stored energy. This would mean that the two cavity pulses are locked by matching different harmonics of their spectrum, being the first of C_2's with the second of C_1's in this case.

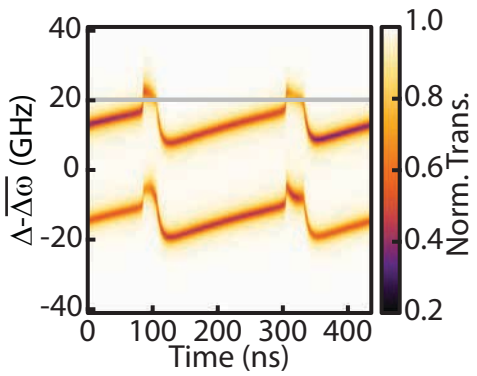

Figure 5.17: **Optical spectrogram of a coupled optical cavity system – red.** Time-dependent optical transmission spectrogram, with the horizontal line indicating the pump laser frequency.

And again, the anti-crossings are observed when the optical spectrogram is analyzed, with the bluer resonance presenting lower transmission ratio (darker) than the redder before the first pulse. After the first pulse we observe that the contrast between bluer and redder extinction ratios is much lower, although it is still noticeable that the redder resonance has a lower transmission ratio, until the second pulses happen and the relation starts another cycle.

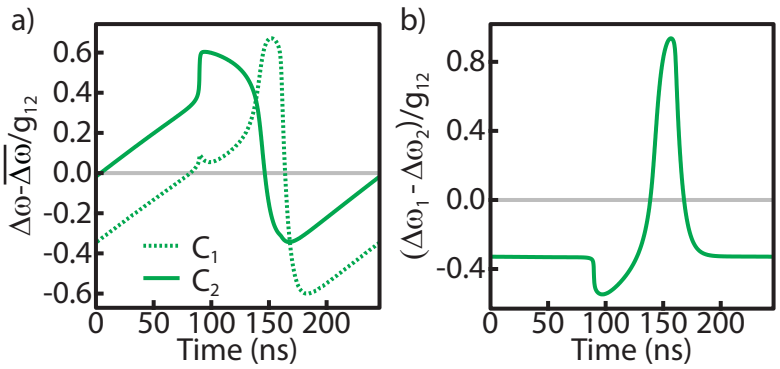

Figure 5.18: **Time-traces of individual resonance frequencies shifts of coupled optical cavity system – Green.** a) Individual resonance frequencies shifts normalized by g_{12}. b) Spectral distance between individual cavity resonances normalized by g_{12}. c) Time-dependent optical transmission spectrogram, with the horizontal line indicating the pump laser frequency.

And finally, the analysis of the green region (fig. 5.18) shows the origin of the second dip in a single pulse. Again the two anti-crossings occur in the same pulse but, differently from the first case (blue traces), both individual resonances are shifting with significant amplitude. From figure 5.18a it is clear that in both times the individual resonances cross, they are shifting in opposite directions, i.e., when one is suffering a red-shift the other is always going through a blue-shift. Moreover, when the first crossing occurs, both individual resonances present high instantaneous blue-shift, such that one of the coupled resonances is always bluer than the pump laser. Then, when the anti-crossing takes place, the transmission oscillates once before the coupled resonances return to the initial position.

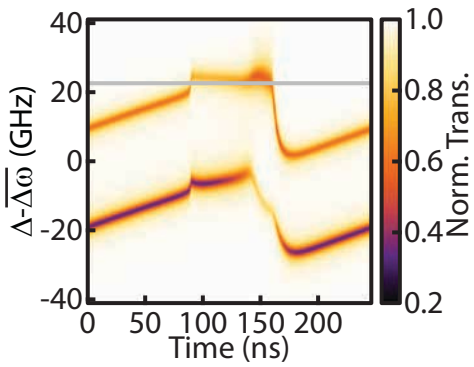

Figure 5.19: **Optical spectrogram of a coupled optical cavity system – green.** Time-dependent optical transmission spectrogram, with the horizontal line indicating the pump laser frequency.

Looking at the optical spectrogram of the coupled resonances (fig. 5.19) it is pos-

sible observe the first anti-crossing happening after the bluer resonance have already become bluer than the input laser, as its transmission gets lower than the redder resonance. And this is what distinguishes this case from the first. There the anti-crossing only happens after the bluer coupled resonance has already become redder than the pump laser. And in this case we can say that the oscillations are locked by matching their first harmonics, in contrast to the second case.

These results show the overall expected results from the experimental measurements. Similarly to what has been demonstrated in coupled optomechanical cavities [12, 13], the optical coupling can mediate the coupling and synchronization of self-pulsing in silicon optical micro-cavities. Also, it was possible to distinguish very different operation conditions, with very distinct transmission signals to identify each one.

On the following sections the processes to characterize FC and thermal life-time of the samples will be resented, as well as the experimental results of the experiments with the self-pulsing in a single cavity and in a two coupled cavities system.

5.3. Sample characterization

Among the parameters involved in the modeling of self-pulsing in silicon optical cavities, three of them are intrinsically design or fabrication dependent; the optical decay rate, the thermal lifetime and the FC lifetime. The optical decay rate depend on the fabrication because the dry etching process typically leaves damaged borders, which can cause scattering in disk optical cavities and increase the optical losses. It is easily measured by probing the cavities optical spectrum, and was presented in section 5.1. The thermal lifetime depends on the pedestal geometry, which is not always accessible, usually requiring destructive imaging techniques to be properly characterized, such as cutting the sample for cross section analysis. Finally, the FC lifetime may depend on the disk geometry and fabrication because surface effects contribute to the recombination of the generated FC [140, 144, 145].

To better determine if the values used in the numerical analysis previously described are consistent with the experimental data, we performed the measurements of these parameters in our samples. The thermal life-time was measured for the single and double cavity samples, because the two systems have different pedestal dimensions. The FC lifetime was measured only for the single cavity, because it is expected to be the same for both given that the two optical cavities are nominally identical and were fabricated in the exact same process.

FC lifetime

The FC lifetime is measured in a pump and probe scheme (fig. 5.20). For this a pump laser, with relatively high power (approximately 1 mW, enough to set the cavities into self-pulsing regime), is tuned close to a resonance at 1470 nm and pulsed with an electro-optical amplitude modulator (Covega's MACH-10 063) able to respond up to 10 GHz (response

time of 100 ps). The modulator is driven by a 1 ns rise-time pulse generator (Agilent's 81160A), which is much faster than the thermal lifetime to guarantee that the thermo-optical effect doesn't interfere with the characterization of the FC life-time. The detuning of the pump is such that, although it has enough power to produce self-pulsing, there is not enough power inside of the cavity to start the oscillations. A probe laser, with much lower power (approximately 10 µW), is tuned half a linewidth from another resonance close to 1520 nm. Due to the short time of the measurement (less than one second) no locking of the lasers to the resonances is necessary.

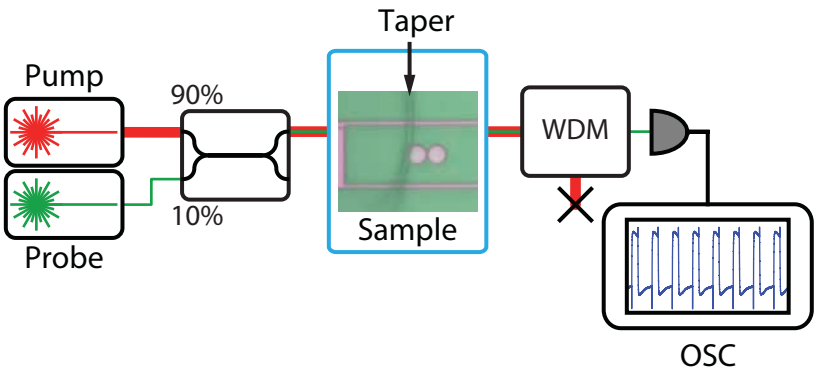

Figure 5.20: **Schematics of a pump and probe setup.** A 90:10 fiber coupler joins pump and probe lasers and send them to the taper. After the sample pump and probe are separated using a wavelength division multiplexer (WDM).

Pump and probe lasers are coupled with a 90:10 fiber coupler and sent into the taper. After the sample, pump and probe are separated using a wavelength division multiplexer (WDM). At this point the pump is discarded and only the probe, after passing through an optical amplifier, is measured with a fast photodetector, whose photocurrent is measured in the oscilloscope. The pump was measured before the sample to confirm the 1 ns rise time.

The quick changes of the pump laser power coupling into the cavity causes the resonances to shift due to an increase or decrease in FC density caused by TPA. Because the modulation timescale is much shorter than the thermal life-time, it is possible to observe changes in the probe transmission exclusively due to the generation of FC. Figure 5.21 shows the experimental data obtained with the long pulses due to the slow thermal effect, while the short spikes are caused by the FC generation.

The whole data presents 82 FC dependent peaks, 41 rising and 41 dropping; the rising pulses were isolated and a modified function of a charging capacitor fitted to them. To derive the best fitting function, we assumed first that the change in resonance frequency due to FC is small enough, such that the probe laser transmission dependency on the detuning to the probe resonance can be considered linear. Also, the change in the frequency of the probe resonance is given by $\Delta\omega = g_N N$ and this is what causes the rising/dropping of probe transmission. Because the cavity can be assumed to instantly respond to the FC density variations, together with the linear dependency with detuning, the time dependent probe transmission can be considered a direct measurement of the FC density time dependence.

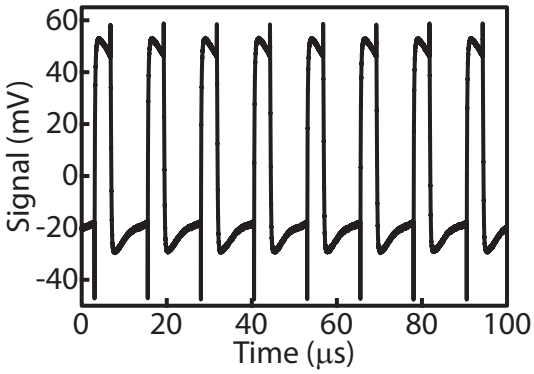

Figure 5.21: **Pulses for FC lifetime characterization.** The probe signal presents the slower pulses due to the thermo-optical effect, together with sharp peaks due to the response of the cavity to the generation of FC.

The basic time dependency of FC generation is given by equation 5.15, which is the same equation of a charging capacitor but with a source more complex than the typical step-function typically used in the electronics text-book counterpart. Hence it is possible to rewrite equation 5.15 with a generic time-dependent source, $f(t)$:

$$\frac{dN(t)}{dt} = -\gamma_{FC}N(t) + f(t) \ . \tag{5.24}$$

The FC are generated by the intra-cavity energy squared, which in turn is proportional to the modulator's output power squared. It is easy to show that, to a first order approximation, the output power squared of the modulator follows the electrical drive input, if the latter is slow enough compared to the modulator response-time. This means that the source in equation 5.24 can be set as a 1 ns rising function, obtained assuming that it is the output of an RC circuit responding to a step function, which is given by

$$f(t) = A0\left(1 - e^{-\gamma_{mod}(t-t_0)}\right) \ \text{ for } \ t > t_0, \tag{5.25}$$

where A_0 is an arbitrary amplitude that can be normalized to unit, t_0 is a given time when the pulse starts and $1/\gamma_{mod} = \tau_{mod} = 1$ ns is the pulse rise-time, which equals to that of the pulse generator because it is much slower than the 100 ps response time of the modulator. We discarded the DC component related to the mean intra-cavity energy as it will be only a static shift of the FC density. Moreover, it is known that the FC density can affect the carriers life-time if it is too high, for instance due to Auger recombination [140]. Because of the pump laser detuning, absorption is expected to generate FC enough just to produce a measurable change on the optical resonance, which can be accomplished with approximately 10^{15} cm^{-3} of FC density causing less than $\kappa/10$ of change in the resonance frequency. Hence, we do not expect the carriers density to affect their life-time.

Inserting the source equation (eq. 5.25) into the FC equation (eq. 5.24) the problem can be analytically solved resulting in the expected FC function when it responds to such a

modulation. Discarding the DC component due to the mean intra-cavity energy the solution is given by

$$N(t) = A0\left(\gamma_{mod}\left(1 - e^{-\gamma_{FC}(t-t_0)}\right) + \gamma_{FC}\left(e^{-\gamma_{mod}(t-t_0)} - 1\right)\right) \quad \text{for } t > t_0. \tag{5.26}$$

Figure 5.22 shows the 41 rising pulses, shifted all to start at $t_0 = 0$ s, with equation 5.26 fitted to them. In order to make the picture clearer the individual fitted curves are not shown, with a curve with the average fitting parameters plotted instead. The resulting FC lifetime is 508 ± 3 ps, calculated as the mean value of the individual fitted parameters and the error given by their standard deviation.

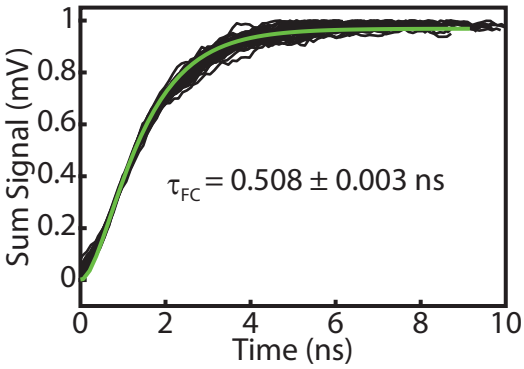

Figure 5.22: **Fit of FC lifetime data.** 41 rising pulses displaced to $t_0 = 0$ s and normalized (black), with equation 5.26 plotted with the average of 41 fitted parameters (green).

This value is one order of magnitude smaller than the used in the theoretical model. However it is not expected for a 2 µm radius silicon disk to have such a small FC lifetime, specially comparing to the value of 1.45 ns measured by Aldaya *et al.* [139]. In their case the device used to measure the FC lifetime was a Mach-Zehnder interferometer with arms composed by single-mode TE waveguides, which means that the cross-section of the waveguide is on the order of 500 nm. This means that their surface area to volume ratio is much larger than that of our micro-disks, which should make their lifetime shorter [140] than mine. Even considering that the surfaces of our devices have a thin native oxide layer, which is known to decrease carriers life-time [140], at most one should expect similar values for our disks and their waveguides.

The long excitation pulse rise-time we used probably hinders the measurement, even though we tried to correct for this using a modified fitting function. Moreover, errors in setting the probe detuning can also affect this measurement, hence it would be best to not consider this value as valid until the procedure is repeated with these issues addressed. Nevertheless, this result doesn't change the validity of the qualitative comparison between theoretical model and experimental results, what will be done later in this chapter.

Thermal lifetime

The thermal lifetime is also measured with a pump and probe setup, exactly as the one shown in figure 5.20. The procedure is detailed in Victor Brasch's PhD thesis [146] and the general idea is represented in figure 5.23. Sweeping the wavelength of a pump laser through one of the cavity's resonances causes all of them to shift due to absorption and the thermo-optical effect. A static weak laser nearby another resonance will probe this second peak twice: (1) while the resonances are all shifted to higher frequencies; (3) when they all return after the probe resonance has reached its maximum shift (2) and all the resonances return to their original position as the cavity cools down.

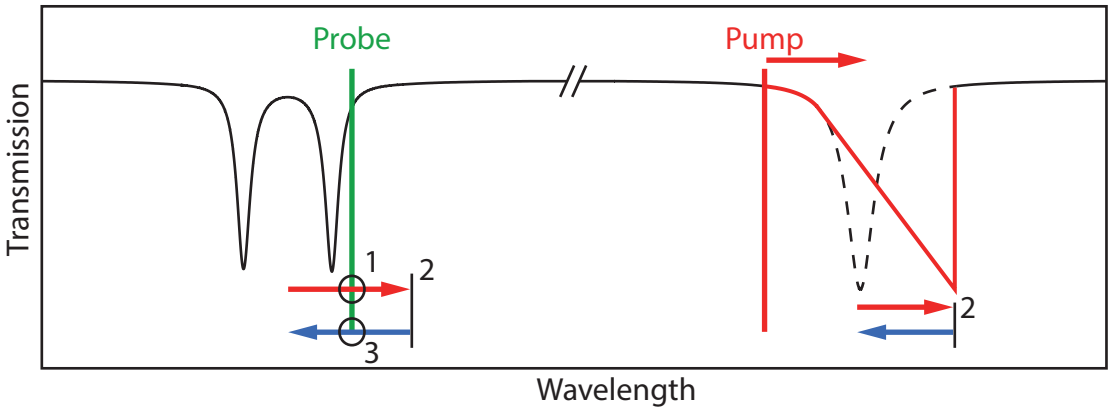

Figure 5.23: **Scheme for thermal lifetime measurement.** A pump laser sweeps over one resonance, while a static probe laser probes another resonance as it passes by it as a result of the thermo-optical effect. The probe laser transmission changes when the probe resonance red-shifts (1) while the cavity heats up and, after reaching maximum shift (2), blue-shifts (3) while the cavity cools down. Figure adapted from reference 146.

This process results in a given time between (2) and (3) and, by knowing the distance in frequency between the probe laser and the maximum red-shift of the probe resonance, it is possible to determine the time-dependency of the resonance, which reflects the thermal lifetime of the cavity. In our case, the resonances have two peaks distant by a known frequency, hence it is easier to write the speed of frequency shift during cool-down when the two peaks cross the probe laser frequency.

Repeating this process for different relative positions between probe laser and probe resonance, it is possible to plot the shift speed versus time (from (2) to (3)) and, by fitting a decaying exponential ($e^{-t/\tau_{th}}$), obtain the thermal lifetime of the samples. Figure 5.24 shows an example of the data obtained for one position of the probe laser, with events (1), (2) and (3) identified. The time axis was shifted such that $t = 0$ is the time when maximum shift happens (event (2)). Because the pump is high enough to cause self-pulsing, a low-pass filter was applied (in post-processing) to the traces in fig. 5.24a for clarity. In figure 5.24b no filter was applied to any of the traces, resulting in the larger noise before the maximum shift time (t_2).

Performing this procedure for both double and single cavity systems, using $t_3 - t_2$ as

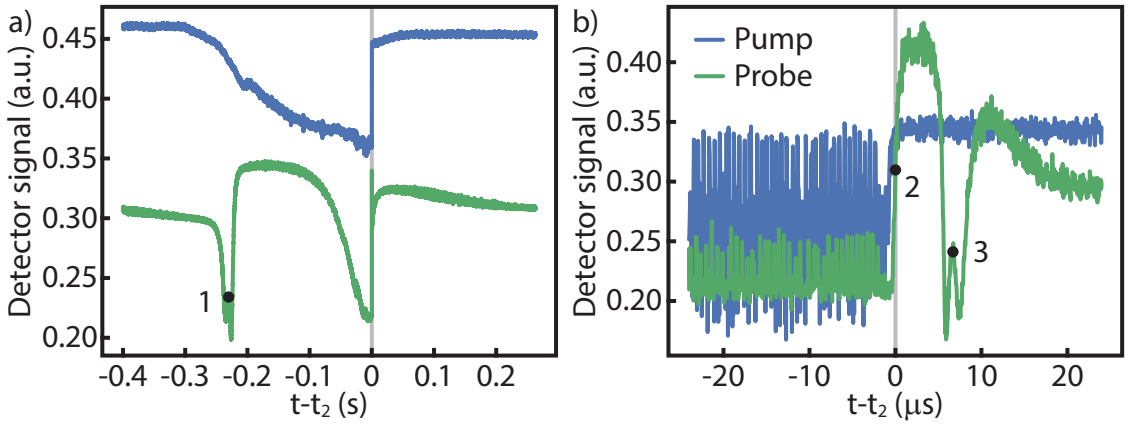

Figure 5.24: **Data obtained for the thermal lifetime determination.** a) Pump (blue) and probe (green) showing the whole sweep over the pump resonance. (1) marks the position when the probe resonance passed by the probe laser position for the first time. The two traces were filtered to remove the oscillations signal for better clarity. b) Zoom in the time when the maximum pump shift occurs (t_2). (2) marks the reference maximum pump shift time and (3) the moment when the probe resonance passes by the probe laser position for the second time. No filter was applied in these traces, hence the noise before t_2 due to self-pulsing of the pump resonance. Both probe trace was displaced upwards for better comparison with the pump trace.

the instant of shift speed evaluation, where t_3 is defined as the average time between probe peaks during cool-down. Repeating it for different detunings between probe laser and probe resonance a time dependent frequency shift speed data set is produced. Figure 5.25 shows the resulting data for both single (a) and double (b) cavity systems, together with the fitted curves. The resulting thermal life-times are $\tau_{th} = 2.98 \pm 0.55$ µs for the single cavity and $\tau_{th} = 2.00 \pm 0.24$ µs for the double cavity, with the error given by the standard error of the fit. The single cavity value is much smaller than the used in the numerical model, while the value for the double cavity is only 30% smaller.

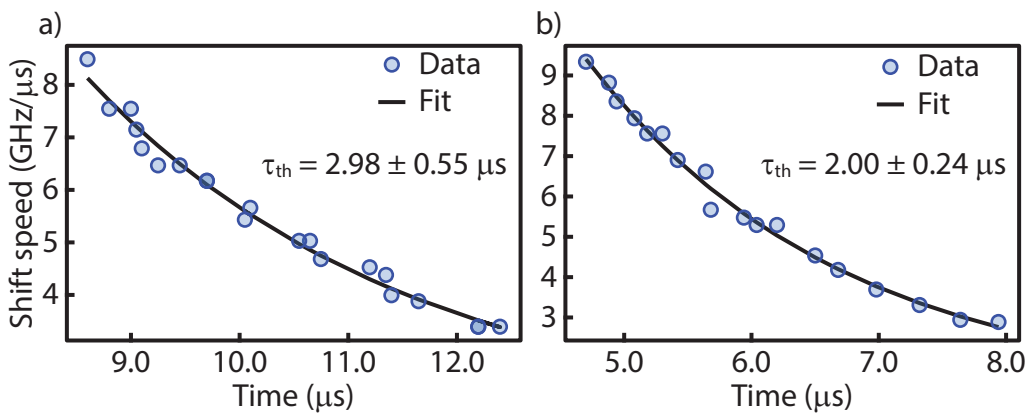

Figure 5.25: **Thermal driven exponentially decaying shift speeds.** a) Single cavity data. b) Double cavity data.

Again, these discrepancies are expected to result in variations of the quantitative numerical results, but do not have great impact on the general behavior of the solutions. Hence the qualitative comparison between model and experiments is still valid.

5.4. Experimental single cavity oscillations

The first step in our experiments was to verify if these small cavities could enter the self-pulsing regime, for what we first measured the single cavity system. The general procedure to obtain all the necessary data is to step the wavelength of the pump laser over the resonance of the cavity close to 1470 nm, with high input power. In each step, the transmitted light is measured with a photodetector whose photocurrent spectrum is obtained with an electrical spectrum analyzer (ESA) and the time-trace with an oscilloscope (OSC). The final laser wavelength position is determined by the amount of non-linear shift suffered by the resonance due to the pump power, typically on the order of a few nanometers from the cold cavity resonance.

For pump powers as low as 200 µW the single cavity already presents the signatures of self-pulsing, but to obtain the high-bandwidth pulses, with a spectrum spanning several hundreds of MHz, 360 µW is injected into the taper, resulting in an estimated cavity input power of 310 µW (taking the taper loss into account). This typically causes a non-linear shift of approximately 4 nm in the resonance and produces the spectrogram presented in figure 5.26. To produce this spectrogram the laser wavelength step was of 50 pm. In this spectrogram it is possible to observe the sharp start of the oscillations and the shift of the first harmonic with wavelength, in the same manner as presented in the theoretical model.

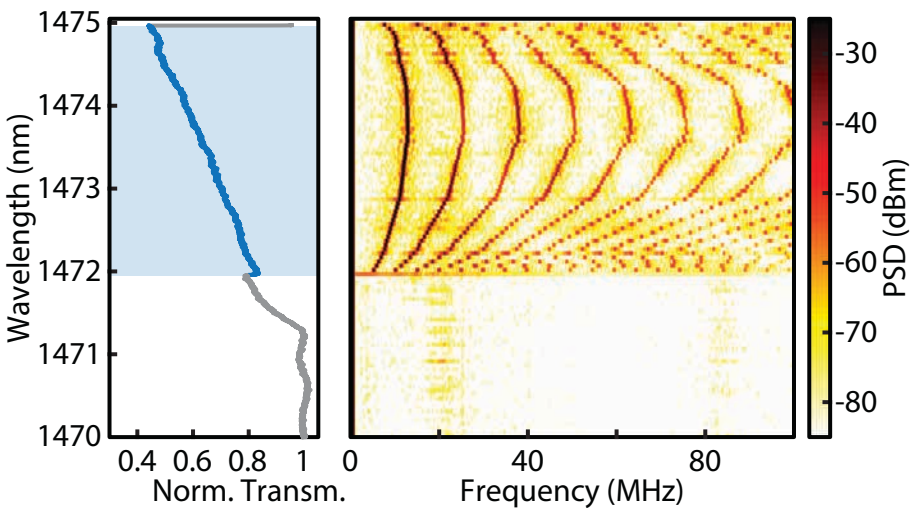

Figure 5.26: **Experimental single cavity self-pulsing spectrogram.** Left) Optical transmission along the pump resonance. The blue region indicates the wavelengths for which oscillation takes place. Right) Pump wavelength dependent spectrogram. Vertical scale follows the transmission signal on the left.

The transmission time-traces (fig. 5.27, left) reveal the behavior expected from the self-pulsing process, with a sharp dip in the beginning and a slow decay after that until the end of the pulses. It is also possible to note the variation of the pulses duty-cycle with the pump detuning, which produces the varying frequency on the spectrogram. In this case we chose to show the traces when the laser wavelength is set to 1472.5 nm (top) and to 1474.5 nm (bottom).

We can also take the discrete time-derivative of these traces and obtain the phase-space diagram (fig. 5.27,right), which is very well reproduced by the theoretical mode. Due to the intrinsic noise of the measurements a low pass filter (post-processing) was used in the data, reducing the noise in the phase-space diagram; also, these diagrams are constructed with several cycles of the pulses, for clearer definition of the closed path. The time-traces are always shown close to zero because the RF output of the photodetector gives only the AC component of the photocurrent, filtering the DC component up to 40 kHz (see NewFocus 1617-AC user's guide).

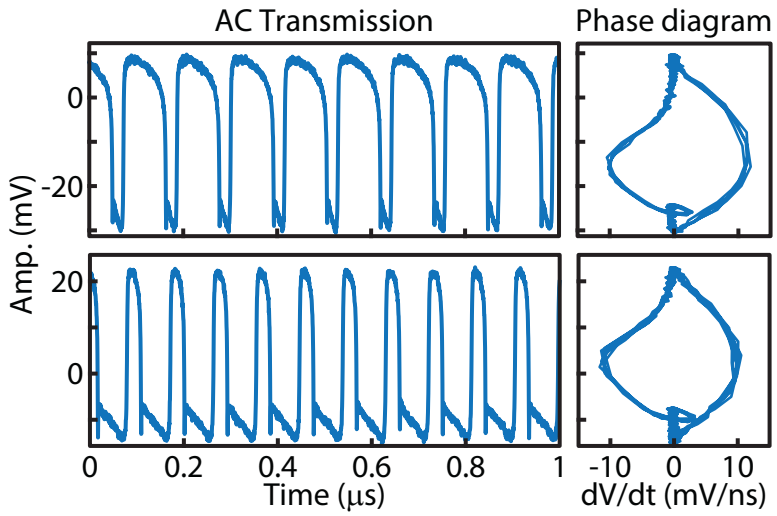

Figure 5.27: **Experimental single cavity self-pulsing time-traces.** Time-traces of the transmitted laser (left) and their respective phase diagram (right). The top set is taken when the pump laser wavelength is set to 1472.5 nm, while the bottom set is for a wavelength of 1474.5 nm. The vertical scales of the phase-diagrams match those of the time-traces on their left.

I also tested the possibility of injection-locking these oscillations with an external amplitude modulation of the pump laser. For that the pump laser passes through an electro-optic amplitude modulator driven by a sinusoidal electrical drive with output power of -10 dBm (100 μW), which gives an optical power modulation depth of only 8%, for our modulator whose V_π (voltage for a π change in the optical field phase) is 4 V. The modulation frequency is fixed at 80 MHz, which in this case corresponds the 16th harmonic of the pulses at the beginning of the oscillations. The laser wavelength is then swept (not stepped) with a cavity input power set to 310 μW, producing the spectrogram shown in figure 5.28. The vertical timescale is time instead of wavelength because this measurement was made without synchronizing the laser sweep to the spectrogram acquisition.

Despite the very small modulation amplitude, the FC-TO frequency is locked to the modulation tone at certain regions, characterizing the locking of the oscillations by the modulation. Moreover, the locking occurs for many harmonics, from the 16th to the 7th in this case. This result implies that one should be able to couple two pulsing cavities even if their first harmonic don't match, which gives freedom for the two oscillating systems to be designed separately in terms of the pulse characteristics.

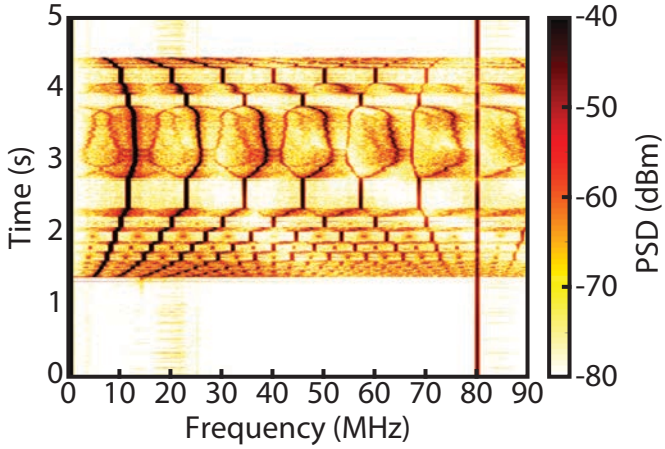

Figure 5.28: Spectrogram of FC-TO oscillations with RF modulation tone sweeping frequency (dashed line).

This ability to lock an oscillator to a low noise external source is of great interest because it can be used to reduce the phase-noise of the main oscillator, which is related to the stability of the oscillators frequency [147]. To address the phase-noise reduction of the self-pulsing process we measured the phase-noise of the first harmonic of the pulses while the oscillations are locked at different harmonics (fig. 5.29). For that we used the phase-noise application of the ESA, which measures the phase-noise through what is called direct measurement, i.e., it measures the amount of noise in a 1 Hz window centered at a given distance from the carrier frequency. Because the modulation signal has much less phase-noise than the pulses, we observe a significant reduction of the phase noise up to 100 kHz from the carrier (>40 dBc at 10 kHz), even locking just in the first harmonic. Further reduction of phase-noise when locking through higher order harmonics is also observed. Further investigation is needed to determine the origins of the peaks in the locked phase-noise curves, which could be due to external sources, such as the electronics used to obtain the data.

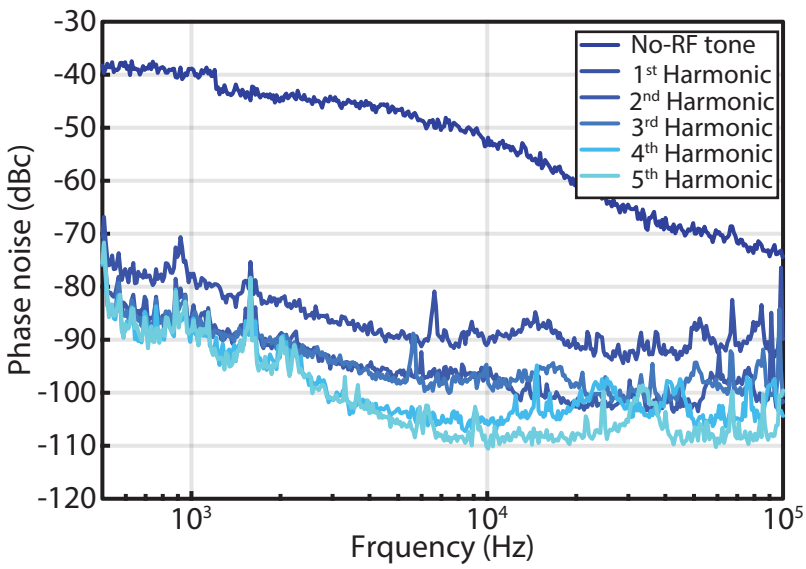

Figure 5.29: **Phase noise of self-pulsing for different harmonics locking.**

According to Agilent's (now Keysight) Phase-noise Measurement Solutions guide, this method should be considered only as a quick way to obtain the phase-noise of a locked oscillator, and not as reliable source of phase-noise information. Also, the documentation (as well as Enrico Rubiola [147]) states that direct phase-noise measurement performed by ESA's suffer from limitations related to the ability to separate amplitude- from phase-noise and the dynamical range of the equipment. Nevertheless, the measurements presented here show such a significant reduction in noise due to the locking of the self-pulsing, even though the modulation is relatively weak, that this alone justifies the interest in studying the system presented here.

5.5. Experimental double cavity oscillations

The two cavity system was measured following the same procedure detailed in the last section, stepping the laser wavelength across the resonances around 1472 nm with power enough to observe the self-pulsing of the transmitted light. In this case, because the optical mode volume increases due to the two cavities, the input power required to attain self-pulsing also increases as the phenomenon depends on the energy density to occur. The measurements presented here were performed with 2.4 mW of taper input power, which results in an estimated cavity input power of 2.0 mW when the taper loss is accounted for.

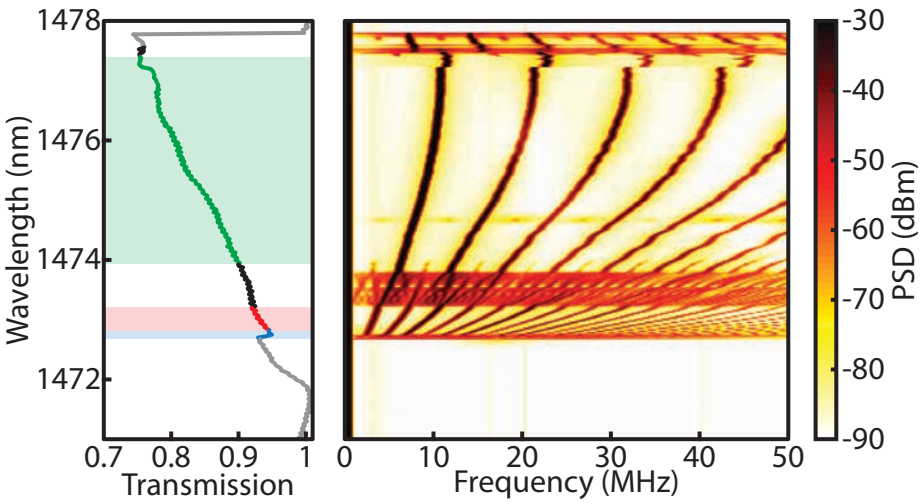

Figure 5.30: **Experimental double cavity self-pulsing spectrogram.** Left) Optical transmission along the pump resonance. The colored regions indicate the wavelengths for which oscillation takes place, marking the different operation regions of interest. Right) Pump wavelength dependent spectrogram. Vertical scale follows the transmission signal on the left.

The resulting spectrogram of this process is shown in figure 5.30, in which it is possible to note the transition regions present in the theoretical model. Note that on the red region there are more spectral peaks than in the green region, which was not clear on the numerical spectrogram due to the larger detuning step used there. Also, some of the spectral peaks seem to follow a continuous path passing by the region between red and green, while some of the

harmonics seem to vanish after this transition region. This could be a confirmation of the hypothesis that, in the red region of the spectrogram, the pulses of the two cavities lock through different harmonics, i.e., at different frequencies, while in the green region they are locked at the first harmonic, i.e., at the same frequency.

Again, the transmission time-traces are obtained together with the spectra, and three examples matching three different regions (matching colors) of the spectrogram are presented in figure 5.31, as well as their respective phase diagrams. The three traces were taken with the laser wavelength set to 1472.7 nm (blue), 1473.05 nm (red) and 1475.5 nm (green). These three examples match very well the three operation conditions presented in the theoretical model, namely the pulses dominated by a single cavity (blue), the two amplitude pulses (red) and the single pulses with a second broader dip. Even the detail of the small oscillations before the pulse for the blue trace is visible, despite the noisy background. Then, comparing these data with the model, it is possible to state that the two cavities have their oscillations locked to each other exclusively by sharing the same optical field, in all of these situations.

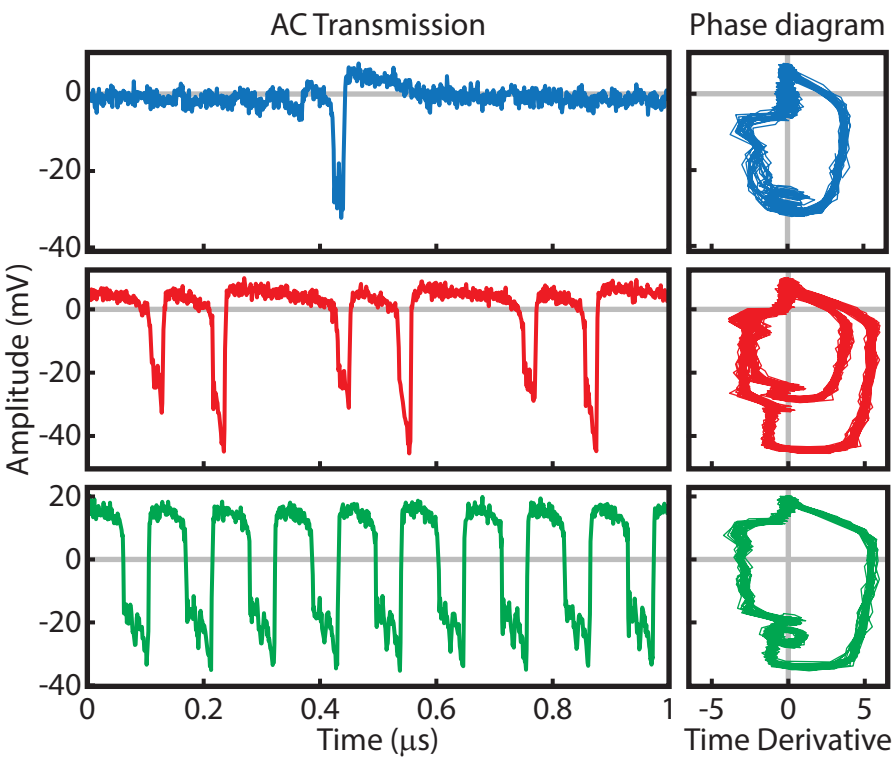

Figure 5.31: **Experimental double cavity synchronized self-pulsing time-traces.** These are the time-traces of the transmitted laser (left) and their respective phase diagram (right). The top (blue) set is taken when the pump laser wavelength is set to 1472.7 nm, the middle (red) set is for a wavelength of 1473.05 nm and the bottom (green) for a wavelength of 1475.5 nm, with the colors matching the regions marked in fig. 5.30. The vertical scales of the phase-diagrams match those of the time-traces on their left.

Finally looking at the transmission time-trace of one of the regions marked in black in fig. 5.30, more precisely for the laser wavelength set to 1477.775 nm, we observe the trace shown in figure 5.32, where it is clear from both time-trace and phase-diagram that there are

two cavities oscillating in an asynchronous fashion, causing random-like pulses, filling a larger area in the phase-space and presenting noisier spectra. This indicates that the coupling of the oscillations through the optical field is strong enough to guarantee a broad range of synchronous operation, but not enough to completely avoid asynchronous operation.

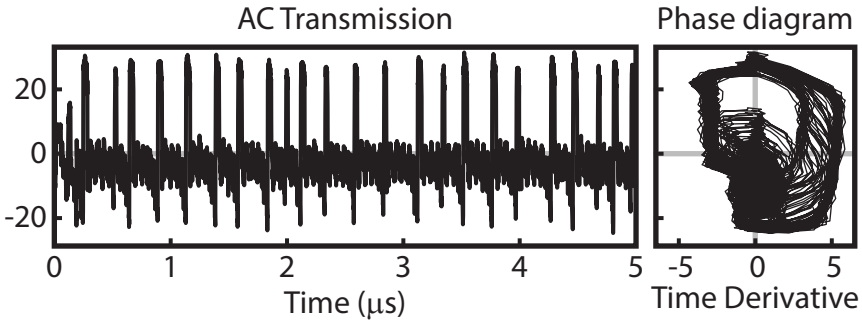

Figure 5.32: **Experimental double cavity asyncrhonous self-pulsing time-trace.** Time-trace of the transmitted laser (left) and its respective phase diagram (right). The pump laser wavelength is set to 1477.775 nm, with the color matching one of the regions marked in fig. 5.30. The vertical scale of the phase-diagram matches that of the time-trace on the left.

5.6. Conclusion

In conclusion, although the self-pulsing in silicon optical micro-cavities may impair the operation of optomechanical devices, they can be of interest for the silicon photonics community. That is because this oscillations can be easily tailored [48, 49] by controlling the geometry of the devices, which primarily changes the thermal lifetime, or the FC lifetime [138]. Also, these oscillations can be easily locked to very weak reference signals, as shown in section 5.4, even for higher harmonics, allowing for great reduction of the phase-noise of the pulses. In fact it has been already demonstrated that these pulses can be locked also to optical modulations due to the optomechanical interaction optomechanical [50, 51], paving the way to an even more versatile systems and devices.

Chapter 6

Conclusions and perspectives

6.1. Conclusions

In this thesis we studied two different topics that are of interest for the advancement of optomechanical devices. In the first work we used a near-field optomechanical (NFO) system to decouple optical and mechanical designs. This allowed for the study of the mechanical component of a near-field optomechanical device, without any concerns to the optical cavity. The mechanical resonators are composed by a double-paddle mechanical device coupled to the optical field of a micro-disk cavity through the evanescent field of the latter. This mechanical design suppresses anchor losses through the destructive interference of elastic waves. With this it was possible to demonstrate high mechanical Q-factors, for a device with resonant modes close to 55 MHz, limited by material and surface damping mechanisms.

Comparison of analytical and numerical models to the experimental results showed that the Akhiezer effect is the most likely material mechanism to limit the device operation at room temperature, together with surface mechanisms. The latter was demonstrated to be important at all temperatures, ranging from room (293 K) down to cryogenic (22 K) conditions, by submitting the devices to treatments that are known to improve the surface properties of silicon devices, leading to increased Q-factors. Part of this work was presented at the ENFMC Brazilian Physical Society Meeting of 2015, in which it received an award as "The best poster on the optics and photonics area". The final results were presented at the Conference on Lasers and Electro-Optics®of 2016 (CLEO 2016) [52] and a complete paper is currently under revision, but a preprint version can be found in arXiv [53].

Although we could demonstrate the effectiveness of anchor loss suppression in the optomechanical devices, we could not demonstrate self-oscillations at room temperature. That is because the input power threshold to attain such regime was higher than the power needed to start the self-pulsing process. This phenomenon is known to take place in silicon optical micro-cavities and, as exemplified in this thesis, can impair the operation of silicon based optomechanical oscillators. This brought me to the second topic of our work, which was the study of self-pulsing in silicon micro-cavities.

More specifically, we demonstrated that it is possible to lock the pulses of a single cavity to a weak modulation tone of the pump laser. Also, the locking can occur by matching the modulation frequency to various harmonics of the pulses, leading to reduction of the phase-noise in the first harmonic. Moreover, we theoretically and experimentally demonstrated that

these pulses, when occurring in a pair of optically coupled cavities, can effectively synchronize, similarly to what was demonstrated for an optomechanical system [12]. This work was presented as a poster at the CLEO 2017 [148] and a paper is currently under preparation.

6.2. Perspectives

The NFO devices are expected to produce very high quality oscillators that can be part of more complex systems, such as optomechanical arrays [15]. In fact, the samples in which the devices presented here are fabricated also include a series of devices composed by a single optical cavity with several similar mechanical resonators coupled to it, as shown in figure 6.1. These devices are expected to couple all mechanical resonators to each other with the optical field as the only mediator of this interaction.

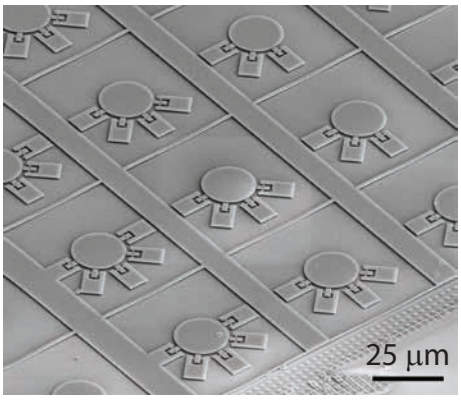

Figure 6.1: **SEM image of an array of double paddles NFO device.**

Given the results of our work we expect these array devices to work but only for low temperature, when the mechanical Q-factor increases, reducing the power threshold for optomechanical self-oscillations. And, because silicon thermal properties greatly change at low temperatures, reducing the sample temperature will greatly decrease the thermal life-time of the devices, which could eliminate the problem of self-pulsing before the device enters in the optomechanical self-oscillation regime [48].

As for the coupled cavities' self-pulsing work, it should follow first the natural path of testing an increasing number of coupled cavities, again similarly to the optomechanical counter-part [13]. An advantage of the self-pulsing to the optomechanical approach is that in the former the oscillations can couple through different harmonics. This means that even for systems with great differences in cavity dimensions, which can lead to different pulse periods, the pulses can still synchronize, relieving a constrain on fabrication.

However, there is still an issue to obtain coupled optical cavities, which can be difficult as minor unavoidable fluctuations in the fabrication process can render cavities whose resonant frequencies are far enough for them to be practically decoupled. And this problem scales quickly with the number of coupled cavities. But we observe that the non-linear shift

of the resonances due to the thermo-optical effect can be used to compensate for that. In the case of silicon this shift is always in the direction of reducing the resonant frequency, hence one could pump the system through the bluest (highest frequency) coupled resonance, which will insert more energy on the cavity with the bluest individual resonance. This will cause this cavity's resonance to red-shift more than the others, bringing it closer to their resonances and then dividing the total energy more evenly.

Of course this workaround for the resonance mismatch has a limitation, because when the energy is more evenly distributed between the cavities the amount of energy in the first one drops, which reduces the total shift suffered by its resonance. Hence, if the frequency mismatch is too large, the system can return to a decoupled state because the total energy in each cavity is not enough to maintain the necessary shift to correct for the mismatch.

Lastly, we recall that it has been demonstrated that the self-pulsing of the cavities can actually couple to the optomechanical oscillations [50]. This means that the devices presented in this thesis can become a good platform to study systems in which mechanical, carriers and heat dynamics are coupled through the optical field. And again, the capability of the self-pulsing being locked at any harmonic makes it very easy to attain such a regime, specially because its period is strongly dependent on pump detuning, and the same goes for the optomechanical oscillations due to the optical spring effect.

Bibliography

1. Braginski, V., Manukin, A. Ponderomotive effects of electromagnetic radiation. *Sov. Phys. JETP* **25**(4), 653–655 (1967). 17

2. Cuthbertson, B. D., Tobar, M. E., Ivanov, E. N., Blair, D. G. Parametric back-action effects in a high-Q cyrogenic sapphire transducer. *Review of Scientific Instruments* **67**(7), 2435 (1996).

3. Dorsel, A., McCullen, J., Meystre, P., Vignes, E., Walther, H. Optical Bistability and Mirror Confinement Induced by Radiation Pressure. *Physical Review Letters* **51**(17), 1550–1553 (1983). 17

4. Abbott, B. P., *et al.* Observation of Gravitational Waves from a Binary Black Hole Merger. *Physical Review Letters* **116**(6), 061102 (2016). 17

5. Sun, X., Zheng, J., Poot, M., Wong, C. W., Tang, H. X. Femtogram Doubly Clamped Nanomechanical Resonators Embedded in a High- Q Two-Dimensional Photonic Crystal Nanocavity. *Nano Letters* **12**(5), 2299–2305 (2012). 17, 51

6. Davis, J. P., Vick, D., Fortin, D. C., Burgess, J. A. J., Hiebert, W. K., Freeman, M. R. Nanotorsional resonator torque magnetometry. *Applied Physics Letters* **96**(7), 072513 (2010). 17

7. Tsaturyan, Y., Barg, A., Polzik, E. S., Schliesser, A. Ultracoherent nanomechanical resonators via soft clamping and dissipation dilution. *Nature Nanotechnology* (2017). 17, 20

8. Chan, J., Alegre, T. P. M., Safavi-Naeini, A. H., Hill, J. T., Krause, A., Gröblacher, S., Aspelmeyer, M., Painter, O. Laser cooling of a nanomechanical oscillator into its quantum ground state. *Nature* **478**(7367), 89–92 (2011). 17, 48

9. Teufel, J. D., Donner, T., Li, D., Harlow, J. W., Allman, M. S., Cicak, K., Sirois, A. J., Whittaker, J. D., Lehnert, K. W., Simmonds, R. W. Sideband cooling of micromechanical motion to the quantum ground state. *Nature* **475**(7356), 359–63 (2011). 17

10. Grudinin, I. S., Lee, H., Painter, O., Vahala, K. J. Phonon Laser Action in a Tunable Two-Level System. *Physical Review Letters* **104**(8), 083901 (2010). 17, 18

11. Deotare, P. B., Bulu, I., Frank, I. W., Quan, Q., Zhang, Y., Ilic, R., Loncar, M. All optical reconfiguration of optomechanical filters. *Nature Communications* **3**, 846 (2012). 17

12. Zhang, M., Wiederhecker, G. S., Manipatruni, S., Barnard, A., McEuen, P., Lipson, M. Synchronization of Micromechanical Oscillators Using Light. *Physical Review Letters* **109**(23), 233906 (2012). 17, 18, 22, 48, 61, 87, 100

13. Zhang, M., Shah, S., Cardenas, J., Lipson, M. Synchronization and Phase Noise Reduction in Micromechanical Oscillator Arrays Coupled through Light. *Physical Review Letters* **115**(16), 163902 (2015). 17, 48, 87, 100

14. Heinrich, G., Ludwig, M., Qian, J., Kubala, B., Marquardt, F. Collective Dynamics in Optomechanical Arrays. *Physical Review Letters* **107**(4), 43603 (2011). 18

15. Peano, V., Brendel, C., Schmidt, M., Marquardt, F. Topological Phases of Sound and Light. *Physical Review X* **5**(3), 031011 (2015). 18, 100

16. Brendel, C., Peano, V., Painter, O. J., Marquardt, F. Pseudomagnetic fields for sound at the nanoscale. *Proceedings of the National Academy of Sciences* **114**(17), E3390–E3395 (2017). 18

17. Brendel, C., Peano, V., Painter, O., Marquardt, F. Snowflake Topological Insulator for Sound Waves (2017). 18

18. Righini, G., Dumeige, Y., Féron, P. Whispering gallery mode microresonators: fundamentals and applications. *Rivista del Nuovo Cimento* **34**(7), 435–488 (2011). 18, 59

19. Joannopoulos, J. D., Johnson, S. G., Winn, J. N., Meade, R. D. *Photonic Crystals : Molding the Flow of Light (Second Edition).* Princeton University Press (2008). 18

20. Santos, F. G. S., Espinel, Y. A. V., Luiz, G. O., Benevides, R. S., Wiederhecker, G. S., Mayer Alegre, T. P. Hybrid confinement of optical and mechanical modes in a bullseye optomechanical resonator. *Optics Express* **25**(2), 508 (2017). 19, 20, 27, 29

21. Benevides, R., Santos, F. G. S., Luiz, G. O., Wiederhecker, G. S., Alegre, T. P. M. Ultrahigh-Q optomechanical crystal cavities fabricated in a CMOS foundry. *Scientific Reports* **7**(1), 2491 (2017). 19, 20, 24, 29, 61

22. Johnson, S. G., Ibanescu, M., Skorobogatiy, M. A., Weisberg, O., Joannopoulos, J. D., Fink, Y. Perturbation theory for Maxwell's equations with shifting material boundaries. *Physical Review E* **65**(6), 066611 (2002). 19, 58, 122

23. Chan, J., Safavi-Naeini, A. H., Hill, J. T., Meenehan, S., Painter, O. Optimized optomechanical crystal cavity with acoustic radiation shield. *Applied Physics Letters* **101**(8), 081115 (2012). 19, 58, 61

24. Florez, O., Jarschel, P. F., Espinel, Y. A. V., Cordeiro, C. M. B., Mayer Alegre, T. P., Wiederhecker, G. S., Dainese, P. Brillouin scattering self-cancellation. *Nature Communications* **7**, 11759 (2016). 19

25. Dainese, P., Russell, P. S. J., Joly, N., Knight, J. C., Wiederhecker, G. S., Fragnito, H. L., Laude, V., Khelif, A. Stimulated Brillouin scattering from multi-GHz-guided acoustic phonons in nanostructured photonic crystal fibres. *Nature Physics* **2**(6), 388–392 (2006). 19

26. Dainese, P., Russell, P. S., Wiederhecker, G. S., Joly, N., Fragnito, H. L., Laude, V., Khelif, A. Raman-like light scattering from acoustic phonons in photonic crystal fiber. *Optics Express* **14**(9), 4141 (2006).

27. Safavi-Naeini, A. H., Painter, O. Design of optomechanical cavities and waveguides on a simultaneous bandgap phononic-photonic crystal slab. *Opt. Express* **18**(14), 14926–14943 (2010). 19

28. Anetsberger, G., Arcizet, O., Unterreithmeier, Q. P., Rivière, R., Schliesser, A., Weig, E. M., Kotthaus, J. P., Kippenberg, T. J. Near-field cavity optomechanics with nanomechanical oscillators. *Nature Physics* **5**(12), 909–914 (2009). 19, 49, 58

29. Haus, H. A. *Waves and fields in optoelectronics*. Solid state physical electronics series. Prentice-Hall, Englewood Cliffs, NJ (1984). 20, 30, 116

30. Cleland, A. N. *Foundations of Nanomechanics*. Advanced Texts in Physics. Springer Berlin Heidelberg, Berlin, Heidelberg (2003). 20, 52, 53, 56

31. Aspelmeyer, M., Kippenberg, T. J., Marquardt, F. Cavity optomechanics. *Reviews of Modern Physics* **86**(4), 1391–1452 (2014). 20, 40, 42, 45, 46, 48, 58, 61, 116

32. Chandorkar, S. A., Agarwal, M., Melamud, R., Candler, R. N., Goodson, K. E., Kenny, T. W. Limits of quality factor in bulk-mode micromechanical resonators. In *2008 IEEE 21st International Conference on Micro Electro Mechanical Systems*, pages 74–77. IEEE (2008). 20

33. Liu, X., Vignola, J. F., Simpson, H. J., Lemon, B. R., Houston, B. H., Photiadis, D. M. A loss mechanism study of a very high Q silicon micromechanical oscillator. *Journal of Applied Physics* **97**(2), 023524 (2005). 20

34. Armani, D. K., Kippenberg, T. J., Spillane, S. M., Vahala, K. J. Ultra-high-Q toroid microcavity on a chip. *Nature* **421**(6926), 925–928 (2003). 20

35. Nguyen, D. T., Baker, C., Hease, W., Sejil, S., Senellart, P., Lemaître, A., Ducci, S., Leo, G., Favero, I. Ultrahigh Q-frequency product for optomechanical disk resonators with a mechanical shield (2013). 20

36. Imboden, M., Mohanty, P. Dissipation in nanoelectromechanical systems. *Physics Reports* **534**(3), 89–146 (2014). 52

37. Joshi, S., Hung, S., Vengallatore, S. Design strategies for controlling damping in micromechanical and nanomechanical resonators. *EPJ Techniques and Instrumentation* **1**(1), 5 (2014).

38. Zhang, M., Luiz, G., Shah, S., Wiederhecker, G., Lipson, M. Eliminating anchor loss in optomechanical resonators using elastic wave interference. *Applied Physics Letters* **105**(5), 051904 (2014). 20, 51

39. Fedorov, S. A., Sudhir, V., Schilling, R., Schütz, H., Wilson, D. J., Kippenberg, T. J. Evidence for structural damping in a high-stress silicon nitride nanobeam and its implications for quantum optomechanics (2017). 20

40. Lee, J. E.-Y., Yan, J., Seshia, A. A. Anchor limited Q in flexural mode resonators. In *2008 IEEE Ultrasonics Symposium*, pages 2213–2216. IEEE (2008). 20

41. Wilson-Rae, I. Intrinsic dissipation in nanomechanical resonators due to phonon tunneling. *Physical Review B* **77**(24), 245418 (2008).

42. Cole, G. D., Wilson-Rae, I., Werbach, K., Vanner, M. R., Aspelmeyer, M. Phonon-tunnelling dissipation in mechanical resonators. *Nature communications* **2**, 231 (2011). 20

43. Alegre, T., Safavi-Naeini, A. Quasi-two-dimensional optomechanical crystals with a complete phononic bandgap. *Optics Express* **19**(6), 5658–5669 (2010). 20, 56

44. Pandey, M., Reichenbach, R., Zehnder, A., Lal, A., Craighead, H. Reducing Anchor Loss in MEMS Resonators Using Mesa Isolation. *Journal of Microelectromechanical Systems* **18**(4), 836–844 (2009). 20

45. Zhang, R., Ti, C., Davanço, M. I., Ren, Y., Aksyuk, V., Liu, Y., Srinivasan, K. Integrated tuning fork nanocavity optomechanical transducers with high fMQM product and stress-engineered frequency tuning. *Applied Physics Letters* **107**(13), 131110 (2015). 20, 51

46. Dinu, M., Quochi, F., Garcia, H. Third-order nonlinearities in silicon at telecom wavelengths. *Applied Physics Letters* **82**(18), 2954–2956 (2003). 21, 70

47. Borselli, M., Johnson, T. J., Painter, O. Accurate measurement of scattering and absorption loss in microphotonic devices. *Optics Letters* **32**(20), 2954 (2007). 21, 74, 75

48. Van Vaerenbergh, T., Fiers, M., Dambre, J., Bienstman, P. Simplified description of self-pulsation and excitability by thermal and free-carrier effects in semiconductor microcavities. *Physical Review A* **86**(6), 063808 (2012). 21, 69, 71, 98, 100

49. Abrams, D. M., Slawik, A., Srinivasan, K. Nonlinear Oscillations and Bifurcations in Silicon Photonic Microresonators. *Physical Review Letters* **112**(12), 123901 (2014). 21, 69, 71, 98

50. Navarro-Urrios, D., Capuj, N. E., Gomis-Bresco, J., Alzina, F., Pitanti, A., Griol, A., Martínez, A., Sotomayor Torres, C. M. A self-stabilized coherent phonon source driven by optical forces. *Scientific Reports* **5**, 15733 (2015). 21, 69, 98, 101

51. Navarro-Urrios, D., Capuj, N. E., Colombano, M. F., García, P. D., Sledzinska, M., Alzina, F., Griol, A., Martínez, A., Sotomayor-Torres, C. M. Nonlinear dynamics and chaos in an optomechanical beam. *Nature Communications* **8**, 14965 (2017). 21, 69, 98

52. de Oliveira Luiz, G., Santos, F. G., da Silva Benevides, R., Espinel, Y., Alegre, T. P., Wiederhecker, G. Material limited high-Q mechanical paddle-resonator. In *Conference on Lasers and Electro-Optics*, page STu4E.2. OSA, Washington, D.C. (2016). 22, 99

53. Luiz, G. O., Santos, F. G. S., Benevides, R. S., Espinel, Y. A. V., Alegre, T. P. M., Wiederhecker, G. S. Efficient anchor loss suppression in coupled near-field optomechanical resonators. *arXiv: 1701.03321* (2017). 22, 99

54. Pikovsky, A., Rosenblum, M., Kurths, J. *Synchronization : a universal concept in nonlinear science.* Cambridge University Press, 1st ed. (2003). 22

55. Okamoto, K. *Fundamentals of Optical Waveguides*. Elsevier (2006). 25

56. Santos, F. G. S. *Cavity optomechanics in silicon disks and nanostructured disks*. Ph.D. thesis, University of Campinas (2017). 27, 41, 116

57. Borselli, M., Johnson, T. J., Painter, O. Measuring the role of surface chemistry in silicon microphotonics. *Applied Physics Letters* **88**(13), 131114 (2006). 28, 66

58. Maboudian, R. Critical Review: Adhesion in surface micromechanical structures. *Journal of Vacuum Science & Technology B: Microelectronics and Nanometer Structures* **15**(1), 1 (1997). 28

59. Vargaftik, N. B., Volkov, B. N., Voljak, L. D. International Tables of the Surface Tension of Water. *Journal of Physical and Chemical Reference Data* **12**(3), 817–820 (1983). 28

60. Vazquez, G., Alvarez, E., Navaza, J. M. Surface Tension of Alcohol Water + Water from 20 to 50 .degree.C. *Journal of Chemical & Engineering Data* **40**(3), 611–614 (1995). 28

61. da Silva Benevides, R., de Oliveira Luiz, G., Santos, F. G., Wiederhecker, G., Alegre, T. P. Optomechanical Oscillators Fabricated in a CMOS-compatible Foundry. In *Conference on Lasers and Electro-Optics*, page JTh2A.99. OSA, Washington, D.C. (2016). 29

62. Santos, F. G., Espinel, Y., de Oliveira Luiz, G., da Silva Benevides, R., Wiederhecker, G., Alegre, T. P. Bullseye Optomechanical Resonator. In *Conference on Lasers and Electro-Optics*, page STu4E.4. OSA, Washington, D.C. (2016).

63. Benevides, R., Luiz, G. O., Santos, F. G., Wiederhecker, G. S., Alegre, T. Optomechanical Crystals Fabricated by a CMOS Foundry. In *Frontiers in Optics 2015*, page FTu5C.3. OSA, Washington, D.C. (2015).

64. Santos, F. G., Espinel, Y., Luiz, G., Princepe, D., Wiederhecker, G., Alegre, T. Multi-Ghz Bullseye Optomechanical Cavity. In *Latin America Optics and Photonics Conference*, page LM3C.5. OSA, Washington, D.C. (2014). 29

65. Birks, T., Li, Y. The shape of fiber tapers. *Journal of Lightwave Technology* **10**(4), 432–438 (1992). 29, 30, 129

66. Hauer, B. D., Kim, P. H., Doolin, C., MacDonald, A. J., Ramp, H., Davis, J. P. On-chip cavity optomechanical coupling. *EPJ Techniques and Instrumentation* **1**(1), 4 (2014). 29

67. Spillane, S. S., Kippenberg, T. T., Painter, O. O., Vahala, K. K. Ideality in a Fiber-Taper-Coupled Microresonator System for Application to Cavity Quantum Electrodynamics. *Physical Review Letters* **91**(4), 043902 (2003). 30

68. Knight, J. C. J. C., Cheung, G., Jacques, F., Birks, T. A. T. A. Phase-matched excitation of whispering-gallery-mode resonances by a fiber taper. *Optics Letters* **22**(15), 1129 (1997). 30

69. Gorodetsky, M. L., Pryamikov, A. D., Ilchenko, V. S. Rayleigh scattering in high-Q microspheres. *Journal of the Optical Society of America B* **17**(6), 1051 (2000). 31, 76

70. Little, B. E., Laine, J.-P., Chu, S. T. Surface-roughness-induced contradirectional coupling in ring and disk resonators. *Optics Letters* **22**(1), 4 (1997). 31, 49, 69, 76

71. Shu, F.-J., Zou, C.-L., Özdemir, a. K., Yang, L., Guo, G.-C. Transient microcavity sensor. *Optics Express* **23**(23), 30067 (2015). 33

72. Gilbert, S. L., Swann, W. C. Acetylene 12C2H2 Absorption Reference for 1510 nm to 1540 nm Wavelength Calibration SRM 2517a. *Special Publication (NIST SP) - 260-133* (2001). 33

73. Breguet, J.-M., Pernette, E., Clavel, R. Stick and slip actuators and parallel architectures dedicated to microrobotics. In A. Sulzmann, ed., *Microrobotics: Components and Applications*, pages 13–24. International Society for Optics and Photonics (1996). 39

74. Gorodetsky, M. L., Schliesser, A., Anetsberger, G., Deleglise, S., Kippenberg, T. J. Determination of the vacuum optomechanical coupling rate using frequency noise calibration. *Optics Express* **18**(22), 23236 (2010). 40, 41, 43, 45, 46

75. Braginsky, V., Strigin, S., Vyatchanin, S. Parametric oscillatory instability in Fabry–Perot interferometer. *Physics Letters A* **287**(5-6), 331–338 (2001). 42, 61

76. Braginsky, V., Vyatchanin, S. Low quantum noise tranquilizer for Fabry–Perot interferometer. *Physics Letters A* **293**(5-6), 228–234 (2002). 42, 61

77. Luiz, G. O. *Oscilação em cavidades optomecânicas*. Ph.D. thesis, Universidade Estadual de Campinas (2013). 42, 116

78. Hansch, T., Couillaud, B. Laser frequency stabilization by polarization spectroscopy of a reflecting reference cavity. *Optics Communications* **35**(3), 441–444 (1980). 42, 61

79. Agrawal, G. P. *Fiber-Optic Communication Systems*. Wiley Series in Microwave and Optical Engineering. John Wiley & Sons, Inc., New York, USA (2002). 44

80. Efron, B., Tibshirani, R. *An introduction to the bootstrap*. Chapman & Hall (1994). 45

81. Ying, L., Lai, Y.-C., Grebogi, C. Quantum manifestation of a synchronization transition in optomechanical systems. *Physical Review A* **90**(5), 053810 (2014). 48

82. Ludwig, M., Marquardt, F. Quantum Many-Body Dynamics in Optomechanical Arrays. *Physical Review Letters* **111**(7), 073603 (2013). 48

83. Liu, F., Alaie, S., Leseman, Z. C., Hossein-Zadeh, M. Sub-pg mass sensing and measurement with an optomechanical oscillator. *Optics express* **21**(17), 19555–67 (2013). 48

84. Guzmán Cervantes, F., Kumanchik, L., Pratt, J., Taylor, J. M. High sensitivity optomechanical reference accelerometer over 10 kHz. *Applied Physics Letters* **104**(22), 221111 (2014).

85. Reinhardt, C., Müller, T., Bourassa, A., Sankey, J. C. Ultralow-Noise SiN Trampoline Resonators for Sensing and Optomechanics. *Physical Review X* **6**(2), 021001 (2016).

86. Norte, R. A., Moura, J. P., Gröblacher, S. Mechanical Resonators for Quantum Optomechanics Experiments at Room Temperature. *Physical Review Letters* **116**(14), 147202 (2016). 48

87. Huang, C., Fan, J., Zhang, R., Zhu, L. Optomechanical transductions in single and coupled wheel resonators. *Optics Express* **21**(5), 6371 (2013). 48

88. Kippenberg, T., Rokhsari, H., Carmon, T., Scherer, A., Vahala, K. Analysis of Radiation-Pressure Induced Mechanical Oscillation of an Optical Microcavity. *Physical Review Letters* **95**(3), 033901 (2005). 48

89. Xia Zhang, Tang, W. Viscous air damping in laterally driven microresonators. In *Proceedings IEEE Micro Electro Mechanical Systems An Investigation of Micro Structures, Sensors, Actuators, Machines and Robotic Systems*, pages 199–204. IEEE (1994). 48

90. Cho, Y.-H., Kwak, B. M., Pisano, A. P., Howe, R. T. Slide film damping in laterally driven microstructures. *Sensors and Actuators A: Physical* **40**(1), 31–39 (1994).

91. Young-Ho Cho, Pisano, A., Howe, R. Viscous damping model for laterally oscillating microstructures. *Journal of Microelectromechanical Systems* **3**(2), 81–87 (1994). 124

92. Vemuri, S. *Behavioral Modeling of Viscous Damping in MEMS*. Ph.D. thesis, Carnegie Mellon University (2000).

93. Bao, M., Yang, H. Squeeze film air damping in MEMS. *Sensors and Actuators A: Physical* **136**(1), 3–27 (2007). 128

94. Pratap, R., Mohite, S., Pandey, A. K. Squeeze Film Effects in MEMS Devices (2012). 48, 128

95. Zienkiewicz, O. C., Taylor, R. L. R. L., Zhu, J. Z. *The Finite element method : its basis and fundamentals*. Butterworth-Heinemann, 7 ed. (2013). 49

96. Haus, H., Huang, W. Coupled-mode theory. *Proceedings of the IEEE* **79**(10), 1505–1518 (1991). 49, 70, 80, 117

97. Hasegawa, K., Shimada, T. Perfectly Matched Layer for Finite Element Analysis of Elastic Waves in Solids. *Finite Element Analysis - Applications in Mechanical Engineering* (2012). 50

98. Heiblum, M., Harris, J. Analysis of curved optical waveguides by conformal transformation. *IEEE Journal of Quantum Electronics* **11**(2), 75–83 (1975). 50

99. Newell, W. E. Miniaturization of Tuning Forks. *Science* **161**(3848), 1320–1326 (1968). 51

100. Zotov, S. A., Simon, B. R., Prikhodko, I. P., Trusov, A. A., Shkel, A. M. Quality Factor Maximization Through Dynamic Balancing of Tuning Fork Resonator. *IEEE Sensors Journal* **14**(8), 2706–2714 (2014). 51

101. Lifshitz, R., Roukes, M. L. Thermoelastic damping in micro- and nanomechanical systems. *Physical Review B* **61**(8), 5600–5609 (2000). 53, 54, 64

102. Zener, C. Internal Friction in Solids. I. Theory of Internal Friction in Reeds. *Physical Review* **52**(3), 230–235 (1937). 53

103. Zener, C. Internal Friction in Solids II. General Theory of Thermoelastic Internal Friction. *Physical Review* **53**(1), 90–99 (1938). 53

104. Akhiezer, A. On the Absorption of Sound in Solids. *Journal of Physics-USSR* **1**, 277 (1939). 55, 64

105. Ashcroft, N. W., Mermin, N. D. *Solid state physics*. Holt, Rinehart and Winston (1976). 55

106. Wei, S., Chou, M. Y. Phonon dispersions of silicon and germanium from first-principles calculations. *Physical Review B* **50**(4), 2221–2226 (1994). 55

107. Woodruff, T. O., Ehrenreich, H. Absorption of Sound in Insulators. *Physical Review* **123**(5), 1553–1559 (1961). 55, 56, 64

108. Ghaffari, S., Chandorkar, S. A., Wang, S., Ng, E. J., Ahn, C. H., Hong, V., Yang, Y., Kenny, T. W. Quantum Limit of Quality Factor in Silicon Micro and Nano Mechanical Resonators. *Scientific Reports* **3**, 3244 (2013). 55, 56, 62, 64

109. Ilisavskii, Y., Sternin, V. Lattice absorption of high-frequency sound in silicon. *SOV. PHYS. SOL. ST.* (1985). 56

110. Barrett, H. H., Holland, M. G. Critique of Current Theories of Akhieser Damping in Solids. *Physical Review B* **1**(6), 2538–2544 (1970). 56

111. Maris, H. J. Ultrasonic Attenuation in Dirty Dielectric Crystals. *Physical Review* **175**(3), 1077–1081 (1968).

112. Mason, W. P., Bateman, T. B. Ultrasonic-Wave Propagation in Pure Silicon and Germanium. *The Journal of the Acoustical Society of America* **36**(4), 644–652 (1964). 56

113. Lambade, S. D., Sahasrabudhe, G. G., Rajagopalan, S. Temperature dependence of acoustic attenuation in silicon. *Physical Review B* **51**(22), 15861–15866 (1995). 56, 64, 131

114. Philip, J., Breazeale, M. A. Third-order elastic constants and Grüneisen parameters of silicon and germanium between 3 and 300 °K. *Journal of Applied Physics* **54**(2), 752 (1983). 56, 64, 131

115. Robinson, J. T., Manolatou, C., Chen, L., Lipson, M. Ultrasmall Mode Volumes in Dielectric Optical Microcavities. *Physical Review Letters* **95**(14), 143901 (2005). 58

116. Anetsberger, G., Weig, E., Kotthaus, J., Kippenberg, T. Cavity optomechanics and cooling nanomechanical oscillators using microresonator enhanced evanescent near-field coupling. *Comptes Rendus Physique* **12**(9-10), 800–816 (2011). 61

117. Doolin, C., Kim, P. H., Hauer, B. D., MacDonald, A. J. R., Davis, J. P. Multidimensional optomechanical cantilevers for high-frequency force sensing. *New Journal of Physics* **16**(3), 035001 (2014). 62

118. Kim, P. H., Doolin, C., Hauer, B. D., MacDonald, A. J. R., Freeman, M. R., Barclay, P. E., Davis, J. P. Nanoscale torsional optomechanics. *Applied Physics Letters* **102**(5), 053102 (2013). 62

119. Xu, Q., Manipatruni, S., Schmidt, B. 12.5 Gbit/s carrier-injection-based silicon micro-ring silicon modulators. *Opt. Express* **15**(2), 430–436 (2007). 62

120. Desai, P. D. Thermodynamic Properties of Iron and Silicon. *Journal of Physical and Chemical Reference Data* **15**(3), 967 (1986). 64, 131

121. Asheghi, M., Leung, Y. K., Wong, S. S., Goodson, K. E. Phonon-boundary scattering in thin silicon layers. *Applied Physics Letters* **71**(13), 1798 (1997). 65

122. Villanueva, L. G., Schmid, S. Evidence of Surface Loss as Ubiquitous Limiting Damping Mechanism in SiN Micro- and Nanomechanical Resonators. *Physical Review Letters* **113**(22), 227201 (2014).

123. Yang, J., Ono, T., Esashi, M. Surface effects and high quality factors in ultrathin single-crystal silicon cantilevers. *Applied Physics Letters* **77**(23), 3860 (2000).

124. Yasumura, K., Stowe, T., Chow, E., Pfafman, T., Kenny, T., Stipe, B., Rugar, D. Quality factors in micron- and submicron-thick cantilevers. *Journal of Microelectromechanical Systems* **9**(1), 117–125 (2000). 65, 67

125. Aubin, K. L., Zalalutdinov, M., Reichenbach, R. B., Houston, B. H., Zehnder, A. T., Parpia, J. M., Craighead, H. G. Laser annealing for high-Q MEMS resonators. page 531. International Society for Optics and Photonics (2003). 66, 67, 68

126. Khiznichenko, L. P., Kromer, P. F., Kaipnazarov, D. K., Otenyazov, E., Yustpova, D., Zotova, L. G. The Properties of the Low-Temperature Internal Friction Peak in Silicon. *Physica Status Solidi (B)* **21**(2), 805–810 (1967). 67

127. Evoy, S., Olkhovets, A., Sekaric, L., Parpia, J. M., Craighead, H. G., Carr, D. W. Temperature-dependent internal friction in silicon nanoelectromechanical systems. *Applied Physics Letters* **77**(15), 2397–2399 (2000). 67

128. Li, W.-C., Lin, Y., Kim, B., Ren, Z., Nguyen, C. T.-C. Quality factor enhancement in micromechanical resonators at cryogenic temperatures. In *TRANSDUCERS 2009 - 2009 International Solid-State Sensors, Actuators and Microsystems Conference*, pages 1445–1448. IEEE (2009).

129. Tao, Y., Boss, J. M., Moores, B. A., Degen, C. L. Single-crystal diamond nanomechanical resonators with quality factors exceeding one million. *Nature Communications* **5** (2014).

130. Tao, Y., Navaretti, P., Hauert, R., Grob, U., Poggio, M., C L Degen. Permanent reduction of dissipation in nanomechanical Si resonators by chemical surface protection. *Nanotechnology* **26**(46), 465501 (2015). 67, 68

131. Tao, Y., Hauert, R., Degen, C. L. Exclusively Gas-Phase Passivation of Native Oxide-Free Silicon(100) and Silicon(111) Surfaces. *ACS Applied Materials & Interfaces* **8**(20), 13157–13165 (2016). 68

132. Johnson, T. J., Borselli, M., Painter, O. Self-induced optical modulation of the transmission through a high-Q silicon microdisk resonator. *Optics Express* **14**(2), 817 (2006). 69, 74

133. Barclay, P. E., Srinivasan, K., Painter, O. Nonlinear response of silicon photonic crystal micresonators excited via an integrated waveguide and fiber taper. *Optics Express* **13**(3), 801 (2005). 70, 73, 74, 79, 81

134. Green, M. A., Keevers, M. J. Optical properties of intrinsic silicon at 300 K. *Progress in Photovoltaics: Research and Applications* **3**(3), 189–192 (1995). 70

135. Tsang, H. K., Wong, C. S., Liang, T. K., Day, I. E., Roberts, S. W., Harpin, A., Drake, J., Asghari, M. Optical dispersion, two-photon absorption and self-phase modulation in silicon waveguides at 1.5μm wavelength. *Applied Physics Letters* **80**(3), 416–418 (2002). 70

136. Soref, R., Bennett, B. Electrooptical effects in silicon. *IEEE Journal of Quantum Electronics* **23**(1), 123–129 (1987). 70

137. Lautenschlager, P., Garriga, M., Vina, L., Cardona, M. Temperature dependence of the dielectric function and interband critical points in silicon. *Physical Review B* **36**(9), 4821–4830 (1987). 71

138. Turner-Foster, A. C., Foster, M. A., Levy, J. S., Poitras, C. B., Salem, R., Gaeta, A. L., Lipson, M. Ultrashort free-carrier lifetime in low-loss silicon nanowaveguides. *Optics Express* **18**(4), 3582 (2010). 71, 98

139. Aldaya, I. A., Gil-Molina, A., Fragnito, H. L., Dainese, P. C. Simple Method to Simultaneous Characterize Two-Photon Absorption Coefficient and Carrier Lifetime in Silicon Waveguides. In *Latin America Optics and Photonics Conference*, page LTu5D.4. OSA, Washington, D.C. (2016). 71, 74, 75, 90

140. Dimitropoulos, D., Jhaveri, R., Claps, R., Woo, J. C. S., Jalali, B. Lifetime of photogenerated carriers in silicon-on-insulator rib waveguides. *Applied Physics Letters* **86**(7), 071115 (2005). 71, 87, 89, 90

141. Slack, G. A. Thermal Conductivity of Pure and Impure Silicon, Silicon Carbide, and Diamond. *Journal of Applied Physics* **35**(12), 3460 (1964). 74

142. Glassbrenner, C. J., Slack, G. A. Thermal Conductivity of Silicon and Germanium from 3°K to the Melting Point. *Physical Review* **134**(4A), A1058–A1069 (1964).

143. Asheghi, M., Touzelbaev, M. N., Goodson, K. E., Leung, Y. K., Wong, S. S. Temperature-Dependent Thermal Conductivity of Single-Crystal Silicon Layers in SOI Substrates. *Journal of Heat Transfer* **120**(1), 30 (1998). 74, 131

144. Almeida, V. R., Barrios, C. A., Panepucci, R. R., Lipson, M. All-optical control of light on a silicon chip. *Nature* **431**(7012), 1081–1084 (2004). 87

145. Johnson, T. J., Painter, O. J. Passive Modification of Free Carrier Lifetime in High-Q Silicon-on-Insulator Optics. In *Conference on Lasers and Electro-Optics/International Quantum Electronics Conference*, page CFF4. OSA, Washington, D.C. (2009). 87

146. Brasch, V. *Soliton Kerr Frequency Combs Generated in Integrated Photonic Chips*. Ph.D. thesis, École Polytechnique Fédérale De Lausanne (2016). 91

147. Rubiola, E. *Phase noise and frequency stability in oscillators*. Cambridge University Press (2009). 95, 96

148. de Oliveira Luiz, G., P. M. Alegre, T., S. Wiederhecker, G. Synchronization of thermal-carrier oscillations in coupled silicon microcavities. In *Conference on Lasers and Electro-Optics*, page JTh2A.104. OSA, Washington, D.C. (2017). 100

149. Souza, M. C. M. M., Rezende, G. F. M., Barea, L. A. M., Wiederhecker, G. S., Frateschi, N. C. Modeling quasi-dark states with temporal coupled-mode theory. *Optics Express* **24**(17), 18960 (2016). 118

150. Landau, L. D., Lifshitz, E. *Fluid Mechanics, Volume 6*. Elsevier (1987). 124

151. Darling, R. B., Hivick, C., Xu, J. Compact analytical modeling of squeeze film damping with arbitrary venting conditions using a Green's function approach. *Sensors and Actuators A: Physical* **70**(1-2), 32–41 (1998). 128

152. Lyon, K. G., Salinger, G. L., Swenson, C. A., White, G. K. Linear thermal expansion measurements on silicon from 6 to 340 K. *Journal of Applied Physics* **48**(3), 865 (1977). 131

Appendices

A. Optical lumped model equation and the optical spectrum

A.1. Single cavity

The most common equation to treat the coupling of light into an optical cavity is the one presented by Herman Haus in his book Waves and Fields in Optoelectronics [29]. This equation reduces the electromagnetic field equations to a rate equation for its complex amplitude, $a(t)$, and is given by

$$\frac{da(t)}{dt} = \mathrm{i}\omega_0\, a(t) - \frac{\kappa}{2}\, a(t) + \sqrt{\kappa_e}\, s_{in} e^{\mathrm{i}\omega_l t}, \tag{A.1}$$

where ω_0 is the cavity's resonance angular frequency, $\kappa = \kappa_e + \kappa_i$ is the total energy decay rate comprised of the intrinsic cavity losses κ_i and the coupling rate between the cavity and the input channel (e.g., the waveguide) κ_e. s_{in} is related to the input pump power such that $\mid s_{in} \mid^2 = P_{in}$, which oscillates in a given frequency ω_l that is not necessarily resonant with the cavity. Note that this equation appears for both classical and quantum treatment of the occupation of the cavity modes, such that in the former case $\mid a \mid^2$ represents the total energy stored in the cavity, while in the latter it represents the number of photons [31]. The derivation from the Maxwell equations to this rate equation can be found in my Master's degree thesis (in Portuguese) [77] and Felipe's PhD thesis as well (in English) [56].

This equation can be changed to what is called a rotating frame through a transformation of variables of the form $a(t) \rightarrow \tilde{a}(t)e^{i\omega_l t}$. This results in an equation in which the fast oscillation of the electromagnetic filed, both ω_0 and ω_l, vanish and only the slow variation dominated by κ is kept. This is justified because we are interested in the "slow" variations of its amplitude inside the cavity, given by the decay rate and what is called the detuning between input laser and cavity resonance ($\Delta = \omega_l - \omega_0$). Then, equation A.1 becomes

$$\frac{da(t)}{dt} = -\mathrm{i}\Delta\, a(t) - \frac{\kappa}{2}\, a(t) + \sqrt{\kappa_e}\, s_{in}, \tag{A.2}$$

where the tilde was suppressed for simplicity.

To obtain the optical spectrum of the cavity one can assume that the source (s_{in}) frequency is varied such that the energy inside the cavity changes in a much slower time-scale than that defined by κ. In this condition, the cavity can be assumed to respond instantaneously to the variation and equation A.2 can be set equal to zero. This results in a solution for $a(t) = a$

of the form

$$a = \frac{\sqrt{\kappa_e}\, s_{in}}{\mathrm{i}\Delta + \frac{\kappa}{2}}. \tag{A.3}$$

This is the equation for the complex amplitude of the field confined inside the cavity for a given detuning Δ. From this we obtain the detuning dependent stored energy and the normalized transmission (or reflection, depending on the kind of cavity), considering that both input and output are coupled through the same port with coupling rate κ_e. These two quantities are given by

$$U = \mid a \mid^2 = \frac{4\kappa_e P_{in}}{4\Delta^2 + \kappa^2} \quad \text{and} \tag{A.4}$$

$$P_{out} = \frac{\left|\sqrt{P_{in}} - \sqrt{\kappa_e} a\right|^2}{P_{in}} = \frac{4\Delta^2 + (\kappa - 2\kappa_e)^2}{4\Delta^2 + \kappa^2}, \tag{A.5}$$

where we used the relation $\mid s_{in} \mid^2 = P_{in}$ and the signal in $\sqrt{\kappa_e a}$ is a convention related to the relative phase between the input and output fields. This is the typical function used to fit simple resonances, obtaining the relevant parameters to properly characterize the optical modes of a cavity in absence of couplings.

A.2. Two coupled cavities

To obtain the equations for coupled cavities or for the case when a single cavity presents coupled modes, one must turn to the coupled mode theory of optical modes [96]. This method uses the same initial equation A.1, but now one for each mode coupled to each other, which in the rotating frame are given by

$$\frac{da_1(t)}{dt} = -\mathrm{i}\Delta_1\, a_1(t) - \frac{\kappa_1}{2}\, a_1(t) + \sqrt{\kappa_e}\, s_{in} s + \mathrm{i}\frac{\mathrm{g}_{12}}{2} a_2(t) \quad \text{and} \tag{A.6}$$

$$\frac{da_2(t)}{dt} = -\mathrm{i}\Delta_2\, a_2(t) - \frac{\kappa_2}{2}\, a_2(t) + \mathrm{i}\frac{\mathrm{g}_{12}}{2} a_1(t), \tag{A.7}$$

where g_{12} is the coupling rate between modes 1 and 2, which can be either the modes of two cavities or two modes of the same cavity. Rigorously, this coupling rate can be estimated from the overlap of the modes and the energy and momentum conservation laws. Here we wrote the more general problem, with the two modes having different resonant frequencies, resulting in different detunings of the laser, and different intrinsic decay rates. Note that for a typical coupled cavity system κ_2 doesn't include a contribution from κ_e, as the second cavity only receives light through the first, and only the latter is coupled to the waveguide. This is not necessarily true for the case of coupling between two modes of the same cavity, e.g., when there is coupling of counter-propagating modes. Also, if there is coupling between different modes of the same cavity, because their coupling to the waveguide can be different, this must be considered and the equations modified. Nonetheless, we do not add such complications here

because there is little contribution for the intended discussion.

Solving the adiabatic approximation to this set of equations ($da_i(t)/dt = 0$, with $i = 1,\ 2$) we obtain the function for the normalizes transmission, assuming that it couples through the same port of the input. This is the function fitted to the spectra of two coupled modes. Of course this can be scaled up to various coupled modes, but be aware that for some coupled cavity designs this method can lead to a reduced amount of resonances with respect to the experimental data, as discussed by Souza *et al.* [149].

$$P_{out} = \frac{\left|s_{in} - \sqrt{\kappa_e}\, a_1\right|^2}{P_{in}} = \frac{4\Delta_1^2\left(4\Delta_2^2+\kappa_2^2\right) - 8\Delta_1\Delta_2 g_{12}^2 + \left(4\Delta_2^2+\kappa_2^2\right)(\kappa_1 - 2\kappa_e)^2 + g_{12}^4 + 2g_{12}^2\kappa_2(\kappa_1 - 2\kappa_e)}{4\Delta_1^2\left(4\Delta_2^2+\kappa_2^2\right) - 8\Delta_1\Delta_2 g_{12}^2 + 4\Delta_2^2\kappa_1^2 + \left(g_{12}^2 + \kappa_1\kappa_2\right)^2} \tag{A.8}$$

B. Acetylene spectrum

Here is an example of the spectrum of the acetylene cell used as an absolute wavelength reference for the calibration of the optical spectra of the cavities presented in this thesis.

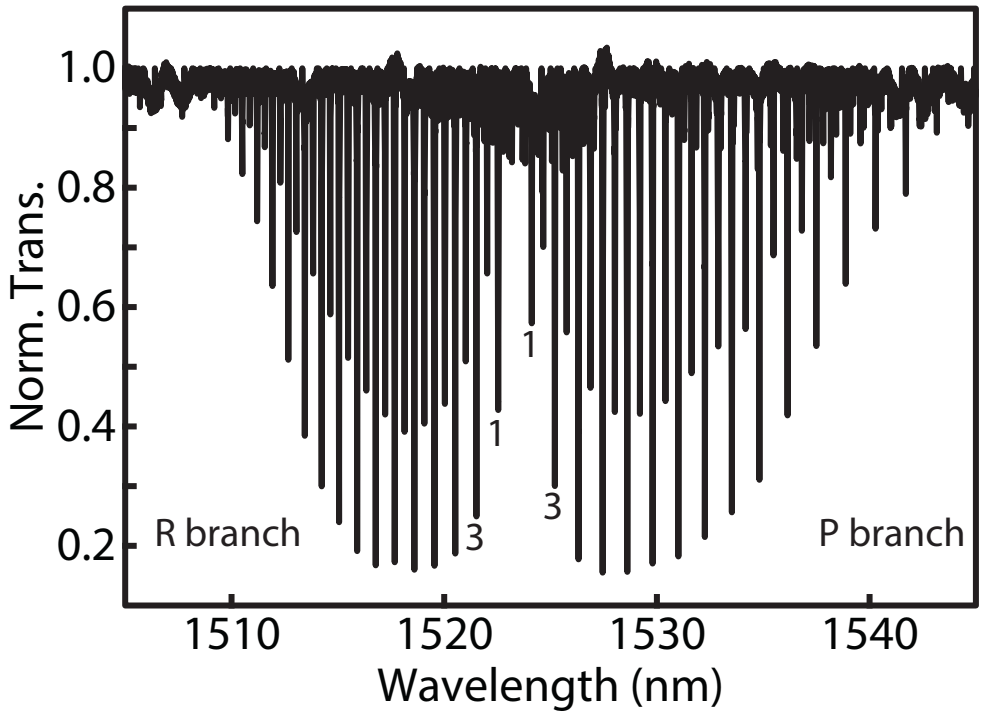

Figure B.1: **Normalized transmission of an acetylene cell.** The numbers indicate the first and third resonances in the R and P branches.

C. Homodyne detection signal model

To understand the detuning dependent signal obtained in this setup (sec. 3.2), let us first look into the expected transmission for a simple resonance like the one represented by equation A.2. For that we must write the polarization dependent transfer matrices of all the relevant components.

The input laser is given by the vector

$$E_{in} = \begin{pmatrix} 1 \\ 0 \end{pmatrix}. \tag{C.1}$$

The half wavelength plate matrix is obtained from

$$T_{\lambda/2}(\theta) = \begin{pmatrix} cos(\theta) & -sin(\theta) \\ sin(\theta) & cos(\theta) \end{pmatrix} \begin{pmatrix} 1 & 0 \\ 0 & -1 \end{pmatrix} \begin{pmatrix} cos(\theta) & sin(\theta) \\ -sin(\theta) & cos(\theta) \end{pmatrix}. \tag{C.2}$$

The quarter wavelength plate matrix results from

$$T_{\lambda/4}(\theta) = \begin{pmatrix} cos(\theta) & -sin(\theta) \\ sin(\theta) & cos(\theta) \end{pmatrix} \begin{pmatrix} 1 & 0 \\ 0 & \mathrm{i} \end{pmatrix} \begin{pmatrix} cos(\theta) & sin(\theta) \\ -sin(\theta) & cos(\theta) \end{pmatrix}. \tag{C.3}$$

The linear polarizing plate matrix is given by

$$T_{LP}(\theta) = \begin{pmatrix} cos(\theta) & -sin(\theta) \\ sin(\theta) & cos(\theta) \end{pmatrix} \begin{pmatrix} 1 & 0 \\ 0 & 0 \end{pmatrix} \begin{pmatrix} cos(\theta) & sin(\theta) \\ -sin(\theta) & cos(\theta) \end{pmatrix}. \tag{C.4}$$

Finally, the cavity matrix is given by

$$T_C(\Delta) = \begin{pmatrix} 1 - \frac{2\kappa_e}{\kappa - 2\mathrm{i}\Delta} & 0 \\ 0 & 1 \end{pmatrix}. \tag{C.5}$$

In all this elements, θ is the rotation of the plate with respect to a reference axis (e.g, the cavity optical mode preferential orientation), $\mathrm{i} = \sqrt{-1}$ is the imaginary unit, κ is the optical mode decay rate, κ_e is the coupling rate of the cavity to the waveguide and Δ the relative detuning between input laser and optical mode. Note that, for simplicity, it was assumed that the laser emits in the same polarization of the cavity mode.

The total transfer matrix of this system is obtained simply multiplying all these element components, resulting in

$$T_{Total}(\Delta, \theta_{in}, \theta_{out}) = T_{\lambda/2}(\theta_{out}) T_{\lambda/4}(\theta_{out}) T_C(\Delta) T_{\lambda/2}(\theta_{in}) T_{\lambda/4}(\theta_{in}), \tag{C.6}$$

where θ_{in} is the input and θ_{out} the output polarization rotations.

Finally, we obtain the output field in the two orthogonal polarizations by multiplying the total transfer matrix to the input field and, to produce the two outputs of the polarizing beam-splitter, to the linear polarization matrix. This gives

$$E_{out}^{(V)}(\Delta, \theta_{in}, \theta_{out}) = T_{LP}(\theta_V) T_{Total}(\Delta, \theta_{in}, \theta_{out}) E_{in} \quad \text{and} \tag{C.7}$$

$$E_{out}^{(H)}(\Delta, \theta_{in}, \theta_{out}) = T_{LP}(\theta_H) T_{Total}(\Delta, \theta_{in}, \theta_{out}) E_{in}. \tag{C.8}$$

Figure C.1 shows the resulting detuning dependent signals, obtained by taking the intensity $\left| E_{out}^{H,V} \right|^2$, which is responsible for producing the photocurrent on the photodetector.

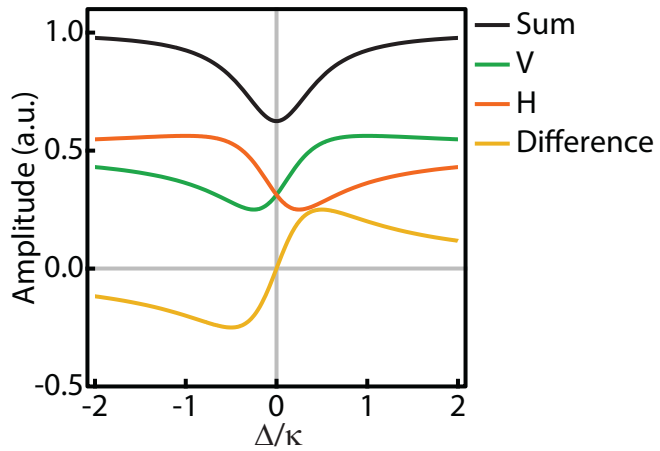

Figure C.1: **Theoretical signals from the output of a homodyne detection scheme.** The sum results in the usual transmission signal, but with smaller extinction due to the polarization rotation of the input. The difference gives a dispersive curve with non-zero derivative at zero detuning.

D. Numerical Estimative of g_0

To estimate the optomechanical coupling of the paddles in chapter 4 we solve the problem of the disk without the paddle using COMSOL®. Figure D.1 shows the geometry used, which takes advantage of the axial symmetry of the cavity, allowing to solve a 2-D problem, instead of a 3-D.

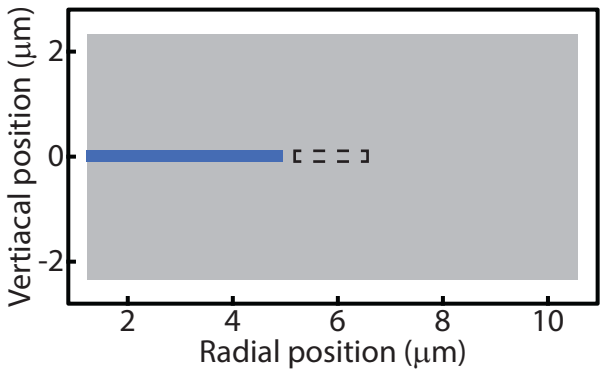

Figure D.1: **Computational domain to estimate g_0.** Gray area is the computational domain set to have the index of refraction of air, while the blue is set to that of silicon. Dashed line marks the position of the front paddle.

When solving this problem one have the option of giving a fixed azimuthal number m and the software returns the different eigenfrequencies. But we want to compare the difference in g_0 for different radial order mode, hence it is more interesting to give a fixed eigenfrequency and solve for m, which returns a set of modes with varying m and radial order. The solution also includes the field distribution for each mode, as shown in the insets of figure 4.10 in chapter 4.

The optomechanical frequency shift caused by the motion of the paddle, $G_{\mathrm{OM}} = g_0/x_{\mathrm{zpf}}$, is calculated for each mode using perturbation theory. That is done using the expression derived by Steven Johson [22], which can be written as

$$G_{\mathrm{OM}} = \frac{\omega_0}{2} \frac{\int_S |\mathbf{U}_n| \left(\Delta\varepsilon |\mathbf{E}_t|^2 + \Delta\varepsilon^{-1} |\mathbf{D}_n|^2\right) dA}{\int_V \varepsilon_0 n^2 |\mathbf{E}|^2 dV}, \tag{D.1}$$

where $x_{zpf} = \sqrt{\hbar/(2m_{eff}\Omega_m)}$ is the quantum zero-point fluctuation of a mechanical mode with effective mass m_{eff} and angular frequency Ω_m, ω_0 is the optical unperturbed resonance frequency, $\mathbf{U}_n$ is the normalized mechanical displacement perpendicular to the surface S, $\Delta\varepsilon = \varepsilon_0(n_{in}^2 - n_{out}^2)$ is the difference of refractive index inside and outside the material, $\Delta\varepsilon^{-1} = \varepsilon_0^{-1}(n_{in}^{-2} - n_{out}^{-2})$ is the difference of n^{-2} inside and outside the material, $\mathbf{E}_t$ is the field tangent to the surface, $\mathbf{D}_n$ is the electric displacement normal to the surface and $\mathbf{E}$ is the total electric field distributed in a volume V. The use of the absolute value in the displacement ($|\mathbf{U}_n|$) means that the mechanical displacement is positive when the boundary movement points from

the higher to the lower refractive index media, at the surface where the integral is evaluated.

In order to make the calculation simpler, the paddle was considered to curve its surfaces along the disk edge, instead of being flat as the SEM images show. Note that the exponential decay of the optical field in the radial direction makes the field much less intense on the surfaces of the paddles that are farther than 200 nm from the disk's border. Then, the surface integral is evaluated only on the surface closest to the disk, 200 nm form the border, while the others don't affect significantly the results. Also, this surface is considered because it is the one perpendicular to the direction of the motion of the mechanical modes studied in this thesis. The volume integral is evaluated over the entire computational domain.

The drawback of solving this 2-D axis-symmetric geometry is that we either underestimate the value of g_0, by not including the paddle, because we don't have the discontinuity of the field in the radial direction, or we overestimate it, by including the paddle, because the solution is given considering not a finite 2 μm long paddle but a circular ring around the disk. Moreover, the fact the paddle becomes a ring in the latter case implies that it also supports WGM modes, which in turn can couple to the disk's modes, impairing the analysis. Hence, we decided to perform this analysis by not including the paddle on the geometry for the FEM solution, but its effect is accounted by properly setting the values for $\Delta\varepsilon$ and $\Delta\varepsilon^{-1}$ in equation D.1.

E. Air Damping

E.1. Lateral drag-force

At atmospheric pressure, any mechanical device is subject to forces due to the viscosity of the air. The most common way to analytically study these forces starts with the Navier-Stokes equation for the flow of a viscous material, together with the continuity equation, which are given by

$$\rho\left[\frac{\partial\vec{v}}{\partial t}+\vec{v}\cdot\left(\vec{\nabla}\vec{v}\right)\right]=-\vec{\nabla}P+\mu\vec{\nabla}^2\vec{v}+\left(\zeta+\frac{1}{3}\mu\right)\vec{\nabla}\left(\vec{\nabla}\cdot\vec{v}\right)\quad\text{and}\tag{E.1}$$

$$\rho\vec{\nabla}\cdot\vec{v}=\frac{\partial\rho}{\partial t},\tag{E.2}$$

where ρ is the fluid density, $\vec{v}$ is the fluid velocity with respect to the confining boundaries, P is the pressure distribution throughout the fluid, μ is the dynamic viscosity and ζ the second viscosity [150].

In general, micro-mechanical-resonators present very little amplitudes of motion, specially when one is interested only in thermal excitation, which for a mode resonant at 55 MHz and with 3 pg of effective mass have about 5 pm of amplitude. This allows to treat air as an incompressible fluid, which means making $\partial\rho/\partial t=0$, resulting in the incompressible fluid Navier-Stokes equation given by

$$\rho\left[\frac{\partial\vec{v}}{\partial t}+\vec{v}\cdot\left(\vec{\nabla}\vec{v}\right)\right]=-\vec{\nabla}P+\mu\vec{\nabla}^2\vec{v}.\tag{E.3}$$

Considering the device and mechanical modes presented in chapter 4, the main sources of drag force are the top and bottom surfaces of the paddles. That is because these are the regions that drag the most amount of air when they move, transferring energy to the fluid. Because the amplitude of motion is much smaller than the paddles' dimensions, the paddles can be treated as infinite plates, ignoring edge effects [91, 150]. This means that we can ignore the convection term $(\vec{v}\cdot\vec{\nabla}\vec{v})$ in equation E.3. Moreover, the infinite plate approximation means that both $\vec{v}$ and P are uniform on the (x,y) plane. This simplifies equation E.3 to

$$\rho\frac{\partial v_x}{\partial t}\hat{\mathbf{x}}=-\frac{\partial P}{\partial z}\hat{\mathbf{z}}+\mu\frac{\partial^2 v_x}{\partial z^2}\hat{\mathbf{x}},\tag{E.4}$$

where v_x is the fluid velocity component in the $\hat{\mathbf{x}}$ direction.

Note that the $\hat{\mathbf{z}}$ component of equation E.4 ($\partial P/\partial z=0$), together with the initial assumption that pressure is uniform in the (x,y) plane, imply that pressure is uniform in all directions inside the fluid, in other words, there is no pressure gradient, which results in zero

flow. Then the equation to be solved is reduced to

$$\rho \frac{\partial v_x}{\partial t} = \mu \frac{\partial^2 v_x}{\partial z^2}. \tag{E.5}$$

Now we only need to define the boundary conditions of the system. Figure E.1 shows the schematics of an infinite plate suspended over a fixed substrate. For the devices presented in chapter 4 $h_0 = 2$ µm and $d = 220$ nm. This figure will be used as a reference for determining boundary conditions.

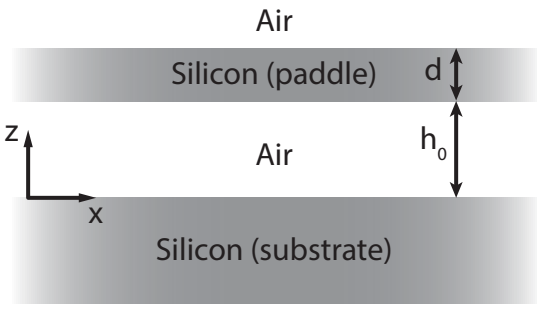

Figure E.1: **Lateral drag-force boundary conditions.** Lateral view of a suspended infinite plate over an infinite fixed substrate, with air filling the regions between and above the plate.

Because of the small amplitude approximation, the boundary conditions can be simplified stating that air velocity, relative to the plate and substrate surfaces, is zero at the surfaces and also very far from the system ($z \to \infty$). Hence we obtain

$$\begin{aligned} v_x(z=0) &= 0, \\ v_x(z=h_0) &= 0, \\ v_x(z=h_0+d) &= 0 \quad \text{and} \\ v_x(z\to\infty) &= 0, \end{aligned} \tag{E.6}$$

where $z = 0$ is the substrate top surface.

Solving equation E.5 for the region above the plate ($z \geq h_0 + d$), with the correct boundary conditions, we obtain

$$v_x(z,t) = v_0 e^{\frac{h_0+d}{\delta}(1-i)} e^{-\frac{z}{\delta}} e^{i\left(\frac{z}{\delta} - \Omega_m t\right)}, \tag{E.7}$$

where v_0 is the plate velocity amplitude, $\delta = \sqrt{2\eta/\Omega_m}$ is a characteristic distance with $\eta = \mu/\rho$ being the fluid cinematic viscosity and Ω_m the frequency of the plate motion. Note that the lateral motion excites transverse waves on the fluid, but this kind of waves are not allowed to propagate in fluids as they present no resistance to sheer stress, hence the characteristic distance is in fact a penetration depth of the transverse waves excited.

For the region between plate and substrate ($0 \leq z \leq h_0$) the solution to equation E.5,

with the correct boundary conditions is

$$v_x(z,t) = \frac{v_0 e^{-i\Omega_m t} \sin\left[(1+i)\frac{z}{\delta}\right]}{\sin\left[(1+i)\frac{h_0}{\delta}\right]}, \tag{E.8}$$

Because the distance between plate and substrate ($h_0 = 2$ µm) is much larger than the characteristic distance ($\delta \approx 300$ nm), equations E.7 and E.8 give practically identical results. Hence we can use only expression E.7 to estimate the attenuation of the paddle modes presented in chapter 4. For that purpose we obtain the force per unit of area that air exerts on the plate from

$$f = \mu \frac{\partial v_x}{\partial z}\bigg|_{z=h_0,h_0+d}. \tag{E.9}$$

The real part of this force is proportional and opposite to the plate's velocity, which generates energy dissipation. The imaginary part, in phase with displacement, acts like an extra spring constant, causing a small change to the oscillation frequency. It is simple to show that the attenuation due to lateral drag force in the paddles is given by

$$\Gamma_m^{LD} = \mathrm{Re}\left\{\frac{4\,f\,A}{v_0\,m_{eff}}\right\}, \tag{E.10}$$

where A is the area of a paddle and m_{eff} is the effective mass of the mechanical mode. The factor 4 accounts for the top and bottom surfaces of the two paddles.

Although v_0 appears in equation E.10, recall that $f \propto v_0$, hence there is no need to estimate the velocity of the motion, although it is a simple task for a thermally driven system. For the devices presented in chapter 4, whose effective mass is approximately 3 pg, expression E.10 results in an estimated lateral drag-force limited mechanical Q of about 1k. Comparing with experimental data taken with the samples at atmospheric pressure (fig. E.2), we find that this is 56% larger than the measured value for the AS mode ($Q_{AS}^{ATM} = 640$), but only 18% larger than the the S mode value ($Q_S^{ATM} = 850$).

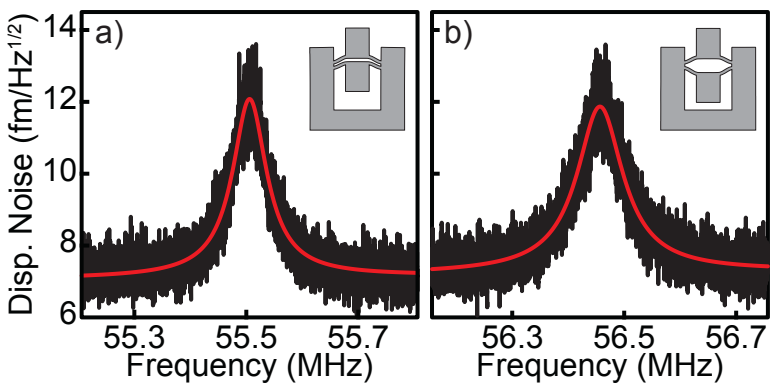

Figure E.2: **Displacement spectral density at room conditions.** S (a) and AS (b) modes' calibrated displacement spectral density at room temperature. Data is shown in black and fitted Lorentzians in red. $f_m \approx 56$ MHz and splitting of 940 kHz. Data of device with $\delta = -50$ nm.

The fact the the AS mode has lower Q-factor than the S mode at room conditions is evidence that another viscous effect is taking place for that device. In this case it can be squeeze-film damping, which could be larger for the AS mode as the distance between paddles changes during the oscillations for this mode, while it is approximately fixed for the S mode.

E.2. Squeeze-film damping

Squeeze film damping (SFD) occurs when a fluid is compressed between moving structures. This is a well known process present in fluid bearings and shock absorbers. In micromechanical resonators this is an important energy dissipation mechanism, specially for modes that modulate small distances between structures. That is because the variation of separation between structures causes pressure changes, which may force fluid movement in and out the region, depending on increase or decrease of space. Because fluids are typically viscous this process leads to dissipation of energy from the mechanical modes.

In order to model such effect we assume:

1 – No slip velocity — this means that there is no lateral velocity of the fluid relative to the boundaries, at the boundaries;

2 – Fluid velocity on the boundaries matches the boundaries velocity;

3 – Pressure is uniform in the direction of the boundary motion ($dP/dn = 0$);

4 – Boundaries' dimensions are much larger than the gap between them;

5 – Isothermal expansion/compression — this means that the fluid density is proportional to pressure;

6 – Gap modulation is much smaller than the gap itself;

7 – Boundaries are the only source of pressure variation, i.e. there are no other external forces acting on the fluid;

8 – Laminar flow — this is reasonable for small amplitude motion in micromechanical resonators;

9 – Fully developed flow — this means that the fluid is incompressible.

This reduces the Navier-Stokes's equation to the Reynold's equation given by

$$\vec{\nabla} \cdot \left(\frac{h^3(\vec{r},t)}{\mu} P(\vec{r},t) \vec{\nabla} P(\vec{r},t) \right) = 12 \frac{\partial \left(h(\vec{r},t) P(\vec{r},t) \right)}{\partial t}, \tag{E.11}$$

where $h(\vec{r},t) = h_0 + \delta(\vec{r},t)$ is the distance between structures, with h_0 being the equilibrium position and $\delta(\vec{r},t)$ the variation of this distance, μ is the fluid's dynamic vicosity and $P(\vec{r},t) =$

$P_a + p(\vec{r},t)$ is the total pressure of the fluid between the structures, with P_a being the atmospheric pressure (equilibrium) and $p(\vec{r},t)$ the variation with respect to equilibrium. Note that one of the assumptions to get to the Reynold's equation is that in the direction of motion the fluid pressure is uniform. This means that the dependency of pressure on position can be reduced to $\vec{r} = (x,y,0)$, if the motion is considered to happen in the $\hat{\mathbf{z}}$ direction. Detailed explanation on the assumptions and how they lead to eq. E.11 can be found in references [93, 94, 151].

Because $\delta \ll h_0$, equation E.11 can be linearized by expanding its terms up to the first order in δ. For simplicity the distance variation in the region between the paddles and close to the disk is assumed to be uniform, i.e., the motion is treated as that of parallel, solid and rigid plates. This means that $\delta(\vec{r},t) = \delta(t)$. Also we can rewrite the Reynold's equation in terms of normalized variables $\mathbb{P} = p/P_a$ and $\mathbb{H} = \delta/h_0$. In this way we arrive at the linearized and normalized Reynold's equation:

$$\vec{\nabla}^2\mathbb{P} = \frac{12\mu}{h_0^2 P_a}\left(\frac{\partial \mathbb{P}}{\partial t} + \frac{\partial \mathbb{H}}{\partial t}\right). \tag{E.12}$$

As noted by Darling *et al.* [151], the problem is now reduced to a simple diffusion equation with a source of the form $(12\mu/h_0^2 P_a)\partial\mathbb{H}/\partial t$. The solution to this equation can be found using the Green function approach, which results in a time-dependent pressure given by

$$p(t) = \sum_{m,n=\text{ímpares}} \left(\frac{8}{\pi^2 mn}\right) \frac{i\sigma P_a}{i\sigma + (m\pi)^2 + (\beta n\pi)^2} \mathbb{H}_0 e^{i\Omega_m t}, \tag{E.13}$$

where $\mathbb{H}_0 = \delta_0/h_0$ is the plates motion normalized amplitude, $\beta = L/W$ with L and W the plate dimensions in directions $\hat{\mathbf{x}}$ and $\hat{\mathbf{y}}$, respectively. The constant $\sigma = (12\mu\Omega_m L^2)/(h_0^2 P_a)$ is called the compression number, and can be interpreted as a normalized frequency. Note that the spacial dependency was ignored, but it is easily recovered by recalling that $\mathbb{H}_0 = \mathbb{H}_0(\vec{r})$, as both δ_0 and h_0 may depend on the mechanical mode and plates profiles, respectively.

Finally, it is possible to estimate the dissipation rate due to squeeze-film between the paddles with equation E.14. In this case the imaginary component of the force is the one that causes damping and it is given by

$$\Gamma_m^{SFD} = \mathrm{Im}\left\{\frac{p(t)\,A}{m_{eff}\,h_0\,\Omega_m}\right\}. \tag{E.14}$$

The estimated damping rate due to this effect in the paddles is of approximately 6 kHz for the AS mode, and 2 kHz for the S mode. Hence this effect doesn't seem to be very important in these devices. But it is important to observe that one of the assumptions to this model is that the distance between plates is much smaller the their own dimensions, which is not true for the paddles. Hence the SFD might be underestimated by not considering edge effects, which would explain the discrepancy between estimated and experimental values.

F. Taper fiber fabrication

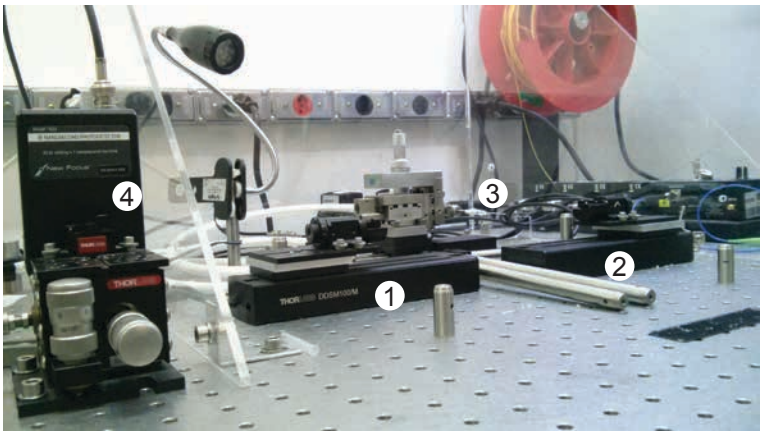

Figure F.1: **Teper pulling setup.** 1 and 2 indicate the pulling motors, 3 indicates the flame position and 4 the photodetector.

The tapered fibers (taper) we used were all fabricated in the group's lab following the process described by Birks and Li [65]. A single mode (SMF28) fiber is cleaned and mounted in the setup shown in figure F.1. This setup comprises of a pair of pulling motors (1,2), and a flame (3) that can move sideways and back and forth. The flame is fed with a mixture of pure isobutane (99.5%) and pure oxygen (99.99%), controlled by two mass-flow controllers.

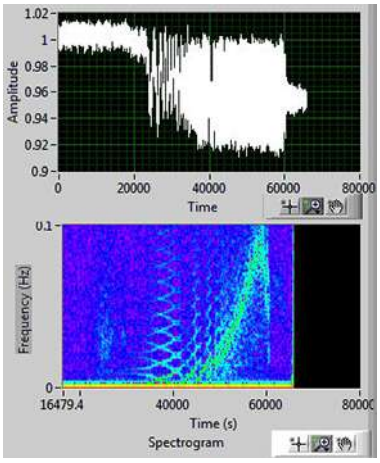

Figure F.2: **Example of transmission time-trace and spectrogram of a taper being pulled.**

The taper transmission at 1.55 µm is monitored using a photodetector (4 in fig. F.1) connected to a DAQ system. From this transmission it is possible to infer if the taper has become single mode, stopping the pulling process at the correct time. This verification is greatly facilitated by monitoring the spectrogram of the transmitted light, as shown in figure F.2. This spectrogram shows the result of interferences occurring in the tapering region as the fiber is stretched. Because these interferences are the result of the taper being multi-mode, one knows that taper is single mode when the spectrogram is devoid of beating lines.

Once the taper is done it is needed to create a loop in its thinest region (fig. F.3). This is necessary in order to guarantee that when the fiber is coupled to a device it only touches that single device and no other part of the chip. It also guarantees that the loop is the only region close to the sample, otherwise there could be optical power leakage from the fiber to the substrate, as the latter typically has much higher refractive index (silicon) than the fiber. This loop typically has 100 µm or less in diameter. The taper is then attached to a glass blade, the same used for optical microscopy, and set on the measuring setup.

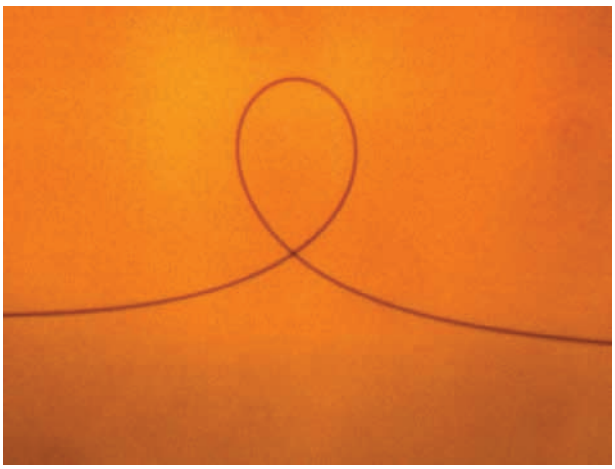

Figure F.3: **Example of a loop taper.**

People often question if the loop doesn't form a cavity in the taper, what would cause problems in measurements by adding extra resonance features to it. Note that te crossing point of the fiber forms almost perfectly a right angle, which greatly reduces the chances of light traveling in one direction to couple to the other. Most of the background problems our group encounters in the optical characterization of the samples are due to the taper not being defect-free or single-mode, causing wavelength dependent interferences on the transmitted light. Also, the crossing point of the loop causes scattering of light, which in turn can generate some interference features on the transmitted signal.

G. Temperature dependent material properties

Figure G.1 summarizes the properties of silicon used to estimate TED and AKE mechanical Q limits as a function of temperature. For TED were used the measured SOI thermal conductivity by Asheghi *et al.* [143], bulk silicon heat capacity by Desai [120] and bulk silicon coefficient of thermal expansion by Lyon *et al.* [152]. For AKE were used the measured bulk silicon heat capacity by Desai [120], sound speed and thermal phonon lifetime of bulk silicon by Lambade *et al.* [113] and the Grüneisen parameter by Philip and Breazeale [114].

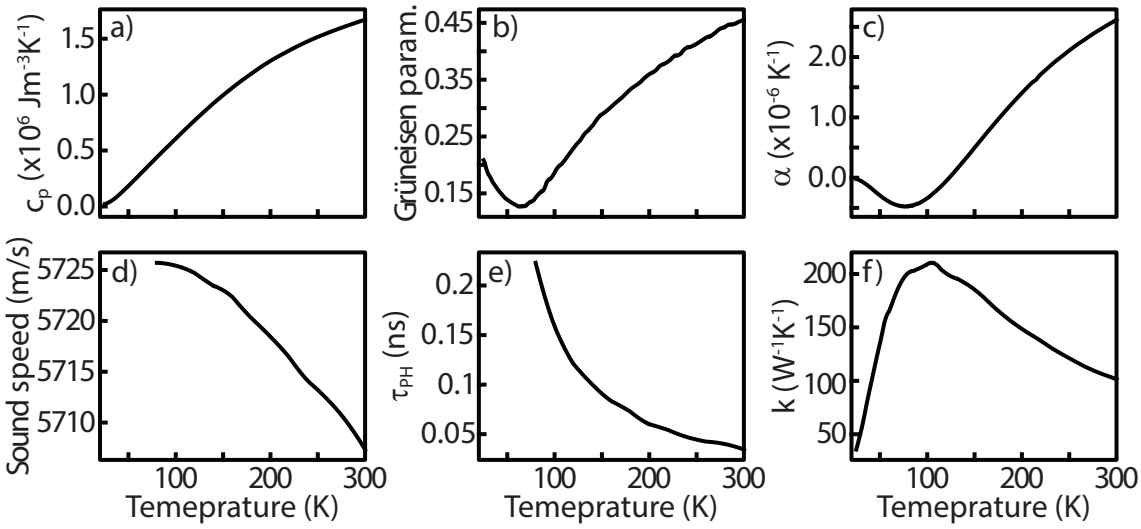

Figure G.1: **Silicon properties versus temperature. a)** Heat capacity [120]; **b)** Grüneisen parameter [114]; **c)** Coeffcient of thermal expansion [152]; **d)** Average Debye sound speed [113]; **e)** Mean thermal phonon life-time [113]; **f)** Thermal conductivity [143].

H. Parameter values for the self-pulse model

These are the material and other parameters used in the model presented in chapter 5. Here t_Si is the silicon layer thickness (220 nm) and r_{disk} is the disk radius (2 µm). The two values given for τ_{th} ar for the double and single cavity systems, respectively.

Table H.1: **Table with parameter values used in chapter 5.**

Parameter	**Vaule**
ρ	2330 kg/m^3
c_p	712 J/(kg K)
n_{Si}	3.485
n_g	0.99 n_{Si}
λ_0	1471.63 nm
κ	$2\pi \times 2.55$ GHz
κ_e	$2\pi \times 1.17$ GHz
κ_i	$\kappa - \kappa_e$
κ_{lin}	$\kappa_i/2$
τ_{FC}	5.8 ns
γ_{FC}	$1/\tau_{FC}$
τ_{th}	(7.0, 3.5) µs
γ_{th}	$1/\tau_{th}$
T_0	300 K
$dn/d\theta$	1.86×10^{-4} K^{-1}
dn/dN	-1.73×10^{-27} m^3
σ_{Si}	10^{-21}m^2
β_{Si}	8.410^{-12} m/W
Γ_{TPA}	1
V_{TPA}	1.24×10^{-18}m^3
Γ_{FC}	1
V_{FC}	1.15×10^{-18}m^3
Γ_{disk}	0.97
V_{disk}	$\pi r_{disk}^2 t_{Si} = 2.76 \times 10^{-18}$m^3

I. Codes for GDS generation

The design sent to the foundry for fabrication of the samples are in a specific format, called GDSII. To generate this file a code in Python 3 was created using the package *gdspy*, which is available through the *pip* package repository. Figures I.1 shows the design generated for the work on the paddle NFO devices.

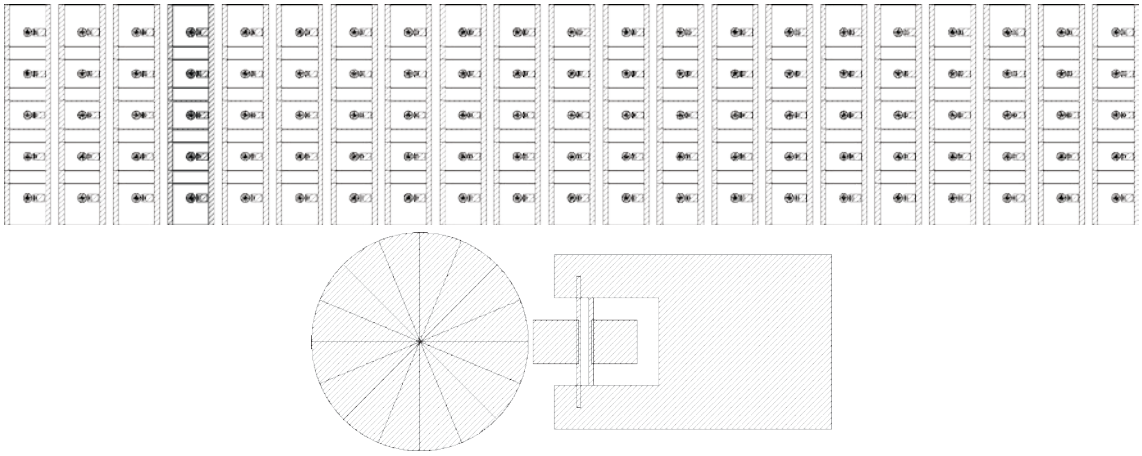

Figure I.1: **GDS of the paddle optomechanical devices.** Top image shows an array in which the asymmetry parameter varies in the horizontal direction, while the gap between paddles varies in the vertical direction. Bottom image shows a zoom in one of the devices to show more details.

An important detail in this design is that the disks are constructed from smaller sections. This was done because of two particularities of the GDS format: first, it only supports polygons, i.e., circles are drawn as many-sided polygons; second, the maximum number of vertices in a single polygon is 200. Hence, the circles in the designs our group sent to the foundry were split into various sections, increasing the number of vertices on their edges. This reduces the chances of the final optical cavities having their quality factor limited by scattering in defects induced by the design rather than the fabrication process.

Below is a code that generates a two-dimensional array of the paddle NFO devices presented in chapter 4, with the gap between paddles varying in one dimension and the asymmetry in the other. This code should be a working example if all necessary packages are properly installed, and it should produce a file with the design on the top of figure I.1. Although *gdspy* has a built-in gds-viewer, we suggest the free software *KLayout* for easy visualization of the designs.

```
import os
import numpy
import gdspy

def paddle_oscillator(center, rad, gap, size1, size2, size3): # This function defines the paddles
    # These are the meaning of the parameters:
        # center - center of the disk [x,y]
        # rad - radius of the disk
        # gap[] - gap between disk and front paddle [0], gap between two paddles [1]  , air gap
    from taper parking lot [2]
        # size1[] - paddle width, height and asymmetry
        # size2[] - paddle clamping beams width and height
        # size3[] - parking lot width and length (for the taper)
    paddle=[]
    #Front paddle - closer to cavity
    uleft = ( center[0] + rad + gap[0] , center[1] + size1[1]/2)
    bright= ( center[0] + rad + gap[0] + size1[0]+size2[0]/2, center[1] - size1[1]/2)
    paddle.append(gdspy.Rectangle(uleft, bright, **wgcor))
    #Front paddle clamp beam left
    uleft = ( center[0] + rad + gap[0] + size1[0], center[1] + size1[1]/2 + size2[1]+0.5*size3
     [1])
    bright= ( center[0] + rad + gap[0] + size1[0] + size2[0], center[1] - size1[1]/2 - size2[1]-
     0.5*size3[1])
    paddle.append(gdspy.Rectangle(uleft, bright, **wgcor))
    #Front paddle clamp beam right
    uleft = ( center[0] + rad + gap[0] + size1[0] + 1*size2[0]+gap[1], center[1] + size1[1]/2 +
     size2[1])
    bright= ( center[0] + rad + gap[0] + size1[0] + 2*size2[0]+gap[1], center[1] - size1[1]/2 -
     size2[1])
    paddle.append(gdspy.Rectangle(uleft, bright, **wgcor))
    #Back paddle- farther away from cavity
    uleft = ( center[0] + rad + gap[0] + 1*size1[0]+2*size2[0] + gap[1]-size2[0]/2  , center[1] +
      size1[1]/2)
    bright= ( center[0] + rad + gap[0] + 2*size1[0]+2*size2[0] + gap[1] + size1[2], center[1] -
     size1[1]/2)
    paddle.append(gdspy.Rectangle(uleft, bright, **wgcor))
    #Parking lot for the taper
    uleft = ( center[0] + rad + gap[0] + size1[0]/2, center[1] + size1[1]/2 + size2[1]+size3[1])
```

```
    bright= ( center[0] + rad + gap[0] + 1.5*size1[0]+2*size2[0] + gap[1] + size1[2] + gap[2]+
     size3[0], center[1] - size1[1]/2 -size2[1]-size3[1])
    rect1a = gdspy.Rectangle(uleft, bright, **wgcor)
    uleft = ( center[0] + rad + gap[0] + size1[0]/2, center[1] + size1[1]/2 + size2[1])
    bright= ( center[0] + rad + gap[0] + 1.5*size1[0]+2*size2[0] + gap[1] + size1[2] + gap[2],
     center[1] - size1[1]/2 -size2[1])
    rect1b = gdspy.Rectangle(uleft, bright, **wgcor)
    p_lot = gdspy.boolean( [rect1a,rect1b], lambda rect1, rect2: rect1 and not rect2, **wgcor)
    paddle.append(p_lot)
    return paddle

def p_lot_2(center, offset, rad, width, gap): # This function creates the taper parking lot
    # Input variables are:
        # center - center of the disk [x,y]
        # offset - offset from disk center [x,y]
        # rad - disk radius
        # width - parking lot dimensions [x,y]
        # gap - gap between disk and parking lot [x,y]
    #p_lot_outer
    uleft = ( (center[0]-offset[0]) - rad - gap[0] - width[0], (center[1]-offset[1]) + rad + gap[1]+
     width[1] )
    bright= ( (center[0]-offset[0]) + rad + gap[0] + width[0], (center[1]-offset[1]) - rad - gap[1]
     - width[1] )
    rect1a = gdspy.Rectangle(uleft, bright, **wgcor)
    #p_lot_inner
    uleftr1 = ( (center[0]-offset[0]) - rad - gap[0], (center[1]-offset[1]) + gap[1] + rad )
    brightr1= ( (center[0]-offset[0]) + rad + gap[0], (center[1]-offset[1]) - gap[1] - rad )
    rect1b = gdspy.Rectangle( uleftr1, brightr1, **wgcor)
    p_lot = gdspy.boolean( [rect1a,rect1b], lambda rect1, rect2: rect1 and not rect2, **wgcor)
    return uleftr1, brightr1, p_lot

# Define layers and datatype
wghol = {'layer':37, 'datatype':2}
wgcor = {'layer':37, 'datatype':4}
wgcld = {'layer':37, 'datatype':5}
wgtre = {'layer':37, 'datatype':6}
fchol = {'layer':35, 'datatype':2}
fccor = {'layer':35, 'datatype':4}
fccld = {'layer':35, 'datatype':5}
```

```
fctre = {'layer':35, 'datatype':6}
nofill = {'layer':10158, 'datatype':0}

# ---------------------------------- ##
# Disk with paddle oscillators - GAP AND ASSYMETRY
# ---------------------------------- ##
# Parameters, all given in um
p_lot_array=[]
paddle_cell2 = gdspy.Cell('paddle2')
dsk_rad = 5 # Disk radius
clamp_width = 0.2 #width of the strings that support the paddles
clamp_length = 1 #length of the strings that support the paddles
drum_length = 2 #Paddles length
drum_width = 2 # Paddle width
n_copies=1 # number of paddle oscillators coupled to the optical cavity
n_angular=8 # angular separation 360/n_angular between paddle devices in the same optical
    cavity
paddle_p_lot_width = 2 # Width of supporting beam to which the strings are attached
p_lot_width_x= 0.8 # Taper parking lot width
p_lot_width_y= dsk_rad + 1*clamp_length # Width of the support of the taper parking lot (has
    to be larger than any critical dimensions of the devices, due to releasing)
hgap = 25  # horizontal gap between disk and parking lot
vgap = 15 # vertical gap between disk and parking lot
pitch_x=2*(hgap+p_lot_width_x/2+dsk_rad) # Repetition pitch in the horizontal direction
pitch_y=2*(vgap+p_lot_width_y/2+dsk_rad) # Repetition pitch in the vertical direction
#ASYMMETRY BETWEEN PADDLES
var1_delta = 0.025 # Asymmetry between paddles - variation step
var1_init = -0.25 # Asymmetry between paddles - start value
var1_final = 0.25 # Asymmetry between paddles - stop value
i0max=(var1_final-var1_init)/var1_delta + 1   # Number of asymmetry values
#GAP BETWEEN TWO PADDLES VARIATION - bgap
var2_delta = 0.2 # Gap step
var2_init = 0.2 # Gap initial value
var2_final =1 # Gap final value
j0max=(var2_final-var2_init)/var2_delta + 1  # Number of gap values
for i0 in range(0,int(i0max)): #VAR1 ALONG X-direction
    dsk_x0 = i0*pitch_x # disk center x value
    drum_delta = var1_init + ( i0 % (i0max) )*var1_delta # asymmetry value
    for j0 in range(0,int(j0max)):   #VAR2 ALONG Y-direction
```

```
    paddle = []
    ## DISK
    dsk_y0 = j0*pitch_y   # disk center y value
    bgap = var2_init + ( j0 % (j0max) )*var2_delta # gap between paddles
    dsk = gdspy.Round( (dsk_x0,dsk_y0), dsk_rad, **wgcor )  # Define disk
    paddle_cell2.add( dsk )
    ## PADDLE OSCILLATOR
    x0 = dsk_x0 # Paddle x position
    y0 = dsk_y0 # Paddle y position
    paddle = paddle_oscillator((dsk_x0,dsk_y0), dsk_rad, [0.2,bgap,2], [drum_length,
drum_width, drum_delta],[clamp_width,clamp_length], [4*drum_length,
paddle_p_lot_width]) # Define paddles
    paddle_cell2.add(paddle)
    for ii in range(0,n_copies): # If more than one paddle device is coupled to a single
optical cavity, this generates them
        paddle_cell2.add(gdspy.boolean(paddle,lambda *p: sum(p[:]), **wgcor).rotate(ii*
numpy.pi*2.0/n_angular,(dsk_x0,dsk_y0)))
    ## ---------------------------------------- ##
    ##  PARKING LOT                             ##
    ## ---------------------------------------- ##
    r1,r2, p_lot = p_lot_2((dsk_x0,dsk_y0), [0,0], dsk_rad, [p_lot_width_x,p_lot_width_y],
[hgap,vgap])
    rect_in =gdspy.Rectangle(r1,r2, **wgcld)
    p_lot_array.append(p_lot.rotate(numpy.pi/2, (dsk_x0,dsk_y0)))
#Pack parking lots in the same polygon
paddle_cell2.add(gdspy.boolean(p_lot_array,lambda *p: sum(p[:]), **wgcor))
 #BOUNDING BOX
bbox = paddle_cell2.get_bounding_box()
BOX = gdspy.Rectangle((bbox[1,0]+1,bbox[1,1]+1),(bbox[0,0]-1,bbox[0,1]-1),**wgcld)
paddle_cell2.add(BOX)
BOX = gdspy.Rectangle((bbox[1,0]+1,bbox[1,1]+1),(bbox[0,0]-1,bbox[0,1]-1),**nofill)
paddle_cell2.add(BOX)

# ------------------------------------ ##
#  OUTPUT                              ##
# ----------------------------------- ##
gdspy.gds_print('OM_paddle.gds', unit=1.0e-6, precision=1.0e-9)
gdspy.LayoutViewer()
```